NTNU
Norwegian University of
Science and Technology

An In-situ FTIR Study of the Methanol to Hydrocarbons Reaction Over Zeolite Catalysts

Stian Forselv

Chemistry
Submission date: July 2011
Supervisor: Morten Bjørgen, IKJ
Co-supervisor: Karina Mathisen, IKJ

Norwegian University of Science and Technology
Department of Chemistry

Abstract

This thesis investigates several different types of zeolites during the conversion of methanol to hydrocarbons, and examines the effects of the differences between them. Two of the zeolite samples and a silicalite sample are further investigated in a more detailed series of experiments. All the zeolites are commercial “off the shelf” samples, while the silicalite sample was synthesized at NTNU by Johan Yttervik.

All samples were characterized by SEM, XRD, ICP-MS and BET to confirm that they were as reported by the manufacturers. The samples were investigated by in-situ FTIR during water desorption and during reaction while feeding methanol at 350 °C. The effluents of the reactions were analyzed by on-line GC-MS-FID. The further experiments were performed while feeding methanol at four different temperatures.

The zeolites show several differences during the reaction, mostly based on their topology. The sample H-Beta 12.5 2 gave some contradictory results, and a possible explanation for this is discussed. The further study describes in greater detail the interaction between methanol and the selected samples.

Sammendrag

Denne oppgaven studerer omdanningen av metanol til hydrokarboner over forskjellige typer zeolitter, og ser på følgene av ulikhetene mellom de. I tillegg er to zeolitter og en silikalitt prøve videre undersøkt i mer detaljerte forsøk. Alle zeolittene brukt er kommersielle prøver, silikalitt prøven er syntetisert på NTNU av Johan Yttervik.

Prøvene ble karakterisert ved SEM, XRD, ICP-MS og BET analyse for å bestemme fundamentale parametre. Prøvene ble også undersøkt med in-situ FTIR under desorbsjon av vann og under omdanning av metanol til hydrokarboner ved 350 °C. Effluentene fra reaksjonen ble analysert med direktekoblet GC-MS-FID. De videre forsøkene ble gjennomført under fire forskjellige temperaturer.

Zeolittene viste flere ulikheter under vanndesorbsjon og reaksjon, prøver av samme topologi viste mindre forskjeller. Prøven H-Beta 12.5 2 gav noen motstridende resultater, og en mulig årsak for dette er drøftet. Den videre undersøkelsen beskriver i større detalj vekselvirkningen mellom metanol og de utvalgte prøvene.

Acknowledgments

First of all I would like to than my supervisor Prof. Morten Bjørgen and my co-supervisor Ass. Prof. Karina Mathisen for their guidance and support. I especially thank Morten for giving me responsibilities in his lab, from which I have learned a lot.

I would also thank Saepurahman for performing the transmission FTIR investigations with me, Johan Yttervik for synthesizing the silicalite sample, Katrine Lie Bøyesen for helping me with the XRD instrument, Tina Kristiansen for aiding me with the BET measurements and Syverin Lierhagen for performing the ICP-MS analysis. I would further like to thank Julian Tolchard for help with the SEM instument and Gunnar Svare, Roger Aarvik and Stein Almo for helping me with laboratory equipment.

Finally, I would like to thank Liv Mari B. Høydal for proofreading and all my other friends for making these five years in Trondheim such a great time.

Contents

Chapter 1

Introduction

1.1 Catalysis

Catalysis is a major field of research and is crucial in modern chemical industry. Catalytic processes constitute approximately 10-15% of the gross national product of industrialized countries, and compose 85-90% of all products made in chemical processes [1]. The definition of a catalyst is a material that increases the rate of a reaction without being consumed, as in the reaction $A + B + C \rightarrow AB + C$. A catalyst works by offering a reaction an alternative route to occur by. This route usually involves more steps, but has a lower energy barrier which makes it more favorable energetically. In a reaction where several parallel reaction routes compete, a catalyst may improve the rate of one of these rutes, thus directing the selectivity of a process [2].

A potential energy diagram for a heterogeneous catalytic reaction is shown in figure 1.1. The uncatalyzed reaction follows a direct route where the reactants A and B combine to form the product AB. This route has a high energy barrier. The catalyzed reaction follows a route with several steps. The first step is the adsorption of reactants onto the catalyst, this step has a very low energy barrier and the adsorbed reactants are at a lower energy state than the free reactants.

The second step is the reaction between the two adsorbed reactants forming the product adsorbed on the catalyst. The energy barrier for this step is much lower than the reaction between the free molecules. The last step is desorption of the product which has a low activation energy. The energy barrier for the uncatalyzed reaction is much higher than for the catalyzed one, and fewer molecular collisions will have sufficient energy to reach the transition state. Both the catalyzed and the uncatalyzed reaction start and end at the same energy level as both start with free reactants and end with free product. The catalyst does not shift the equilibrium but it can make a system achieve equilibrium faster.

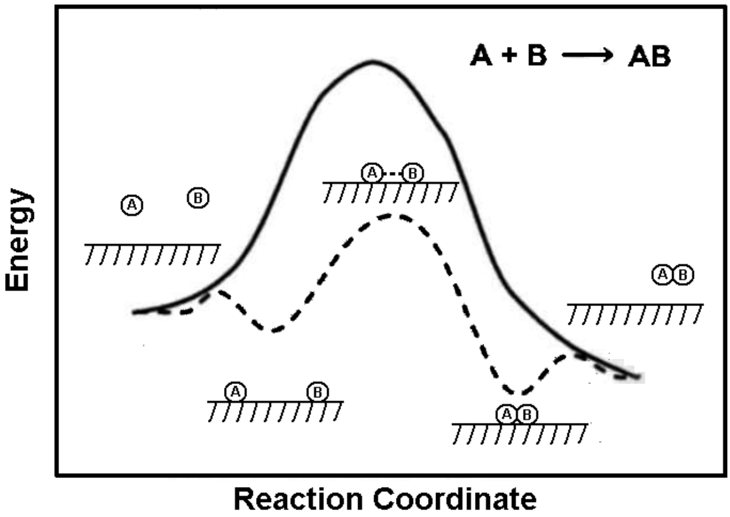

Figure 1.1: Energy level diagram for a heterogeneous catalyzed reaction. Adapted from [1].

Catalysis are divided into three categories: Heterogeneous catalysis, homogeneous catalysis and enzymatic catalysis/bio-catalysis. Only heterogeneous catalysis will be discussed here.

Heterogeneous catalysis is the most applied catalysis in the chemical industry [2]. As the name implies, a heterogeneous catalyst is of a different phase than the reactants and products. Usually the catalyst is a solid and the reactants and products are in gas phase. As can be seen in figure 1.1 a reaction between two gases over a solid catalyst involves both reactants and products to be adsorbed on the surface. An optimal catalyst should easily adsorb the reactants and keep them on the surface long enough to react. On the other hand, it should not bind too strong so that the reaction is hampered. It should also easily desorb the products to allow new reactants to adsorb.

For porous particles there can be other factors involved such as diffusion into pore channels and density of active sites. The micro-scale shape of a catalyst is important, the reactions only take place on the surface and it is therefore desired to achieve a high surface to weight ratio. The size of the pores is also of importance as for zeolites.

The conversion of a catalyst for a given reaction largely depends on the conditions the reaction is carried out at. Important parameters are temperature, pressure, concentrations and how long the catalyst has contact with the reactants. Since varying the amount of feed, catalyst or contact time will affect the conversion it is important to specify these values when comparing conversions. For plug flowreactors this is described by the weight hourly space velocity (WHSV), which is given as mass of reactants per mass of catalyst per hour.

1.2 Zeolites

A zeolite is a crystalline microporous aluminosilicate mineral which can occur natural or be synthesized in a lab [3, 4]. Zeolites were first described by the Swedish chemists/geologist Cronstedt who discovered stilbite in 1756. When heated, the stone released water in a frothing manner. This gave it the name “boiling stone”, in greek Zeolite. Zeolites possess several properties which makes them interesting materials as catalysts. The channels and cavities in the structure have well defined sizes on nanoscale [5]. This makes them shape selective, blocking large molecules while smaller pass through.

There are three types of shape selectivity: Reactant selectivity, when large molecules are prevented to enter the pores and react, while smaller and less branched molecules are not. Product selectivity, when large molecules formed inside pores or cavities are prevented to diffuse due to steric hindrance. Transition state selectivity, when only certain configurations of a transition state or reaction intermediate are possible due to the limited intracrystalline volume, effectively preventing certain reactions to occur.

All the pores and channels give the zeolite particles a very high internal surface. Another characteristic is the presence of acidic sites. This feature combined with the large internal surface and shape selectivity makes zeolites good acidic catalysts for the methanol to hydrocarbon (MTH) reaction.

Zeolites were initially only used as decorative crystals. During the late 1940’s their properties as molecular sieves were used commercially to separate oxygen and nitrogen. And in the 1960 it was used as a catalyst to crack crude oil to petrol. Their ability to catalyze methanol into hydrocarbons were discovered in 1976 by Mobile. A full scale MTG (methanol to gasoline) plant which converted natural gas to methanol and methanol to gasoline over a zeolite was built on New Zealand in 1986 [6].

There was optimism in scientific circles on behalf of the potential of zeolites as catalysts in the early 90’s [5], but as the crude oil prices dropped the MTG process became to expensive. In 1996 the MTG part of the plant in New Zealand was shut down, but the scientific work has still continued though. Zeolites has other applications as well, it is used to a large extent as an ion-exchanger in detergents and fabric softeners. Zeolites can also be used to strengthen cement, or to remove radioactive isotopes and NOx.

1.3 MTH

The conversion of methanol to hydrocarbons over a zeolite catalysts was first reported by Chang and Silvestri in 1976 [7]. Since then, much research on the reaction have been performed, and several industrial processes have been developed [8, 9, 10]. Methanol sources can practically be any carbon material, the most common being coal, natural gas or biomass. Zeolites ability to catalyze MTH reactions is not used commercially to any extent, but several pilot plants are operational. The main drawback of the MTH reaction is that it is more expensive than the conversion of crude oil into other hydrocarbons. The low cost and high accessibility of crude oil has ousted all other sources of fuel. Historically, only large nations subjected to global oil embargo's, like First World War Germany and apartheid South Africa, have relied on other processes to produce fuel.

However, as the global demand for oil steadily increases and oil prices are expected to rise, new fuel sources become economically feasible. Other examples of new crude oil sources of include oil sand in Canada and small or abandoned oil fields, previously considered too expensive to operate. The MTG reaction is therefore still of interest, and with sufficiently high oil prices it may be used to produce fuel in the future. MTH catalyzed by zeolites remain a major field of research and is the main focus of this thesis.

Chapter 2

Theory

2.1 MTH

After the discovery of the MTH reaction, the first experiments focused on the formation of C-C bonds between the oxygenates methanol and dimethyl ether, which only contain C-H, C-O and O-H bonds [11]. While a direct route from methanol and dimethyl ether has been indicated, it is assumed that this reaction occurs at negligible rates. In the early 1990s Dahl and Kolbe introduced an indirect route known as the hydrocarbon pool mechanism [12, 13].

This mechanism does not focus on the initial C-C formation but starts with higher hydrocarbons already present, possibly from remaining template or impurities in the methanol feed. These hydrocarbons are methylated by methanol and subsequently undergo rearrangement and alkane elimination. This route has gained general acceptance during the last decade.

The hydrocarbons constituting the hydrocarbon pool has been identified as polymethylbenzenes for several zeolites and zeotyopes. The first discovery was made by Arstad who identified arenes as the most important hydrocarbon pool specie for the zeotype SAPO-34 [14, 15]. The primary hydrocarbon pool species for H-Beta has been identified as hexamethylbenzene (HMB), its protonated counterpart and heptamethylbenzenium cation [16, 17, 18].

For H-ZSM-5 a dual cycle has been suggested [19, 6]. The first cycle consists of toluene and trimethylbenzene (TMB) which yields ethene and aromatics, while the second cycle consists of alkenes, e.g. propene, which is methylated into higher alkenes and cracks into smaller alkenes.

2.2 Zeolites

2.2.1 Structure

The basic building blocks of a zeolite are the types of corner sharing tetrahedra $[SiO_4]^{4-}$ and $[AlO_4]^{5-}$. These tetrahedra are combined into rings or other sub-units which are further combined to a repeating framework. When determining the ring size it is common to count either the number of tetraheradrally coordinated cation, known as T-atoms, or the oxygen atoms that forms the ring. The ring size ranges from four- to twenty-membered rings.

Rings with 8-members or more are large enough to be considered as pore openings. The diameters of 8, 10 and 12 membered rings are approximately 4.1, 5.5 and 7.4 Å, respectively. As a comparison, the kinetic diameters of He, CH_4 and benzene are 2.6, 3.8 and 5.85 Å respectively. When the subunits combine to form the framework structure, channels and in some cases cavities are formed.

2.2.2 Acidity

As Aluminum, Al, has only three valence electrons, a combination of a Silisium, Si, and Al, tetrahedra will result in a negative charge. This negative charge is balanced by a counter ion, after synthesis it will be a sodium atom. Through ion exchange with ammonium, this sodium atom can be exchanged with a hydrogen atom by the following equation:

$$\mathrm{NaZ}_{(s)} + \mathrm{NH}^+_{4(aq)} \rightleftharpoons \mathrm{NH_4Z}_{(s)} + \mathrm{Na}^+_{(aq)}$$

$$\mathrm{NH_4Z}_{(s)} \xrightarrow{\text{calcine}} \mathrm{NH}_{3(g)} + \mathrm{HZ}_{(s)}$$

Where Z is the zeolite. A hydrogen atom will have Brønsted acidic properties which can be used in acid catalysis. A schematic view of a Brønsted site is shown in figure 2.1. Because of the crystallographic orientation, the hydrogen is exposed to the inner surface and is accessible to any molecule inside the pores or cavities.

The negative charge can also result in Lewis acidity. If a zeolite is heated up to 550 °C, the Brønsted site and a framework oxygen atom is lost as water, creating a Lewis site as shown in figure 2.1.

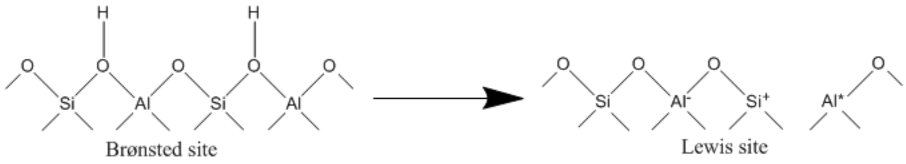

Figure 2.1: Formation of a Lewis site from a Brønsted site.

When examining the acidity of zeolites there are two values that can be measured, acid amount (or acid site density) and acid strength of each site. Acid amount correlates to the amount of base that has to be added to neutralize the zeolite. One method used to determine acid amount is temperature desorption (TPD) of ammonia, where the amount of chemisorbed ammonia determines the acid amount and strength [20]. The acid amount is given in mmol g^{-1}.

The other value is the acidic strength of each individual site. This value can be determined by e.g. investigating the sample interacting with probe molecules of different bacicity using infra red-spectroscopy [21, 22].

Each Brønsted site requires an Al atom in T sites, and the site density is therefore limited by the Si/Al ratio. Lowenstein's rule dictates that aluminum can not occupy sites in adjacent T sites, so the lowest possible Si/Al ratio is 1. The ratio is also dictated by synthesis methods [23], and it is common to perform post synthesis treatment e.g. steaming to increase the Si/Al ratio.

A very low Si/Al ratio does not necessarily result in a high acid site density as the extra Al atoms might be present on extra or inter framework sites.

The acid strength of a Brønsted site is affected by both the Si/Al ratio, the type of T-atom and the topology of the material. The acid strength is reduced if an Al atom has one or more Al atoms as next nearest neighbor (NNN). Each Al atom has nine NNN sites, so Si/Al ratios of less than 9-12 results in a overall lower acidity, as there will be more but weaker acidic sites.

In the 1980's, zeolites where believed to posses superacidic properties. It was however proven later that this is not the case [24]. The acidic strength of H-ZSM-5, H-Beta and H-MOR is approximately the same, while the strength of H-Y is somewhat lower [21, 22].

2.2.3 Topologies

The Atlas of Zeolite Framework Types contains more than 170 types of zeolite frameworks [25]. In this section, four selected frameworks will be described.

2.2.3.1 MFI

The most known zeolite with MFI structure is the ZSM-5. ZSM-5 stands for Zeolite Socony Mobile and was the zeolite used when the MTH reaction was first reported [7]. It is built up from only $[5^4]$ units but can also be described by $[5^8]$ units or pentasil chains.

2.2.3.2 H-ZSM-5 as a catalyst

The topology yields two channels, both 10-ringed. The first channel is sinusoidal and the other is straight and perpendicular to the first, as seen in figure 2.2. The

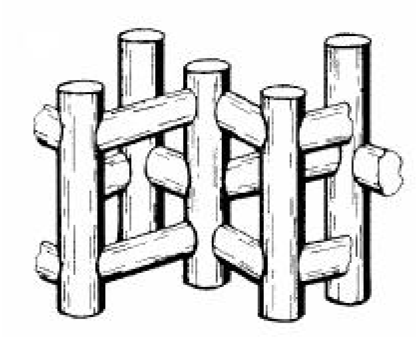

Figure 2.2: The straight and sinusoidal channels of ZSM-5 (MFI)[4].

channels has diameters 5.1 × 5.5 Å and 5.3 × 5.6 Å. Where the two channels cross, 3D intersections are created.

ZSM-5 is one of the most utilized industrial zeolites and is a well studied material. The ZSM-5 was early recognized as a potent catalyst, and is used in both methanol-to-olefin (MTO) and methanol-to-gasoline (MTG) processes [11]. One of the important features with ZSM-5 in the MTH reaction is that it uses a long time to deactivate, it is believed that deactivation is a result of coke formed on the external surface [26].

2.2.3.3 *BEA

The BEA framework is not ordered as other frameworks, and it is therefore marked with an asterisk. The idealized structure consists of $[5^4]$ units and 4-rings connected to form layers with saddle shaped 12-rings, as seen in figure 2.3. It is the stacking of these layers that gives rise to the disorder, as there are two different ways of placing the next layer. A zeolite with the *BEA topology is the Beta. There are three possible ordered polytypes of Beta, designated A,B and C [27].

2.2.3.4 Beta as a catalyst

The beta zeolite has three 12-ring channel systems, all present in the three polytypes of Beta. Two are linear and perpendicular to each other with a pore opening of approximately 5.7 × 7.5 Å. The channels do not change if the layer stacking sequence is altered. The third channel is perpendicular to the two first, and is created by their intersections. This creates a tortuous channel with pore openings of approximately 5.6 × 6.5 Å. Changing the layer stacking sequence can change the shape of this channel.

The Beta is not used in industrial MTH process applications, but has served as a model system for many mechanistic investigations [16, 28, 17, 29]. The pore

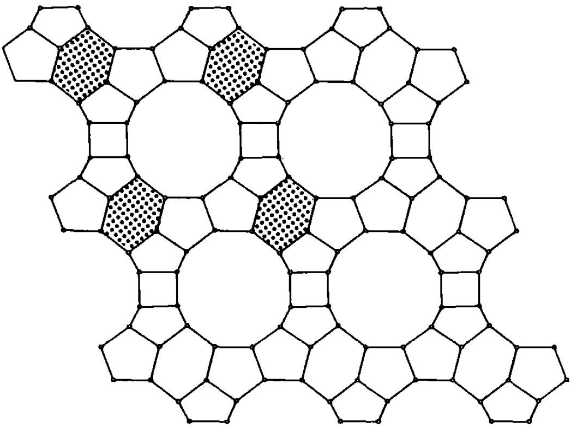

Figure 2.3: The pore opening of Beta polytype B [27].

openings of Beta are large enough to introduce hexamethylbenzene directly, unlike for ZSM-5. This makes the system ideal for investigating the polymethylbenzenes role in the MTH reaction.

2.2.3.5 FAU

The FAU consists of sodalite units connected by double 6-rings stacked in ABC layers as shown in figure 2.4. A zeolite with a FAU structure is the Y-zeolite. The Y and the X zeolite have identical structures and the only difference between them is the Si/Al ratio, a Si/Al $>$ 1.5 is a Y zeolite while a Si/Al $<$ 1.5 is a X zeolite [31].

2.2.3.6 H-Y as a catalyst

A Y zeolite is characterized by two types of cavities, so called supercages and sodalite cages. These supercages are very large, the largest of all known zeolites, with a free diameter of 12 Å. These cages are interconnected through 12-membered rings of 8-9 Å diameter. Sodalite cages have a free diameter of 9 Å and are connected to supercages by 6-membered rings of approximately 2.5 Å in diameter and to other solidate cages by double 6-membered rings. The structure contains equal amounts of each cage [32, 30].

In H-Y there are two types of Brønsted acidic sites, one pointing into the super cages and one pointing into the smaller solidate cage, the first being stronger than the former [33, 34]. Due to the difference of the apertures of the two cages, the accessibility is also different.

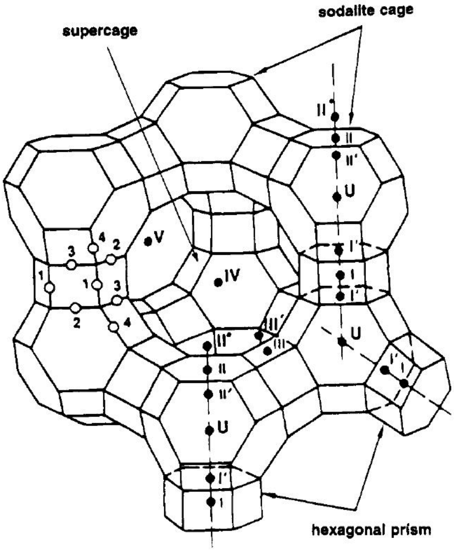

Figure 2.4: The supercage and sodalite cages of H-Y (FAU) [30].

An unmodified Y zeolite is not stable enough for industrial applications in the petroleum industry. To improve stability and the strength of acidic sites, the zeolite is dealuminated to form ultra-stable Y (USY) [35]. USY is among with ZSM-5 the most applied catalyst for the fluidized catalytic cracking (FCC) processes and is also used in hydrocracking [33].

2.2.3.7 MOR

The MOR topology is built up of edge sharing $\left[5^4\right]$ units which forms chains. The chains are combined to form sheets which are stacked with alternating mirror images as seen in image 2.5.

2.2.3.8 Mordenite as a catalyst

The two channel systems in mordenite consist of 12 and 8 membered rings which are perpendicular to each other. The 12-membered rings have pore openings of approximately 6.7×6.59 Å in diameter while the 8-membered rings has dimensions of 2.9×5.7 Å. The size of the former is so small that they are not considered as pores, hence mordenite is regarded as a 1-dimensional zeolite [36]. The two channels does not create any intersections or cavities.

M. Sawa et al. investigated the acid amount in several dealuminated H-MOR samples and concluded that there is a linear relationship between the acid amount

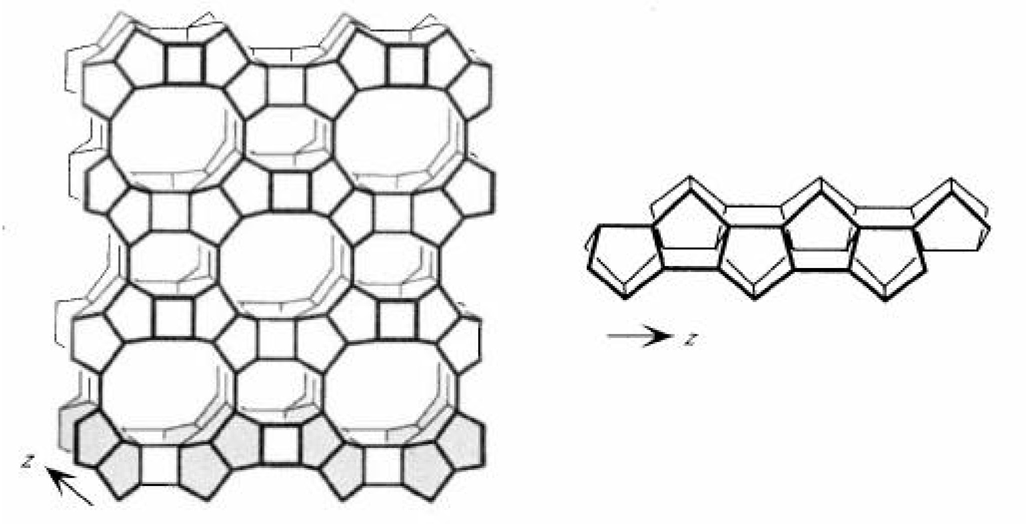

Figure 2.5: Stacking of sheets forming MOR topology [5].

and framework aluminum content for Si/Al above 7.5 [37]. For higher aluminum contents, the acid amount is lower because of the presence of aluminum with NNN aluminum.

Mordenite deactivates too fast for it to compete with ZSM-5 in the MTH reaction. As H-MOR is not damaged by dealumination, this treatment have been investigated to improve it's performance [36, 37]. Introduction of alkali earth metals has also been proposed [38]. Although improved catalytic performance has generally been reported, mordenite is not used in any industrial applications.

2.2.3.9 Summary, pore dimension

The pore dimensions and diameter of any cavities are shown in table 2.1.

Table 2.1: The pore and cavity dimension of selected zeolites.

Zeolite	pore (Å)	pore (Å)	diameter of cavities (Å)
H-ZSM-5	5.1 × 5.5	5.3 × 5.6	-
H-Beta	5.7 × 7.5	5.6 × 6.5	-
H-Y	8-9	2,5	12 and 9
H-MOR	6.7 × 6.59	2.9 × 5.7	-

2.2.4 Defects

In addition to crystallographic defects, zeolites may contain several surface defects. The bulk zeolite contains alternating T and oxygen atoms, but at the surface of the crystal there will be silicon atoms that do not share all its oxygen atoms with other silicon or aluminum atoms. These terminal oxygen atoms are balanced by hydrogen to form what is called silanols, shown in figure 2.6. Silanols do not have acidic nature like Brønsted sites since there is no negative charge to balance. As this happens on the external surface, the O-H groups are for the most part pointing out into void and do not interact with the rest of the structure.

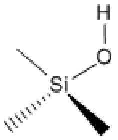

Figure 2.6: Silanol formed on the external surface of the crystal, adapted from [39].

Silanols can also be formed inside a crystal as a result of a defect. If a T atom is removed from the structure, the unbound oxygen atoms will form silanols. As these silanols are formed in the vacancy of the removed T atom, they are very close and will interact and form silanol-nests. Silanol nests can be partially cured by heating the sample above 700 K, which creates strained Si-O-Si bridges as shown in figure 2.7 [40]. Another type of defect is extra framework Al (EFAL). EFAL is created during dealumination, the removed Al-atoms migrate to the surface and may form Lewis acid sites [41].

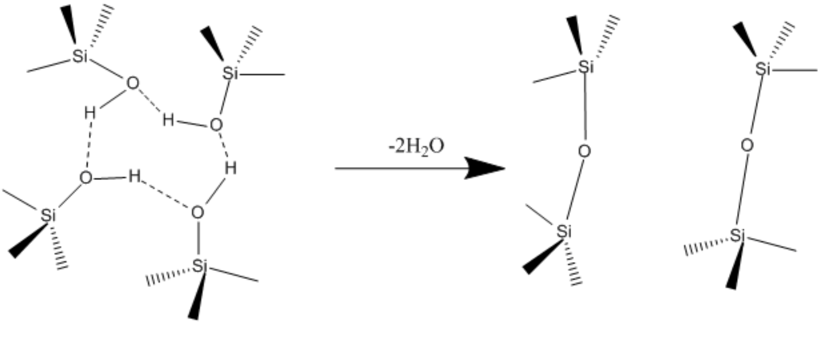

Figure 2.7: Curing of silanol nests.

2.3 Infrared spectroscopy

2.3.1 Light

Light is electromagnetic radiation found between 10 nm and 1 mm in the electromagnetic spectra, given in figure 2.8. The infrared region is divided into three groups, where mid IR (MIR) is the region most used for spectroscopy. Light can be seen as both a particle and a wave. It has a frequency and can cause interference like a wave, but at the same time it has quantized energy like a particle.

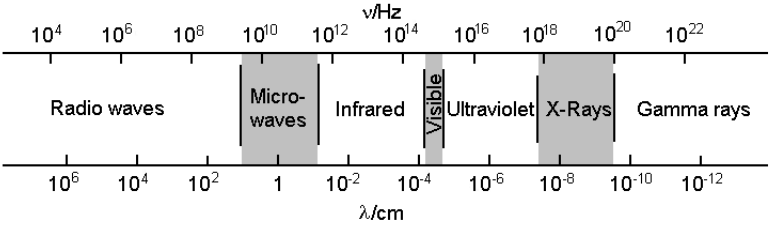

Figure 2.8: Electromagnetic spectra. Adapted from [42].

A light particle, or photon, has energy E_p which is given by

$$E_p = h\nu \tag{2.1}$$

where h is Planck's constant and ν is the frequency. In spectroscopy it is common to use wavenumbers instead of frequency or wavelength. The unit wavenumber is defined as

$$\tilde{v} = \frac{1}{\lambda} \tag{2.2}$$

where λ is the wavelength of the radiation and $\widetilde{v}$ is the wavenumber, usually expressed in terms of reciprocal centimeters (cm^{-1}).

2.3.2 Molecular Vibrations

2.3.2.1 Degree of Freedom

A molecule of N atoms has 3N degrees of freedom. Three of these are translations along the principal axes, while two or three more are rotational motions for linear and non-linear molecules, respectively. The remaining 3N-6 modes (3N-5 for linear) are vibrational degrees of freedom. The vibrational modes for a triatomic non-linear molecule are shown in figure *2.9*. There are four different types of vibrational modes, these are stretching (ν), bending in and out of plane (δ and γ resp.) and torsion (τ), the general magnitude of the frequencies are $\nu > \delta > \gamma > \tau$.

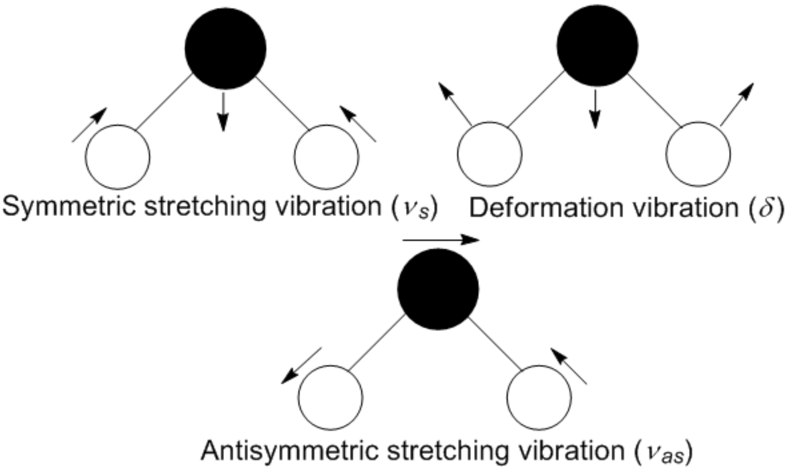

Figure 2.9: Vibrational modes for a triatomic non-linear molecule. Adapted from [43].

2.3.2.2 Classical Vibration Frequency

The classical vibration frequency can be derived using Hooke's law and Newton's second law. This frequency is identical to the quantum mechanical frequency and can be used as a good approximation in calculations.

Consider a diatomic molecule illustrated by two spheres with masses m_1 and m_2 connected by a massless spring. The spheres can vibrate by stretching or compressing the bond, and the displacement of the masses are given as X_1 and X_2. The spring is assumed to obey Hooke's law

$$Force = -Fx \tag{2.3}$$

where F is a constant and x is the displacement of the spring form the equilibrium position ($X_2 - X_1$ in the case of our molecule). By combining Hooke's and Newton's laws, the following two equations are obtained:

$$F\left(X_2 - X_1\right) = m_1 \frac{d^2 X_1}{dt^2} \quad and \quad -F\left(X_2 - X_1\right) = m_2 \frac{d^2 X_2}{dt^2} \tag{2.4}$$

Since the equations are functions of X and its second derivative a trial solution where X varies as a cosine function of time can be proposed:

$$X_1 = A_1 cos\left(2\pi\nu t + \alpha\right) \quad and \quad X_2 = A_2 cos\left(2\pi\nu t + \alpha\right) \tag{2.5}$$

Where A is the maximum amplitude, ν is the frequency of the vibration and α is a phase constant. By differentiating twice with respect to time t thw following qeuations are obtained

$$\frac{d^2X_1}{dt^2} = -A_1 4\pi^2\nu^2 cos\left(2\pi\nu + \alpha\right) \quad and \quad \frac{d^2X_2}{dt^2} = -A_2 4\pi^2\nu^2 cos\left(2\pi\nu + \alpha\right) \tag{2.6}$$

Inserting equation 2.4 and 2.5 into equation 2.6 gives

$$F\left(A_2 - A_1\right) = -m_1 A_1 4\pi^2\nu^2 \quad and \quad \left(A_2 - A_1\right) = -m_2 A_2 4\pi^2\nu^2 \tag{2.7}$$

By rearranging, the amplitude ratios are obtained

$$\frac{A_1}{A_2} = \frac{F}{F - m_1 4\pi^2\nu^2} \quad and \quad \frac{A_1}{A_2} = \frac{F - m_2 4\pi^2\nu^2}{F} \tag{2.8}$$

Solving the equations for v yield

$$16\pi^4 m_1 m_2 \nu^4 - 4\pi^2 F\left(m_1 + m_2\right)\nu^2 + F^2 = F^2 \quad and\, further \quad \nu^4 = \nu^2\left(\frac{F\left(m_1 + m_2\right)}{4\pi^2 m_1 m_2}\right) \tag{2.9}$$

For solutions other than $\nu = 0$, the classical vibration frequency is obtained

$$\nu = \frac{1}{2\pi}\sqrt{F\left(\frac{1}{m_1} + \frac{1}{m_2}\right)} \tag{2.10}$$

2.3.2.3 Vibration Potential

Returning to the case of the diatomic molecule, energy as a function of dislocation is

$$E = \frac{1}{2}FX_{max}^2 \tag{2.11}$$

where F is a force constant and X_{max} is the maximum dislocation, where the kinetic energy is zero. The plot of E as a function of displacement follows that of a parabola or a harmonic oscillator. The classical and quantum mechanical harmonic oscillator is shown in figure 2.10. X_{max} can take any value and the total energy is constant as X varies from X_{max} to $-X_{max}$. Since the kinetic energy and velocity of the atoms increases as $|X| \rightarrow 0$, the molecule will spend more time stretched or compressed than at equilibrium distance. As a result, the probability function will be largest at X_{max} and $-X_{max}$ as shown in figure 2.10.

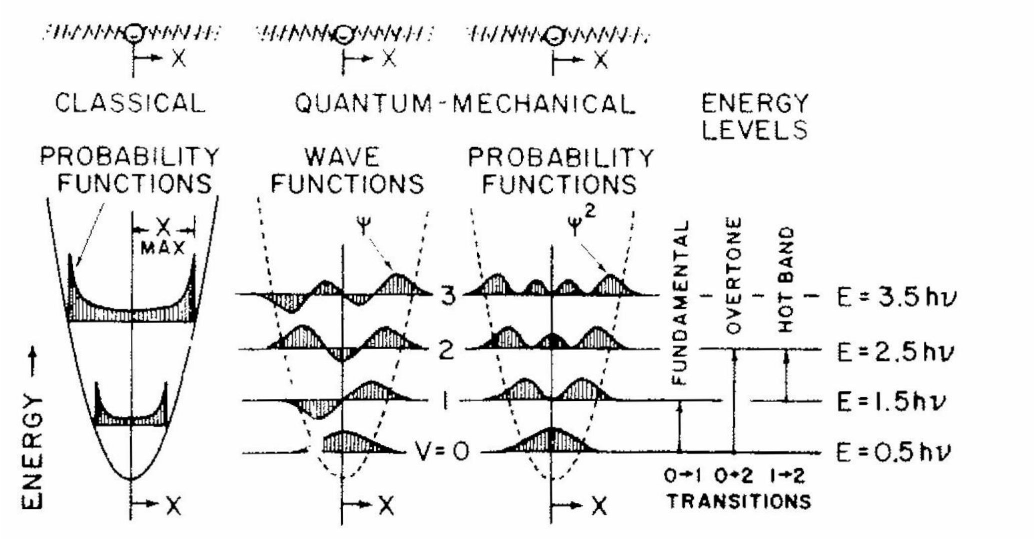

Figure 2.10: Classical and quantum mechanical harmonic oscillators with probability functions [44]. Different transitions are also shown. Note that the overtone transition is forbidden for a harmonic oscillator .

2.3.2.4 Quantum Mechanical Considerations

Since the dimensions of molecules are very small, the wave-particle duality of matter must be taken into consideration. The duality is shown with the deBroglie wavelength which is defined as

$$\lambda = \frac{h}{p} \tag{2.12}$$

where λ is the wavenumber of the particle, h is Planck's constant and p is the momentum of the particle. The quantum mechanical harmonic oscillator is given by

$$E_{vib} = \left(\upsilon + \frac{1}{2}\right) h\nu \tag{2.13}$$

where h is Planck's constant, ν is the classical vibrational frequency and υ is a quantum number which can take integer values or the value 0. This means that the energy for a molecular vibration is quantized and can only take specific discrete values. The energy difference between two states, i and j, is given by

$$\Delta E = \left(\upsilon_j + \frac{1}{2}\right) h\nu - \left(\upsilon_i + \frac{1}{2}\right) h\nu = h\nu \tag{2.14}$$

Due to Heisenberg's uncertainty principle, and as can be seen from equation 2.14 and figure 2.10, the lowest value for E_{vib} is $\frac{1}{2}h\upsilon$ and not 0 as for the classical case. The uncertainty principle also allows the wave function to exceed X_{max}. The harmonic oscillator only allows transitions between neighboring states, i.e. $\Delta v = \pm 1$.

2.3.2.5 Absorption

We have now seen that the molecular vibrations can only occupy certain energy levels and that there is a given separation between these states. For a transition from one state to another, the molecule must absorb or loose energy equal to the energy difference between the two states, $h\nu_m \Delta v$. As a result it can absorb a photon only if the photon has exactly this energy. The energy of a photon from equation 2.1 is $E_p = h\nu_p$, where ν_p is the frequency of the photon. By combining equation 2.1 and 2.14 the equation

$$\nu_p = \nu_m \Delta v \tag{2.15}$$

is obtained. For a transition between neighboring states the photon must have the same frequency as the molecular vibration.

2.3.2.6 Dipole Moment

It has been shown that the absorption frequency is related to the vibrational frequency, but the absorption intensity have not been considered. It can be shown that the intensity of an infrared absorption is proportional to $\left(\frac{\delta\mu}{\delta Q}\right)^2$ where μ is the dipole moment and Q is the normal coordinate. This results in the gross selection rule which requires that the vibration causes a change in the dipole moment of the molecule.

Another consequence is that a vibration which causes a large change in dipole moment will absorb more intensely than a vibration which causes a small change in dipole moment. An example is the dipole monents of silanols and Brønsted acidic sites. The later has a higher dipole moment and will appear overrepresented in a IR spectrum, even though the concentration of silanols most likely is higher.

2.3.2.7 Anharmonicity

The equation derived for the classical vibration frequency assumed that the displacement varied with time as a cosine function. This is true for a mechanical harmonic vibration but not for a vibration with mechanical anharmonicity. An anharmonic vibration will still be periodic, but it will not follow a simple sine or cosine plot. Any anharmonic vibration can however be described by several sine or cosine terms where the frequencies are integral multiples of the fundamental vibrational frequency.

These additional frequencies are called overtones. The selection rule for an anharmonic oscillator is not as strict as for the harmonic and allows transitions between non-neighboring states, $\Delta \upsilon = \pm 1, 2, 3, ...$ For one of these transitions to occur more energy is required, e.g. for the transition $0 \rightarrow 2$ the photon must have a frequency twice that of the molecular vibration.

2.3.2.8 Anharmonic Oscillator

To better describe the anharmonic features of molecular vibrations an anharmonic oscillator must be applied. The Morse oscillator, shown in figure 2.11, is an anharmonic oscillator and is given by the equation

$$E_{vib} = h\nu_e \left(\upsilon + \frac{1}{2} \right) - x_e h\nu_e \left(\upsilon + \frac{1}{2} \right)^2 \tag{2.16}$$

where x_e is an anharmonicity constant. With the introduction of a new second order term, the spacing between neighboring states will no longer be constant for all states but will instead decrease for higher states. A transition $\upsilon = 2 \leftarrow \upsilon = 1$ will therefore require less energy than $\upsilon = 1 \leftarrow \upsilon = 0$ and so on. Transitions from an excited state to a higher state is often called hot bands.

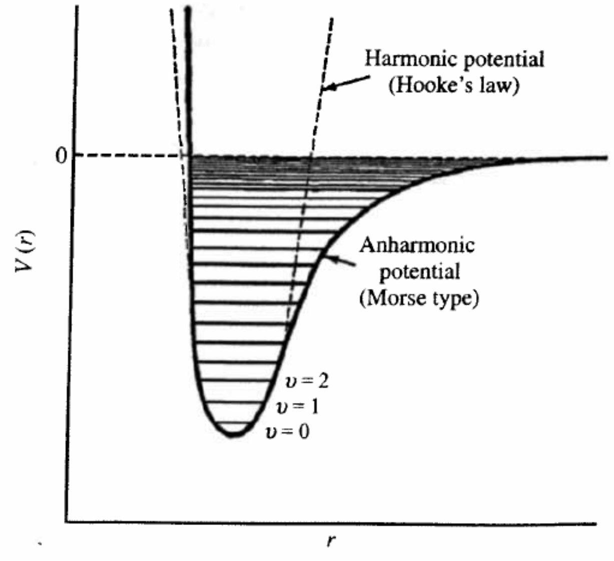

Figure 2.11: Morse oscillator [45].

2.3.2.9 Boltzmann

For hot bands to occur, states with higher quantum numbers must be occupied. This can happen due to thermal excitations. The relative population of an ith energy level is given by the Boltzmann distribution function for non degenerate states

$$\frac{n_i}{n_0} = e^{-(E_i - E_0)/kT} \tag{2.17}$$

2.3.2.10 Effect of anharmonicity

The introduction of anharmonicity allows one photon to excite two different vibrational modes in the same molecule, this gives rise to combination bands in the IR-spectra. The excitation can only occur if the photon has exactly the same energy as the sum of the two transitions

$$E_p = h\nu_p = \Delta E_m = \left(\upsilon_{1,j} + \frac{1}{2}\right) h\nu_1 - \left(\upsilon_{1,i} + \frac{1}{2}\right) h\nu_1 + \left(\upsilon_{2,j} + \frac{1}{2}\right) h\nu_2 - \left(\upsilon_{2,i} + \frac{1}{2}\right) h\nu_2 \tag{2.18}$$

$$h\nu_p = h\nu_1 \Delta\upsilon_1 + h\nu_2 \Delta\upsilon_2 \tag{2.19}$$

Where υ_1 and υ_2 is the quantum number of vibration 1 and 2 respectively and ν_1 and ν_2 is the vibrational frequency of vibration 1 and 2.

Another feature that anharmonicity allows is difference bands. Difference bands appear as a result of absorption of a photon with a wavenumber that is exactly equal to the difference between two fundamental transitions.

$$E_p = h\nu_p = \Delta E_m = \left(\upsilon_{1,j} + \frac{1}{2}\right) h\nu_1 - \left(\upsilon_{1,i} + \frac{1}{2}\right) h\nu_1 - \left(\left(\upsilon_{2,j} + \frac{1}{2}\right) h\nu_2 - \left(\upsilon_{2,i} + \frac{1}{2}\right) h\nu_2\right) \tag{2.20}$$

$$h\nu_p = h\nu_1 \Delta\upsilon_1 - h\nu_2 \Delta\upsilon_2 \tag{2.21}$$

2.3.2.11 Fermi Resonance

Fermi resonance occurs when an overtone or combination transition and a fundamental transition of the same molecule have the same frequency. The result is that two bands will appear in the spectra, one at a slightly higher wavenumber and one at a slightly lower. This is due to quantum mechanical mixing. Fermi resonance can be observed when the Brønsted site of a zeolite is interacting with a base through medium to medium-strong H-bonds [46].

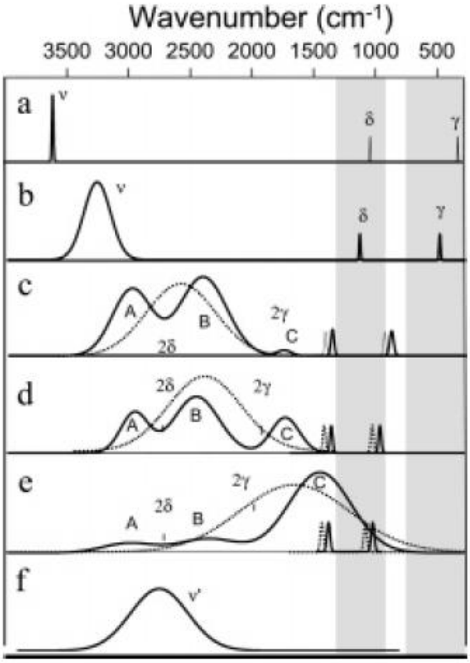

Figure 2.12: Fermi resonance between the stretching mode and two bending modes of a AH bond in a Brønsted acid interacting with bases of increasing strength [46].

The expected features of a Brønsted acid, AH, interacting with bases, B, of increasing strength is shown in figure 2.12. (a) shows an unperturbed AH oscillator, note that the bending modes are hidden by the bands from the framework (shaded area). (b) shows interactions through a weak H-bond. This bond perturbs the AH bond, causing the stretching mode to red shift and the bending modes to blue shift. The width of all three bands are increased.

(c) and (d) shows interaction through a medium and a medium strong H-bond. The full drawn lines show actual spectra, while the dotted line shows the expected features without Fermi resonance. It is expected that the bands are to shift further with increasing bond strength, but instead three bands appear. The fundamental of the stretch mode and the overtones of the bending modes have shifted enough to partially overlap, causing Fermi resonance.

In (c), the overtone of the in plane bending, 2δ, is overlapping well with the vibration fundamental. This creates two components, A and B like normal Fermi resonance. The other bending mode, 2γ, is too far away from the fundamental stretch to result in pronounced Fermi resonance. The C band therefore has a very low intensity. In (d), the modes are shifted so far that the fundamental stretch is placed between the two overtones and causes Fermi resonance with both. Now the B component is the most intense, while the A and C components have similar intensities.

Interaction through a strong H-bond is shown in (e). The modes are now shifted to the extent that the fundamental stretch is only causing Fermi resonance with the fundamental of the in plane bending mode δ. This gives a intense C band partially covered by the framework bands. The A and B components both have a low intensity. (f) shows the interaction between the deprotonated acid and the protonated base through a H-bond. The basicity of the base is now so high that a proton transfer occurs. There is now a new species bonded to the proton, and hence new vibrational modes.

2.3.3 The interferogram

An infrared spectrum shows absorbance or transmittance as a function of wave number. In the early days of IR-spectroscopy, a spectrum was obtained by determining the absorbance of each wave number individually, using one scan per wave number. This is very time consuming as a spectrum from 400-4000 cm^{-1} with a resolution of 1 cm^{-1} would require 3600 scans. Modern instruments scan over all wave numbers simultaneously using an interferometer and a Fourier transformation [45].

2.3.3.1 Michelson interferometer

The Michelson interferometer, shown in figure 2.13, consists of a beamsplitter and two mutually perpendicular mirrors. One of the mirrors is fixed while the other can move along an axis perpendicular to its plane. Light generated by an external source entering the interferometer is first divided by the beamsplitter and the two components are reflected by the mirrors and recombined at the beamsplitter. Depending on the position of the moving mirror, parts of the beam return to the source while the rest continues to the detector.

Let the center of the beamsplitter be at a point called O and the position of the fixed and movable mirror be F and M respectively. Assuming an infinitely narrow beam, the path from the beamsplitter to the mirrors and back is 2OF for the fixed mirror and 2OM for the movable. The optical path difference (OPD) is given by $2\,(\mathrm{OM}-\mathrm{OF})$ and is denoted δ. When the path difference is zero the movable mirror is said to be at zero path difference, ZPD.

When a beam is reflected by a mirror at normal incidence the phase changes with 180°, while it changes with 90° when reflected by an ideal beamsplitter. The beam transmitted by the beamsplitter does not undergo any phase change. Both beams that pass to the detector are reflected once by the beamsplitter and once by one of the mirrors and therefore undergoes the same phase change of 270°. Assuming

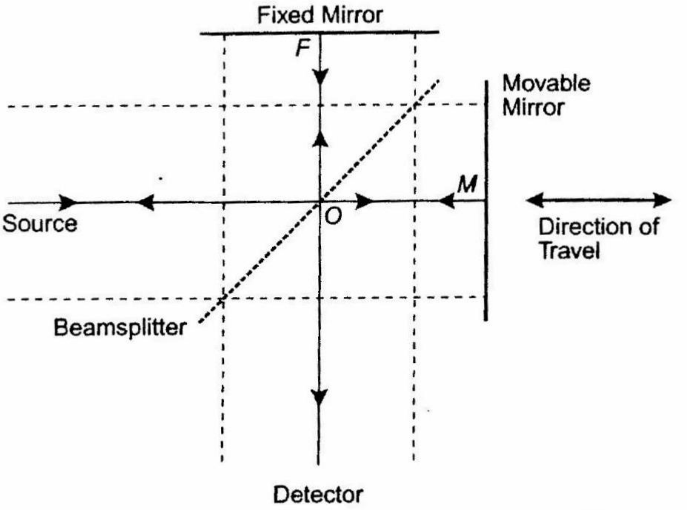

Figure 2.13: Michelson interferometer [45].

that the mirrors are at ZPD or that the OPD is $n\lambda$, the beams will be in phase and interfere constructively when they recombine.

For the beams that return to the source there is a difference depending on which mirror they reach. The beam that goes to the fixed mirror is reflected twice by the beamsplitter and once by the fixed mirror giving a total phase change of 360°, while the beam that is reflected by the moving mirror is transmitted twice by the beamsplitter and reflected once by the moving mirror for a total phase change of 180°. When these two beams recombine they will be 180° out of phase and interfere destructively.

If the OPD is increased to $\frac{1}{2}\lambda$, the beams passing to the detector will interfere destructively while the beams returning to the source interfere constructively. Using a monochromatic beam, the intensity of the beam at the detector is given by

$$I'(\delta) = 0.5I(\widetilde{v}_0)\left(1 + cos2\pi\frac{\delta}{\lambda}\right) \tag{2.22}$$

where $I(\widetilde{v}_0)$ is the intensity of the source. The interferogram with an ideal interferometer is given by the ac signal

$$I(\delta) = 0.5I(\widetilde{v}_0)\,cos2\pi\widetilde{v}_0\delta \tag{2.23}$$

Due to nonideality of several components, the ac signal from the amplifier is

$$S(\delta) = 0.5H(\widetilde{v}_0)\,G(\widetilde{v}_0)\,I(\widetilde{v}_0)\,cos2\pi\widetilde{v}_0\delta \tag{2.24}$$

where $H\left(\widetilde{v}_0\right)$ is a wavenumber correction factor and $G\left(\widetilde{v}_0\right)$ is the responsitivity of the detector and amplifier. All the wavenumber dependent functions can be combined to $B\left(\widetilde{v}_0\right)$ resulting in

$$S\left(\delta\right) = B\left(\widetilde{v}_0\right) cos 2\pi \widetilde{v}_0 \delta \tag{2.25}$$

where $B\left(\widetilde{v}\right)$ is the single beam spectral intensity, giving the intensity of the source modified by instrumental characteristics.

2.3.3.2 Fourier transformation

The interferogram with a continuum source is given by

$$S\left(\delta\right) = \int\limits_{-\infty}^{+\infty} B\left(\widetilde{v}\right) cos 2\pi \widetilde{v} \delta d\widetilde{v} \tag{2.26}$$

with a cosine Fourier transform pair

$$B\left(\widetilde{v}\right) = \int\limits_{-\infty}^{+\infty} S\left(\delta\right) cos 2\pi \widetilde{v} \delta d\delta \tag{2.27}$$

$S\left(\delta\right)$ is an even function, hence equation 2.27 can be rewritten with limits from 0 to $+\infty$

$$B\left(\widetilde{v}\right) = 2 \int\limits_{0}^{+\infty} S\left(\delta\right) cos 2\pi \widetilde{v} \delta d\delta \tag{2.28}$$

Equation 2.28 is important because it shows that in order to measure the complete spectrum at infinitely high resolution, δ has to vary from 0 to $+\infty$. Since $\frac{\delta}{2}$ is the distance the mirror is moving it is clear that the resolution is finite, limited by the length the mirror can move. The resolution is defined as the smallest difference in wavenumber that still yields two different peaks, $\Delta\widetilde{v} = \widetilde{v}_1 - \widetilde{v}_2$. The lowest resolution obtainable is given as

$$\Delta\widetilde{v} = \frac{1}{\Delta_{max}} \tag{2.29}$$

Where Δ_{max} is the maximum retardation of the interferometer. Figure 2.14 shows an actual Fourier transformation from an interferogram to a single beam spectrum.

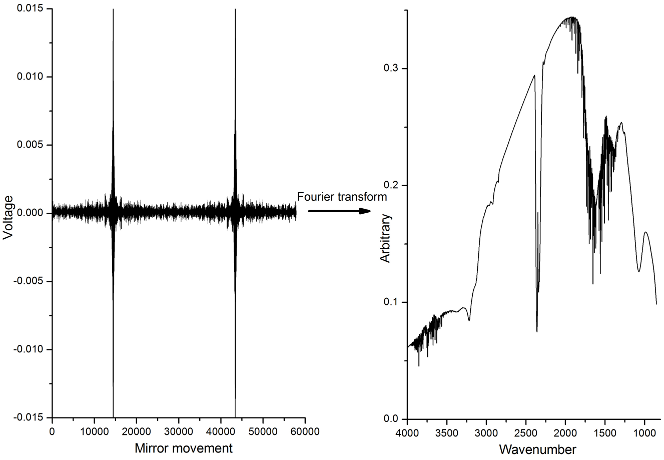

Figure 2.14: An interferogram and the Fourier transformed single beam spectra. Note the symmetry of the interferogram.

2.4 FTIR on Zeolites during MTH

A transmission FTIR spectrum of a calcined zeolite is shown in figure 2.15.

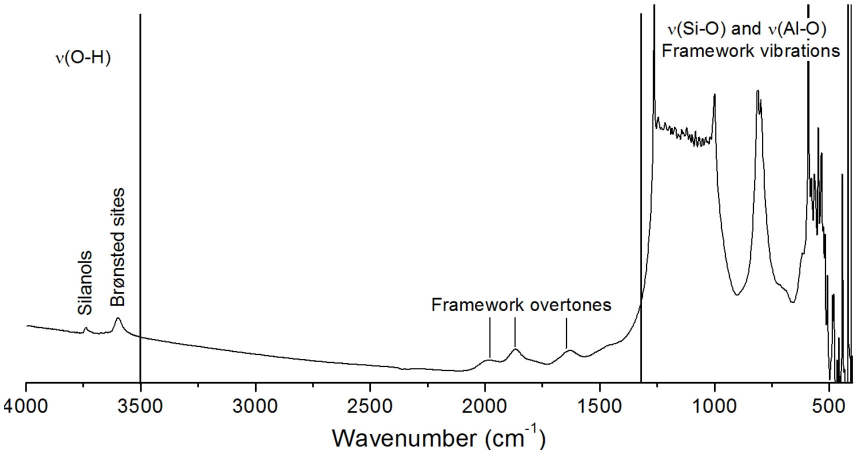

Figure 2.15: FTIR spectrum of a calcined zeolite.

The bonds in a zeolite structure can be divided into two main groups, Si-O and Al-O in the framework structure and O-H on the surface [39]. The vibrational modes from the framework gives a broad and very intense band, usually ranging from 400 to 1300 cm^{-1}, which is not used to gain information about the system. The framework also has combination bands and overtones giving three tops around 1640, 1870 and 1980 cm^{-1}.

The O-H bonds give rise to bands between 3550 to 3750 cm^{-1}. The band from the stretching mode of brønsted sites is found between 3650-3500 cm^{-1} while isolated silanols are found as a narrow band around 3735 cm^{-1}. The bending modes of the Brønsted sites falls in the region dominated by framework vibrations and can therefore not be distinguished. Bands from silanol nests have wavenumbers from 3650 to 3500 cm^{-1} and are usually broad.

v(O-H) from oxygen bound to extra lattice aluminum gives rise to bands located around 3665 cm^{-1} and v(O-H) from extra lattice aluminum is found around 3780 cm^{-1}. Bands from v(O-H) from extra lattice aluminium appear around 3660 cm^{-1} [47]. For samples with large particles, the scattering profile will increase at higher wavenumbers as the wavelength of the IR-beam approaches the size of the particles. This increase can be seen in figure 2.15.

When Brønsted sites interact with bases a hydrogen bonded adduct can be formed (Scheme 1), whilst if the base is strong enough the site can be deprotonated (Scheme 2) adapted from [39].

SCHEME 1 and 2

A hydrogen-bonded adduct will affect the vibrational frequencies of both the Brønsted site and the base. The stretching mode of the Brønsted site will be red shifted while the bending modes and internal modes of the base will be blue shifted, the Brønsted site is much more shifted than what the base is. If the site is deprotonated, the v(O-H) bond from the Brønsted site will naturally not be present at all but the protonated base will.

A transmission FTIR spectra of a zeolite with adsorbed hydrocarbons is shown in figure 2.16.

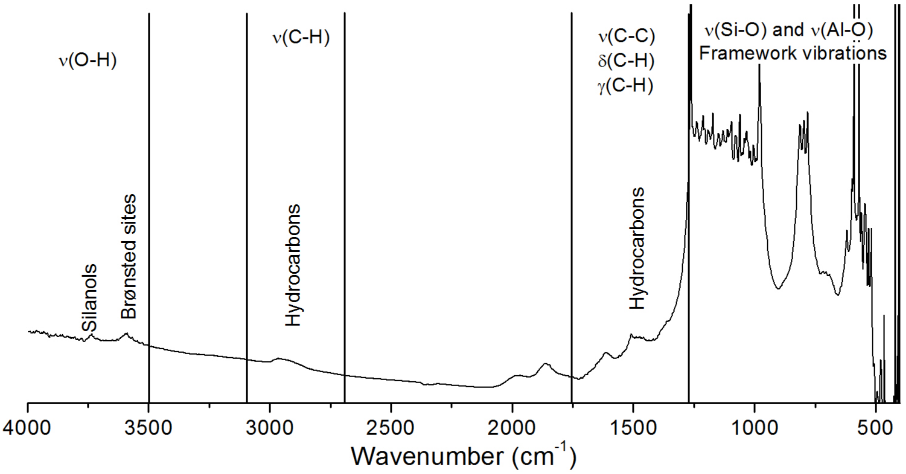

Figure 2.16: FTIR spectrum of hydrocarbons adsorbed on a zeolite.

When introducing hydrocarbons, bands from v(C-H) modes will appear between 2700 and 3100 cm^{-1}, while bands from δ(C-H), γ(C-H) and υ(C-C) modes will appear between 1300 and 1700 cm^{-1}. The bands between 1300 and 1700 cm^{-1} will be superimposed on bands from the zeolite, and the spectrum of the calcined sample should be subtracted to show new bands. It should also be noted that framework bands tends to shift to higher wavenumbers when hydrocarbons are adsorbed and may hide bands. As the zeolite adsorbs species, hydrocarbons or other, the particle size will increase and as a result the scattering profile will increase.

2.5 Physical characterization methods

2.5.1 X-Ray Diffraction

X-ray diffraction (XRD) is a videly used characterization method used for crystals. X-rays are generated by electrons colliding with metal at high velocity. When the electrons are slowed down by the repelling force from the electrons of the metal the kinetic energy is converted to a photon. This causes radiation with a broad wavelength distribution. The incoming electron can also eject electrons from the metal atoms. When an electron from a higher energy level fills this vacancy, radiation with wavelength characteristic for the spesific atom is emitted. It is this characteristic X-ray that is used for monochromatic sources.

A particular characteristic X-ray is isolated by applying a filter that absorbs all other characteristic X-rays. The most used radiation is K$_\alpha$ from copper. When X-rays interact with a crystal diffraction occurs. The incoming rays can be considered as reflecting off atomic planes in the crystal. The condition for diffraction to occur is given by Bragg's law

$$n\lambda = 2d\,sin\theta \tag{2.30}$$

where n is an integer, λ is the wavelength of the incoming X-ray, d is the distance between the atomic planes and θ is the angle between the incoming X-rays and the atomic plane. By varying θ a diffraction pattern is obtained. This pattern depends on the structural arrangement of the atoms and is unique for different types of crystals. XRD is therefore used to identify crystals and topologies [48, 49].

2.5.2 BET

Brunauer-Emmet-Teller (BET) is a simple and frequently applied method to determine surface area [50]. BET is performed by adsorbing gas onto the material to be investigated, using known pressures. The BET-equation is then used to determine the monolayer coverage. By multiplying monolayer coverage with Avogadro number and molecular projected area of the gas, the surface area is obtained.

2.5.3 ICP-MS

Inductively coupled plasma mass spectrometry (ICP-MS) is a technique used to detect trace elements. The samples are usually in liquid form but are converted to an aerosol in the instrument. The fine aerosols are separated in a spray chamber and sent to a plasma torch. In the plasma torch positive ions are formed. The ions then pass electrostatic lenses which guide them to a mass separator. The separated ions are then converted to an electric signal. The advantage of an ICP-MS is the low signal noise which enables it to detect very low element concentrations, in addition to quantitatively analyze higher concentrations [51].

2.5.4 SEM

Scanning electron microscopy (SEM) is a technique used to study materials on micrometer scale. It is a convenient method to determine shape and size of particles. The microscope works by emitting a beam of electrons from an electron gun followed by narrowing of this beam with electromagnetic condenser lenses. After focusing by an objective lens, the beam hits the sample and interacts with it.

To ensure that the beam only interacts with the sample, the beam path is kept in high vacuum. The electron beam can interact with the sample in several ways, giving off different signals. The two signals used for imaging originates from the backscattered electrons and the secondary electrons.

As the name implies, the electron beam in a SEM is scanned over the surface of the sample to create an image. When using SEM on a non conductive sample, the sample will not emit all electrons immediately but build up charge. This is problematic as charged particles will appear bright without texture. To prevent charging it is common to either coat the sample in gold or carbon or to use low vacuum [52, 49].

2.5.5 Gas chromatography

Chromatography is a technique used to separate different molecules based on their different mass and chemical properties. The mixture to be separated is carried through a column by a mobile phase, either a gas or a liquid, over a stationary phase. This stationary phase will interact with various components in the mixture. As the stationary phase interacts differently with different components, a difference in velocity is achieved. The compounds will therefore pass through the column at different times, called retention times. Once through the column, the components can be analyzed by e.g. a mass spectrometer, (MS) or a flame ionized detector (FID) [53].

2.5.6 Mass Spectrometry

In a mass spectrometer the molecules are bombarded by electrons, creating ions which fragments into smaller ions. These ions are then separated according to their mass-to-charge ratio by a mass analyzer and converted to an electric signal. The ions created are a fingerprint of the original molecule, and can be used for qualitatively identification. When calibrated the MS can also be used for quantitatively analyses [54].

2.5.7 FID

A FID is a simple quantitative detector with high sensitivity for organic compounds. The detector works by burning the analyte in a hydrogen-air flame. When organic molecules are introduced to the flame, radicals are formed. These radicals react to ions which are detected by a collector electrode. A FID detector does not detect amongst other water, carbondioxide or ammonia [53].

Chapter 3

Experimental

3.1 Physical characterization of materials

To confirm the information of the samples given by the suppliers, the samples were investigated using XRD, BET, ICP-MS and SEM. All techniques were performed at NTNU.

3.1.1 XRD

The topology of the materials was confirmed using powder X-ray diffraction, performed on a Bruker AXS D8 FOCUS diffractometer using Cu K_α radiation.

3.1.2 BET

The surface area using BET was obtained from a Tristar 3000 Micromeritics Surface Area and Porosimetry Analyzer at liquid nitrogen temperature. All samples were degassed at 250 °C for 24 hours prior to measurements. Specific surface area was calculated by BET model on the adsorption isotherm from 5 points of relative pressure.

3.1.3 ICP-MS

The Si/Al ratio was verified using ICP-MS. The samples were dissolved in HNO_3 (1,5 mL) and HF (0,5 mL), diluted to 216 mL with distilled water and analyzed on a High resolution ICP-MS, ELEMENT 2 from Thermo Electronic.

3.1.4 SEM

Prior to investigation, the samples were dispersed in acetone on metal stubs and gold coated. The SEM images were obtained from a Hitachi S-3400N scanning electron microscope.

3.2 Catalyst characterization

3.2.1 Transmission FTIR

The zeolite samples were pressed into self supporting wafers and placed inside a high pressure transmission cell. All samples were heated in synthetic air at 500 °C prior to reaction. For the MTH reaction Helium (He 6.0) was passed through methanol in a saturation evaporator kept at 0 °C and subsequently led to a High Temperature High Pressure Cell for FTIR from Specac kept at 350°C. The He flow was adjusted for each sample to give a WHSV of 2.0 g methanol per g catalyst per hour. During the calcination and reaction, spectra were recorded with a Bruker VERTEX 80 spectrometer using a DTGS detector at 4 cm^{-1} resolution and 2 mm aperture.

3.2.2 Diffuse Reflecance Infrared Fourier Transformed Spectroscopy, DRIFTS

The samples were pressed to wafers and subsequently crushed and sieved to obtain particles between 425 and 212 µm. Then a ceramic porous cup was filled with sample and the surface was smoothed. All samples were heated in synthetic air at 500 °C prior to reaction. For the MTH, reaction helium was passed through methanol in a saturation evaporator at 0°C and subsequently led to the DiffusIR IR-cell kept at the reaction temperature. The He flow was adjusted for each sample to give a WHSV of 2.0 g methanol per g catalyst per hour.

The spectra were recorded with a Bruker VERTEX 80 spectrometer with a LN-MCT detector at 1 cm^{-1} resolution and 2 mm aperture. Methanol was fed for 2 hours and 30 min before being switched off and the system was flushed with He at the same carrier gas flow and temperature for 30 min.

3.2.3 GC-MS

The effluents from the reaction were analyzed quantitatively and qualitatively by online GC-MS on an Agilent 7890A GC system with a 5975C MDS and a FID detector, recorded every 30 min starting from 5 or 10 minutes after introducing methanol.

Chapter 4

Results and Discussion

4.1 Characterization

The materials were characterized using SEM, XRD, ICP-MS, BET and FTIR. The results are presented below.

4.1.1 SEM investigation

All samples were investigated using SEM to estimate the size of agglomerates and primary particles. Due to a poor resolution of the SEM instrument, the value of the particle sizes are rough and their shape is for the most part not determined accurately.

4.1.1.1 ZSM-5

H-ZSM-5 13.5 SEM images obtained of ZSM-5 13.5 are shown in figure 4.1. Figure 4.1 (a) shows an overview, (b) and (c) a close-up of an agglomerate and (d) shows primary particles.

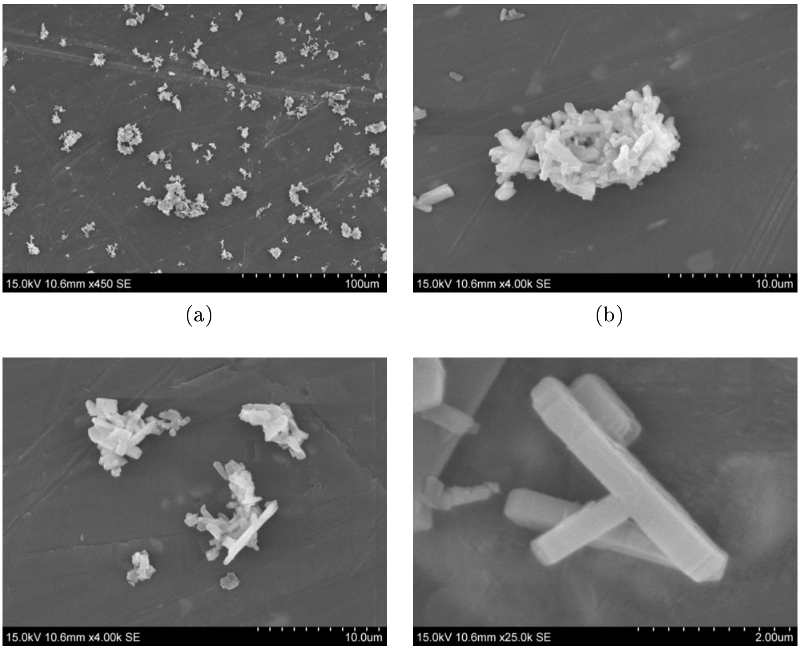

(a) (b) (c) (d)

Figure 4.1: SEM micrographs of ZSM-5 13.5. (a) an overview, (b) and (c) agglomerates and (d) close-up of a primary particle.

From figure 4.1 (a) and (b) it can be seen that the sample forms agglomerates between 30 and 10 µm without any distinct shape. Figure 4.1 (c) and (d) shows that some of the primary particles are rod shaped and between 1 and 4 µm long, while others are more disordered but still appear to have straight surfaces. The particle size and shape is consisted to that reported by other for the same topology [55].

H-ZSM-5 15 The SEM images of ZSM-5 15 are shown in figure 4.2. Figure 4.2 (a) shows a large agglomerate, (b) shows smaller agglomerates and debris, (c) shows a close-up of a small agglomerate and (d) shows a close-up of an agglomerate.

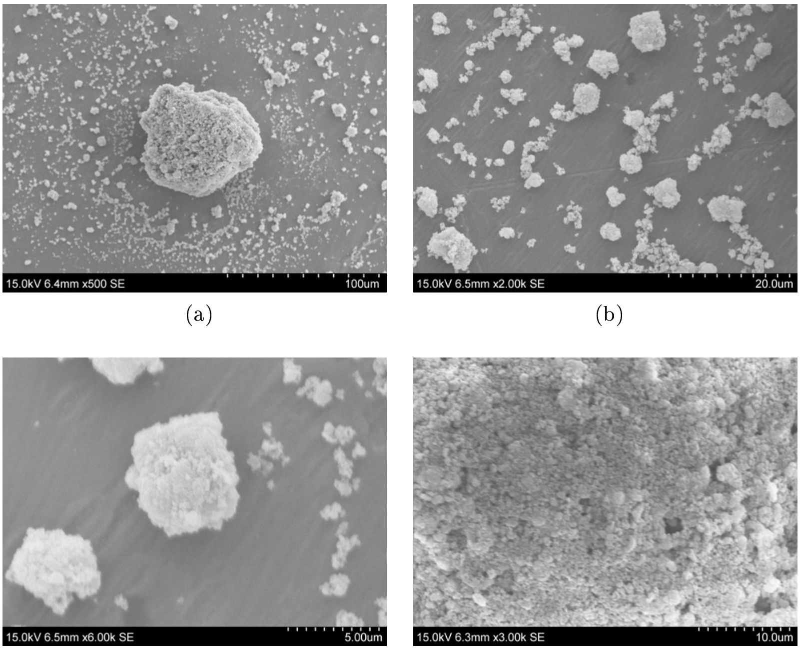

(a) (b)

(c) (d)

Figure 4.2: SEM micrographs of ZSM-5 15. (a) overview, (b) and (c) agglomerates and (d) close-up of an agglomerate.

Figure 4.2 shows that ZSM-5 15 forms round agglomerates up to 80 µm, although most are < 5 µm. Both agglomerates and crystals are irregularly shaped. Because of the poor resolution of the SEM-instrument it is hard to determine the particle size, but it appears to be smaller than 0.8 µm. The particle size is consisted to that reported by other for the same topology [56, 57].

H-ZSM-5 40 Figure 4.3 shows SEM images of ZSM-5 40. An overview is given in figure 4.3 (a) while (b) shows smaller agglomerates or debris. (c) shows a close-up of a small agglomerate.

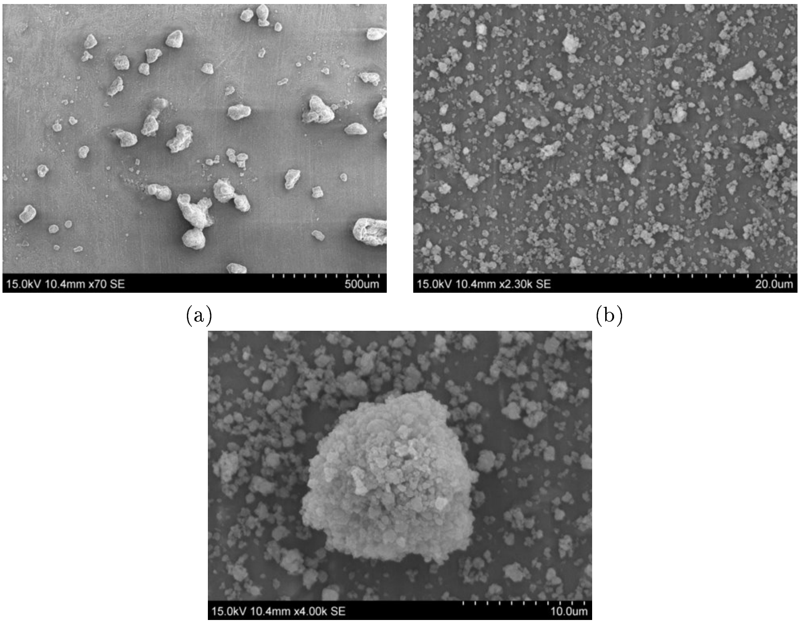

(a) (b)

(c)

Figure 4.3: SEM micrographs of ZSM-5 40. (a) overview, (b) small agglomerates and debris and (c) close-up of a small agglomerate.

From figure 4.3 it is evident that ZSM-5 40 forms agglomerates without any distinct shape, between 50 and 200 µm. The crystal size is again hard to determine, but seems to lie between 1 and 0.5 µm which is consistent with that reported by others [56, 57]. The irregular shape of the crystals is similar to reported values [58, 56, 55].

H-ZSM-5 45 SEM images obtained of ZSM-5 45 are shown in figure 4.4. (a) shows several large agglomerates, (b) smaller agglomerates and crystals and (c) a close-up of small agglomerates.

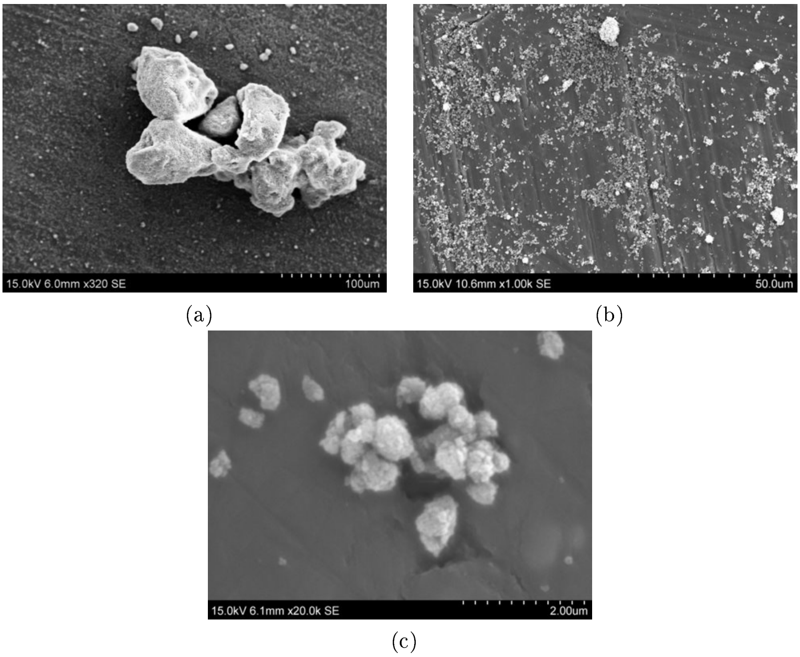

(a) (b)

(c)

Figure 4.4: SEM micrographs of ZSM-5 45. (a) large agglomerates, (b) small agglomerates and debris and (c) small agglomerates.

The agglomerates in figure 4.4 (a) are from 40 to 100 µm in size and do not have any distinct shape. The size of the smaller agglomerates ranges from 2.5 to 10 µm and they tend to be formed as even lumps. The crystal size is between 0.5 and 1 µm, and is consistent with that reported by others [56, 57]. As for ZSM-5 40 the crystals have irregular shape, as reported in other studies [58, 56].

4.1.1.2 Beta

H-Beta 12.5 Figure 4.5 shows SEM images of Beta 12.5. Figure 4.5 (a) shows an overview with several large agglomerates and (b) a close-up of smaller agglomerates.

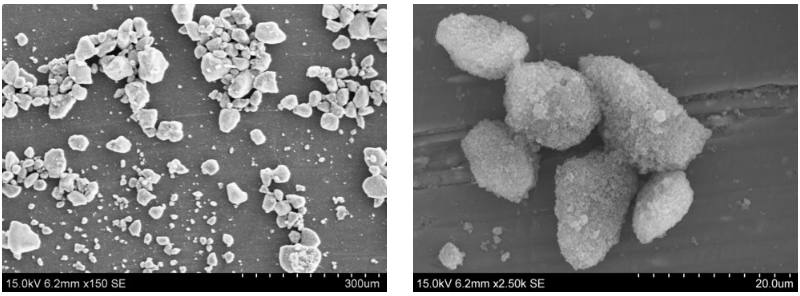

(a) (b)

Figure 4.5: SEM micrographs of Beta 12.5. (a) overview and (b) close-up of smaller agglomerates.

The sample forms agglomerates whithout any distinct shape. The size of the agglomerates are from 10 to 70 µm. The crystal size is hard to determine due to poor resolution, but can be estimated to 0.2-0.7 µm. The shape and size of the crystals are in correlation with those found in the litterature [59, 60, 61, 62].

H-Beta 12.5 2 SEM images of H-Beta 12.5 2 are shown in figure 4.6. Figure 4.6 (a) shows a large and several small agglomerates and (b) shows the surface of an agglomerate.

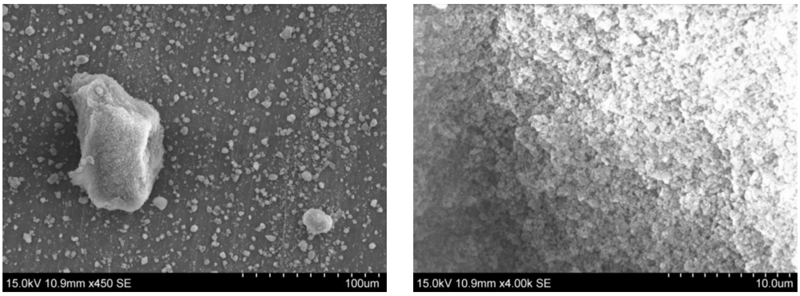

(a) (b)

Figure 4.6: SEM micrographs of H-Beta 12.5 2. (a) overview and (b) close-up of the surface of an agglomerate.

The large agglomerate is approximately 100 µm while the smaller are 5 - 20 µm and seems to form mostly round agglomerates. The crystal size is hard to determine, but appears to be lower than 0.4 µm. The shape and size of the crystals are in correlation with those found in the litterature [59, 60, 61, 62].

H-Beta 19 Figure 4.7 shows SEM images taken of Beta 19. Figure 4.7 (a) shows an overview, (b) shows the surface of an agglomerate and (c) shows a small agglomerate and primary particles.

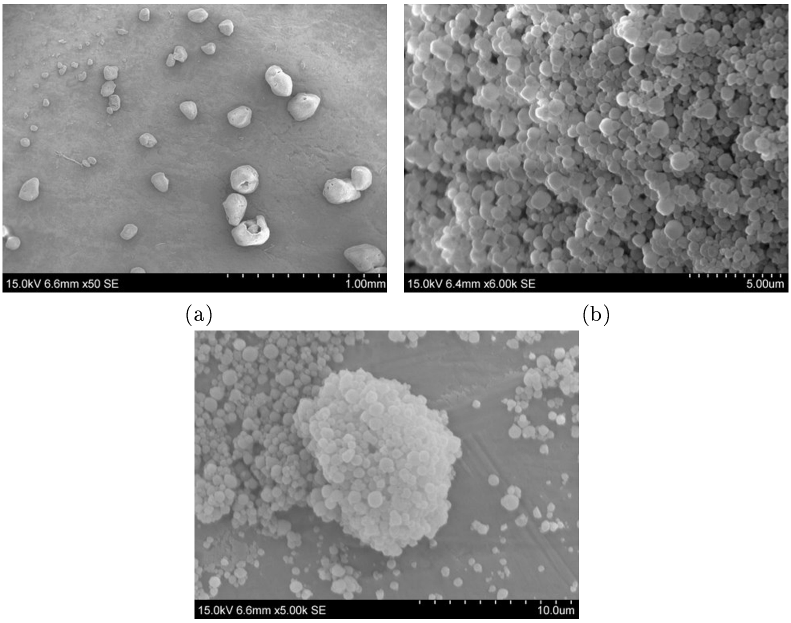

(a) (b)

(c)

Figure 4.7: SEM micrographs of Beta 19. (a) overview, (b) close-up of an agglomerate and (c) close-up of a small agglomerate.

From figure 4.7 it can be seen that Beta 19 forms agglomerates between 50 and 100 µm, somewhat larger than for the other two betas. The crystals had a spherical shape and were between 0.4 and 0.9 µm. The shape and size of the crystals are in correlation with those found in the litterature [59, 60, 61, 62].

4.1.1.3 Y zeolites

H-Y 15 Figure 4.8 shows SEM images obtained for Y 15. Figure 4.8 (a) shows an overview, (b) a close-up of an agglomerate, (c) small agglomerates and primary particles while (d) shows a close-up of primary particles.

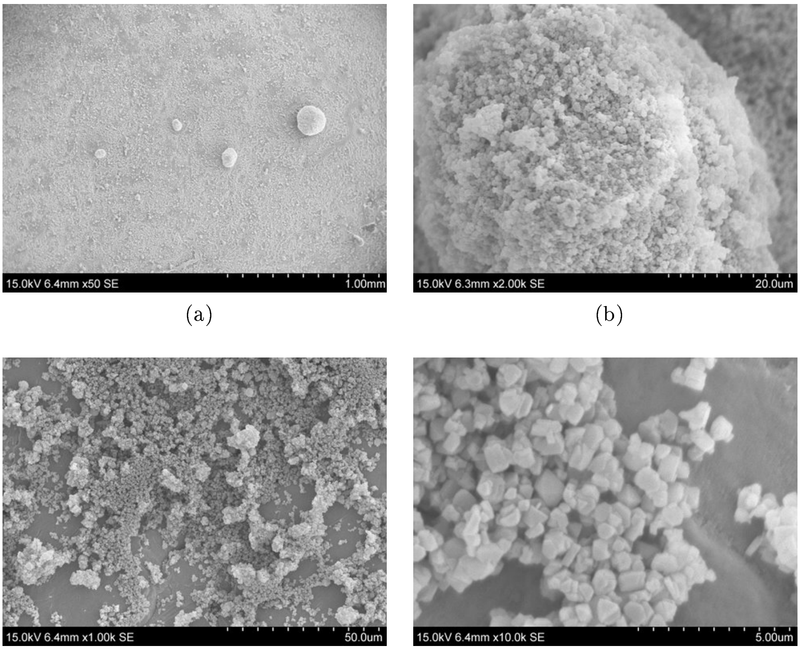

(a) (b)

(c) (d)

Figure 4.8: SEM micrographs of H-Y 15. (a) overview, (b) close-up of an agglomerate, (c) small agglomerates and primary particles and (d) close-up of primary particles.

As can be seen from figure 4.8, Y 15 does not form agglomerates to the same extent as the other samples, but those few formed are fairly large with sizes between 60 and 150 µm. The crystals seem to have smooth surfaces and straight edges with sizes around 0.9 µm as reported by others [59, 63].

H-Y 40 SEM images of Y 40 are shown in figure 4.9. (a) shows an overview, (b) small agglomerates, while (c) and (d) shows a close-up of a small agglomerate and crystals respectively.

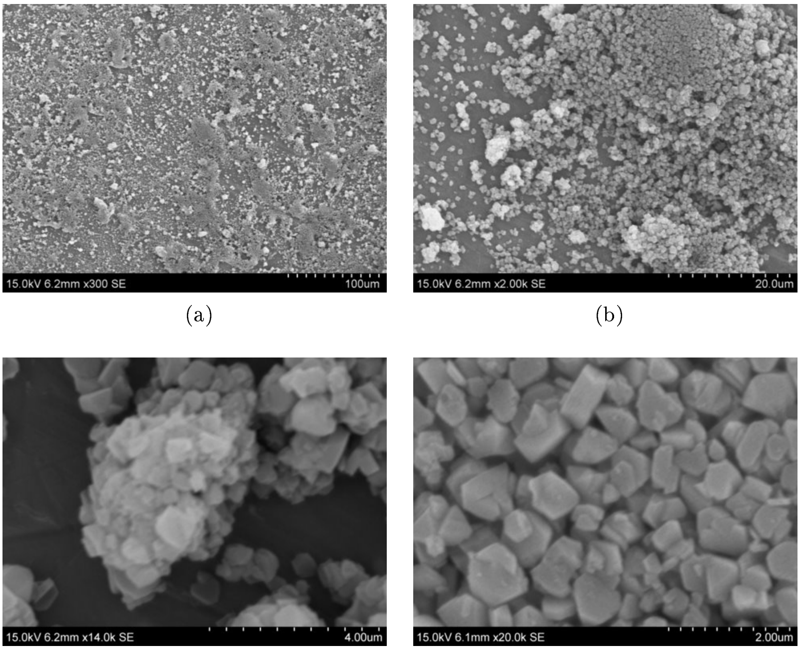

(a) (b)

(c) (d)

Figure 4.9: SEM micrographs of H-Y 40. (a) overview, (b) small agglomerates, (c) close-up of a small agglomerate and (d) close-up of primary particles.

From figure 4.9 it can be seen that Y 40 is very similar to Y 15. Neither form several large agglomerates, and the crystals are fairly ordered with smooth surfaces and sizes around 0.9 µm, as reported by others [59, 63].

4.1.1.4 H-MOR

Figure 4.10 shows SEM pictures of MOR. Figure 4.10 (a) shows an overview, (b) a close-up of a shell and (c) shows primary particles.

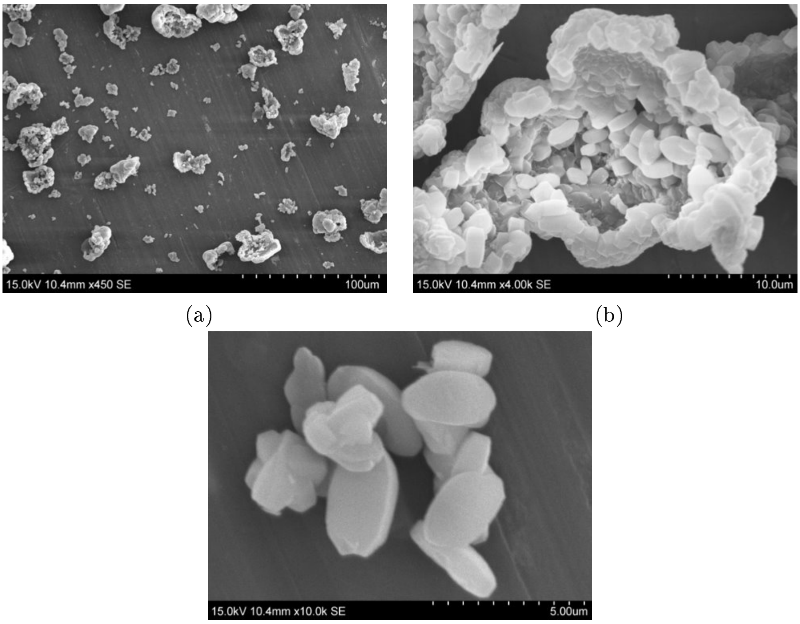

(a) (b)

(c)

Figure 4.10: SEM micrographs of MOR. (a) overview, (b) close-up of a shell and (c) close-up of primary particles.

Figure 4.10 (a) and (b) shows that the sample mainly consists of hollow sintered shells between 30 and 15 µm. The primary particles are disc-shaped and 1-3.5 µm, larger than any of the oter samples. The shape is somewhat similar as that reported by others for the same topology [64].

4.1.1.5 Silicalite

The SEM images obtained of the silicalite sample are shown in figure 4.11. (a) shows large agglomerates, (b) a close-up of agglomerates, (c) the surface of an agglomerate and (d) shows small agglomerates or debris.

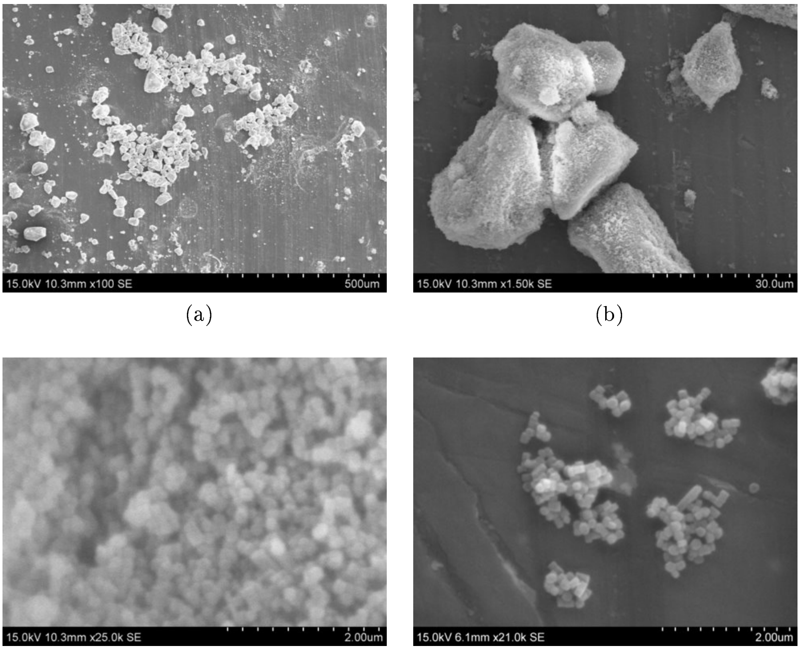

(a) (b)

(c) (d)

Figure 4.11: SEM micrographs of the silicalite sample. (a) overview, (b) close-up of agglomerates, (c) close-up of the surface of an agglomerate and (d) primary particles.

From figure 4.11 it can be seen that the sample forms agglomerates without a consistent shape, ranging from 40 to 90 µm in size. The crystal shape is almost cubic or spherical with sizes around 0.2 µm, but other shapes and sizes also occur. The shape and size of the crystals have been reported by Zhang and Jin for H-ZSM-5 crystallized without aging [65].

4.1.1.6 Summary

The approximate crystal size of the samples determined with SEM imaging is summarized in table 4.1. From the table the samples can be roughly divided into three groups based on their crystal strength. The samples with large particles are H-ZSM-5 13.5 and H-MOR, while the medium sized particles are found in H-ZSM-5 15, H-ZSM-5 40, H-Beta 19, H-Y 15 and Y 40. The samples with small particles are H-ZSM-5 45, H-Beta 12.5 and H-Beta 12.5 2.

Table 4.1: Approximate crystal size determined by SEM imaging.

Sample	Crystal size (µm)
H-ZSM-5 13.5	1 - 4
H-ZSM-5 15	$<$ 0.8
H-ZSM-5 40	0.5 - 1
H-ZSM-5 45	0.4 - 0.6
H-Beta 12.5	0.2 - 0.7
H-Beta 12.5 2	$<$ 0.4
H-Beta 19	0.4 - 0.9
H-Y 15	0.9
H-Y 40	0.9
H-MOR	1 - 3,5
Silicalite	0.2

4.1.2 XRD

All samples were examined using XRD to confirm phase purity and topology.

4.1.2.1 ZSM-5

XRD patterns of H-ZSM-5 13.5, H-ZSM-5 15, H-ZSM-5 40 and H-ZSM-5 45 are shown in figure 4.12.

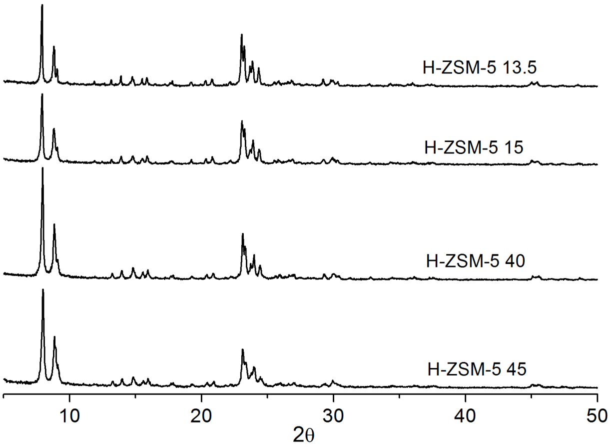

Figure 4.12: Powder X-ray diffractograms of the ZSM-5's.

As can be seen from the figure, all samples where of the same phase. The first peak for ZSM-5 13.5 seems narrower than the same peak for ZSM-5 45 which indicates a difference in crystal size. By comparing with published patterns, the phase purity and topology were confirmed [66, 56, 55].

4.1.2.2 Beta

Figure 4.13 shows XRD patterns of H-Beta 12.5, H-Beta 12.5 2 and H-Beta 19.

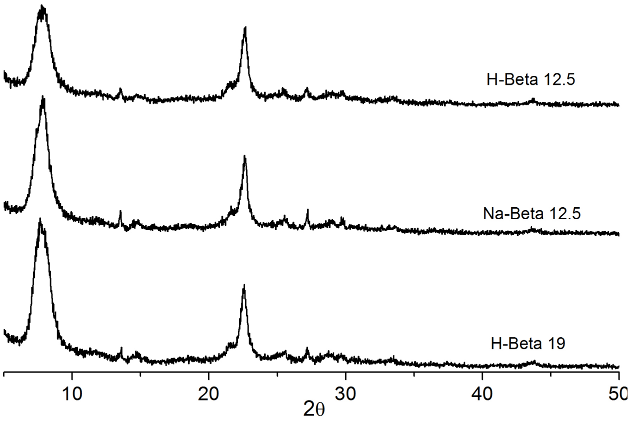

Figure 4.13: Powder X-ray diffractograms of the Betas.

The figure shows that all samples were of similar phase, comparison with published patterns confirms phase purity and topology [27, 67, 68]. The broad peaks are a result of the three polymorphs that the samples consist of.

4.1.2.3 Y zeolites

XRD patterns of H-Y 15 and H-Y 40 are shown in figure 4.14.

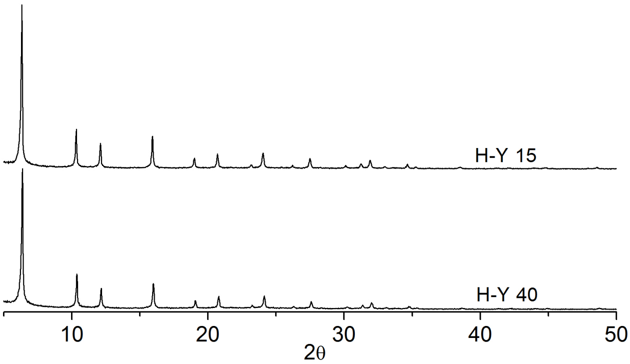

Figure 4.14: Powder X-ray diffractograms of the Y zeolites.

Both patterns contain the same intensities which shows that they are of the same phase. By comparing with patterns already published, the phase purity and topology were confirmed [69, 70, 63].

4.1.2.4 MOR

The XRD pattern of H-MOR is shown in figure 4.15.

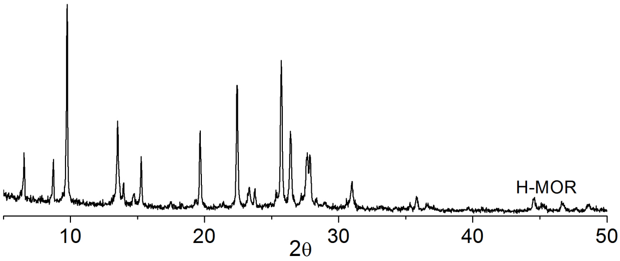

Figure 4.15: Powder X-ray diffractograms of the MOR.

Comparison with published patterns confirms phase purity and topology [64, 71].

4.1.2.5 Silicalite

The XRD pattern of the silicalite sample is shown in figure 4.16.

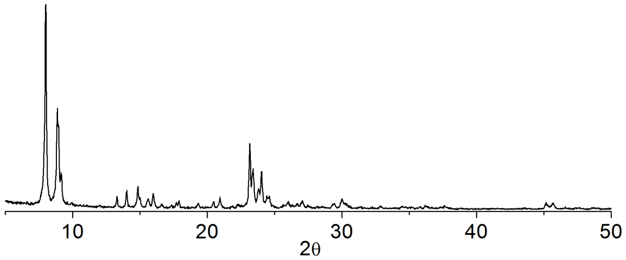

Figure 4.16: Powder X-ray diffractograms of the silicalite sample.

By comparing with published patterns, phase purity and topology is confirmed [66, 56, 55].

4.1.3 ICP-MS and BET

Si/Al ratios calculated from ICP-MS analysis of the samples and BET surface areas are shown in table 4.2. The table shows that the Si/Al ratios are very close to the values given by the suppliers, except values found for H-Y 40 and H-MOR which deviates to some extent. Although the aluminum value for the silicalite is above trace level, the sample contains very little aluminum and should not show any acidity. The BET surface area is as expected similar for each topology.

Table 4.2: Si/Al ratios calculated from ICP-MS and specific surface area from BET measurements of the samples.

Sample	Si/Al (ICP-MS)	Specific surface area from BET $\left(m^2/g\right)$
H-ZSM-5 13.5	13.78	317
H-ZSM-5 15	16.36	335
H-ZSM-5 40	42.23	358
H-ZSM-5 45	44.5	347
H-Beta 12.5	13.16	546
H-Beta 12.5 2	14.4	456
H-Beta 19	22.1	508
H-Y 15	15.25	647
H-Y 40	48.22	669
H-MOR	7.51	382
Silicalite	1436	331

A distinct correlation between pore and cavity diameters and BET values can be seen. The narrow 10-ring windows of the MFI topology give values around 340 m^2/g, while the larger 12-ring windows of the Beta zeolites give values around 500 m^2/g. The high value around 650 m^2/g for the Y zeolites is a result of the super cages. While the channels of MOR are 12-ringed, these are only one dimensional and the topology also contains 8-ringed channels. The surface area for MOR is therefore closer that of MFI topology than BEA*.

4.1.4 FTIR

FTIR was employed to investigate the nature and amount of the acidic sites as well as defects. Transmission FTIR spectra of the dehydrated samples are shown in figure 4.17. The ZSM-5 samples are shown in a), the betas in b) and the Y zeolites and MOR in c).

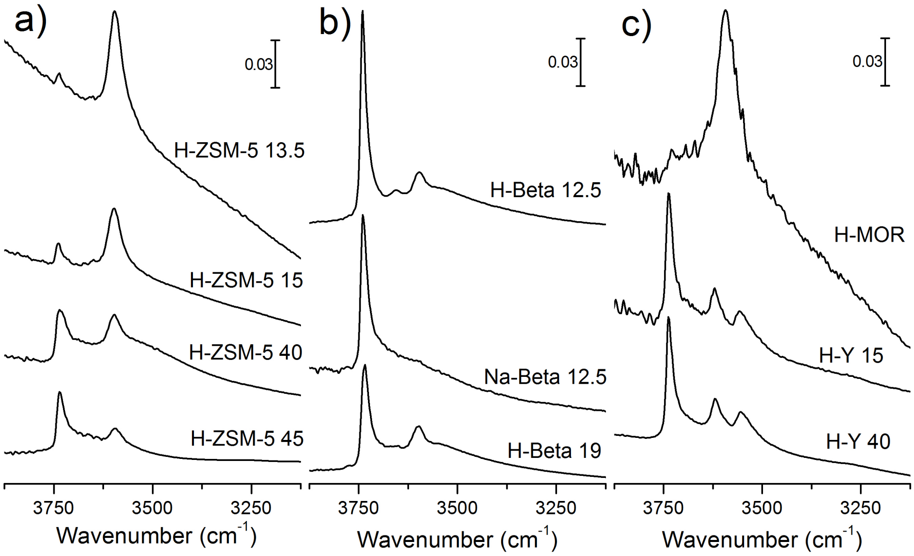

Figure 4.17: Transmission FTIR spectra of the dehydrated samples obtained at 350°C. All spectra have been normalized by weight.

4.1.4.1 ZSM-5

The ZSM-5 samples showed decreasing scattering profiles associated with decreasing crystal sizes, as also seen on the SEM images. All ZSM-5 samples are characterized by two bands around, one at 3738 cm^{-1} and the other at 3596 cm^{-1}, which is assigned to Brønsted acidic sites and silanols respectively. The intensity of the Brønsted band decreases for samples with higher Si/Al ratios. This is to be expected as samples with lower contents of aluminum have fewer acidic sites.

The silanol bands show an opposite trend, and increases with higher Si/Al. This is not directly related to aluminum content, but rather result from decreasing particle size which gives a higher surface to weight ratio. All silanol bands have a shoulder at lower frequencies from silanols on the internal surface. For H-ZSM-5 40, a broad band or shoulder can be seen at 3500 cm^{-1}. This band originates from silanols interacting with each other in silanol nests. H-ZSM-5 15 appears to contain a band at approximately 3660 cm^{-1} which is assigned to extra lattice aluminum [47].

4.1.4.2 Beta

H-Beta 12.5 and H-Beta 19 are both characterized by two bands, at 3600 and 3737 cm^{-1} as the previous samples, and the bands are assigned to Brønsted acidic sites and silanols respectively. The spectra of H-Beta 12.5 2 contains a band at 3737 cm^{-1} but does not show any band around 3600 cm^{-1} and does not seem to contain any Brønsted acidic sites. The absence of Brønsted acidic sites for this sample is somewhat unexpected as all samples have undergone the same pretreatment and the sample contains aluminum. The sample does not show any other bands associated with aluminum either.

Only H-Beta 12.5 2 shows any scattering profile and it is roughly the same as that of ZSM-5 15 and 40, this is not the same as seen on the SEM images. The sizes of the other two samples correlate well to the sizes determined from SEM. H-Beta 12.5 contains a well defined band at 3658 cm^{-1} which is assigned to extra lattice aluminum [47]. The spectra of both H-Beta 12.5 and 19 seem to contain a broad band or shoulder at 3540 cm^{-1} which is assigned to silanol nests.

4.1.4.3 Y zeolites

Both spectra of the Y zeolites are characterized by three bands. The first, at 3737 cm^{-1}, is assigned to silanols and the two others, at 3620 and 3553 cm^{-1}, are assigned high frequency (HF) and low frequency (LF) Brønsted acidic sites [34]. Both samples show a scattering profile at about the same magnitude as H-ZSM-5 15 and 40, as indicated by their size from the SEM investigation. None of the Y zeolites show bands related to defects or extra species.

4.1.4.4 MOR

The spectrum of H-MOR is very noisy and only one band at 3592 cm^{-1} can be distinguished, this band is assigned to Brønsted acidic sites. The band is the most intense of all Brønsted bands found in the samples. This is not surprising as H-MOR has the lowest Si/Al ratio. The spectrum shoes a very high scattering profile and indicates large particles, as shown by SEM investigation. Although no silanol band can be seen, this does not exclude the possibility of any being present because of the noisy spectra.

Due to the large particles it is expected that H-MOR contains few silanols and that the silanol band is very small, as for H-ZSM-5 13.5. The sample does not contain any major defects or extra species, but it is impossible to rule out small defects.

4.1.4.5 Summary

All samples except Beta 12.5 2 showed Brønsted acidic bands. Based on the information given by the supplier it was expected that all samples were acidic and the result is therefore a bit unexpected. The scattering profile of the samples except H-Beta 12.5 2 correlates well to the particle sizes determined for SEM microscopy, the scattering profile of H-Beta 12.5 2 was much higher than expected. The samples show a broad variety in both defects, particle size and acid site density.

4.2 Water desorption

Prior to the MTH reaction, all samples were heated in synthetic air in order to remove adsorbed water. In addition to being a necessary step, it also shows how the zeolites interact with water and can give information about the system, particularly the acidity. The proton affinity of H_2O is 166.5 kcal/mol, and it will typically form hydrogen-bonded species as shown in Scheme 3, adapted from [46].

SCHEME 3

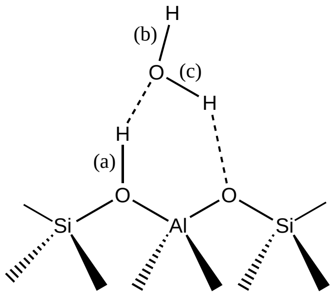

In Scheme 3 there are three types of O-H bonds, two from water and one from the zeolite. Modes from $v(\text{O-H})_\text{b}$ are nearly unperturbed and are found at wavenumbers close to that of the free water molecule. The two other modes are involved in hydrogen-bonds with oxygen and is downward shifted compared to the unperturbed bonds. The $v(\text{OH}\cdots\text{O})_\text{a}$ modes are of particular interest because these will be more shifted for strong acidic sites than for weak, and the shift can therefore be used to give an indication of the acidic strength of the zeolite.

Overtones of bending modes from bond (a) will interact with the $v(\mathrm{OH}\cdots\mathrm{O})_\mathrm{a}$ mode and cause Fermi resonance, there will therefore not be a single band, but two or three instead. To give an indication of the shift, the location of the Evans window is used.

At high water loadings several water molecules are known to form clusters which have a proton affinity high enough to deprotonate the zeolite (Scheme 4, adapted from [46]).

SCHEME 4

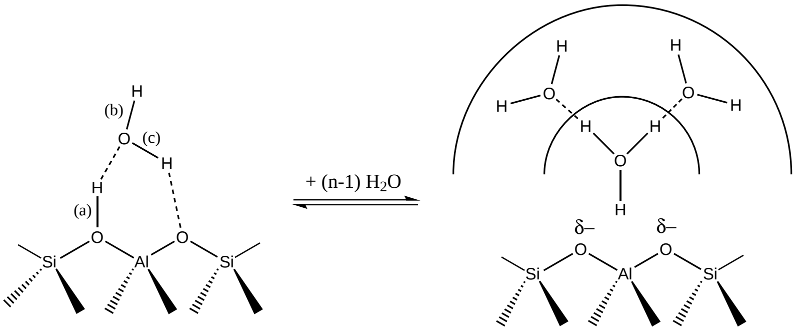

These clusters ability to deprotonate the acidic sites depends on the strength of the site and the number of water molecules in the cluster. As bond (a) is not present for the deprotonated specie, there will not be any Fermi resonance.

4.2.1 ZSM-5

The ZSM-5 samples have narrow pore diameters and are not expected to contain large amounts of water. Based on previous work, the acidic strength is expected to be fairly high [72].

H-ZSM-5 13.5 The spectra of the desorption of water from H-ZSM-5 13.5 are shown in figure 4.18. Figure 4.18 shows the actual spectra while figure 4.19 shows difference spectra. As can be seen on figure 4.18, the framework overtones shift as the temperature increases and water leaves the system. This creates false bands in the difference spectra, these false bands are marked with asterisks. The spectra can be divided into two groups, high and low loadings of water.

Starting with the highest water amount (spectrum 1), two broad bands at 3605, 3390 and a window at approximately 3270 cm^{-1} can be seen on a broad continuum from 1600 to 3600 cm^{-1}. The band at 3605 cm^{-1} could be a combination of more bands, and is together with the band at 3390 cm^{-1} assigned to vibrational modes of H_2O in outer spheres [73]. The band at 3390 cm^{-1} could also contain a component from $v(\mathrm{OH}\cdots\mathrm{O})$ modes of inner spheres. The window is a result

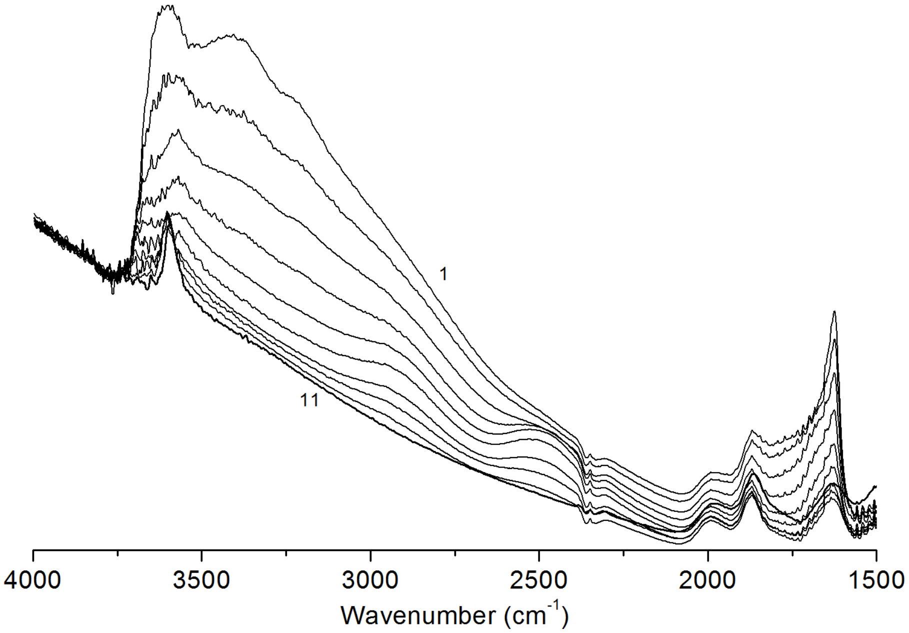

Figure 4.18: Transmission FTIR of the water desorption from H-ZSM-5 13.5. Starting temperature 50 °C (spectrum 1), 20 °C increase per spectrum to 230 °C (spectrum 10). Spectrum 11 collected at 500 °C.

of Fermi resonance between $v(\mathrm{OH}\cdots\mathrm{O})$ modes of inner spheres and overtones of $\gamma(\mathrm{H_2O})$. The continuum is associated with a variety of $\mathrm{H^+(H_2O)}_n$ species [73].

At lower frequencies a narrow band can be seen at 1625 cm^{-1} with an asymmetric shoulder on the high frequency side. The band is assigned to $\gamma(\mathrm{H_2O})$ modes of water in outer spheres while the shoulder is in part assigned to various bending modes of H_2O in both inner and outer spheres [74]. As the temperature increases, all bands lose intensity.

After reaching approximately 130 °C (spectrum 5), the features of a deprotonated zeolite are eroded and new features related to hydrogen-bonded species start to dominate the spectra. Most evident are the two bands at 2932 and 2490 cm^{-1} identified as an AB diad from Fermi resonance between $v(\mathrm{OH}\cdots\mathrm{O})_\mathrm{a}$ and an overtone of a bending mode, the Evans window is located at 2676 cm^{-1} [46]. The intensity of the A component is slightly higher than that of the B component. In the high frequency region two bands, at 3693 and approximately 3567 cm^{-1}, are present. These are assigned to $v(\mathrm{O\text{-}H})_\mathrm{b}$ and $v(\mathrm{OH}\cdots\mathrm{O})_\mathrm{c}$ respectively [73].

The Brønsted bands start to become visible after approximately 170 °C (spectrum 7) and continues to grow. The asymmetric band between 1840 and 1660 cm^{-1} is in part assigned to a C band of the ABC triplet caused by Fermi resonance, but

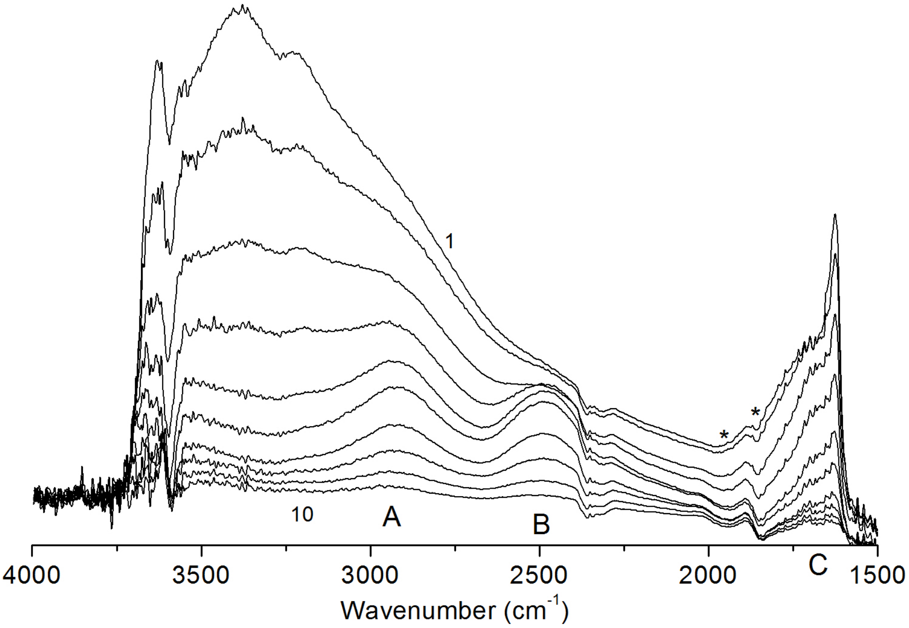

Figure 4.19: Transmission FTIR of the water desorption from H-ZSM-5 13.5. Starting temperature 50 °C (spectrum 1), 20 °C increase per spectrum to 230 °C (spectrum 10). Spectrum 11 collected at 500 °C. All spectra are difference spectra, where the spectrum of the calcined sample has been subtracted, asterisk indicates false bands.

could also contain components from remaining water clusters. The band at 1625 cm^{-1} is constantly diminishing but is present to approximately 210 °C (spectra 9).

These results confirm the assumption that when water is in surplus, water cluster are formed with a high enough proton affinity to deprotonate the Brønsted acidic sites. When surplus water leaves the system, only single water molecules remain adsorbed to the acidic sites. As the proton affinity of a single water molecule is too low to deprotonate the acidic site, it is instead hydrogen-bonded and Fermi resonance occurs. It should be noted that some clusters are present at high temperatures.

H-ZSM-5 15 The spectra of the desorption of water from H-ZSM-5 15 are shown in figure 4.20. The spectra are shown as difference spectra and have several similarities with those of H-ZSM-5 13.5, as expected given the same topology and close Si/Al ratio. There are some bands present from adsorbed hydrocarbons which burns off as the temperature increases. These species affect the framework overtones, but it is assumed that they don't affect the acidic strength.

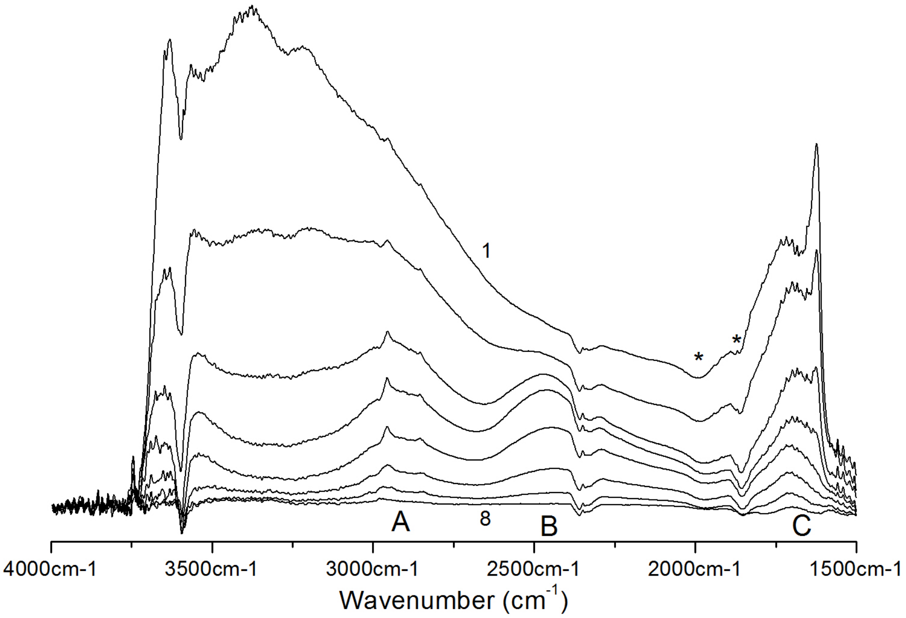

Figure 4.20: Transmission FTIR of the water desorption from H-ZSM-5 15. Starting temperature 50 °C (spectrum 1), 20 °C increase per spectrum to 190 °C (spectrum 8). All spectra are difference spectra where the spectrum of the calcined sample has been subtracted, asterisk indicates false bands.

The spectra of H-ZSM-5 15 at high water loadings has two bands, at 3610 and 3381 cm^{-1}, and a window at 3271 cm^{-1} on a broad continuum from 1600 to 3600 cm^{-1}. As earlier, the bands are assigned to $\upsilon(OH\cdots O)$ modes of inner and outer spheres, the window is a result of Fermi resonance between $\upsilon(OH\cdots O)$ modes of inner spheres and overtones of $\gamma(H_2O)$. The two small bands at 2957 and 2852 cm^{-1} are from hydrocarbons.

The band at 1626 cm^{-1} from $\gamma(H_2O)$ modes of water in outer spheres is also present, but what was seen as a high frequency tail for H-ZSM-5 13.5 is now a more separate band at 1719 cm^{-1}. The band is still assigned to various bending modes of H_2O in both inner and outer spheres [74].

Lower water loadings are reached earlier than for the previous sample, but we observe the same bands. The bands at 3670 and 3566 cm^{-1} are at similar positions, but all features associated with Fermi resonance appear at different wavenumbers. The A and B diad are found at 2925 and 2446 cm^{-1} respectively, both at lower wavenumbers. While the Evans window and the C component are found at 2682 and 1709 cm^{-1} respectively, both at higher wavenumbers.

The B and C components are more intense than for H-ZSM-5 13.5. All these changes can be attributed to a higher acidic strength of the Brønsted sites of H-ZSM-5 15, interacting with water through stronger H-bonds. The silanol bands does not change intensity to any extent, and no clear bands from species interacting with them are expected.

H-ZSM-5 40 The spectra of the desorption of water from H-ZSM-5 40 are shown in figure 4.21. This sample contains very small amounts of hydrocarbons at the start of the calcination. The spectra at higher water loadings are somewhat different than for the two previous samples. The band at 3616 cm^{-1} is less defined and the band at 3380 cm^{-1} is broader and dominates the region. No other bands are distinguishable in the high frequency region.

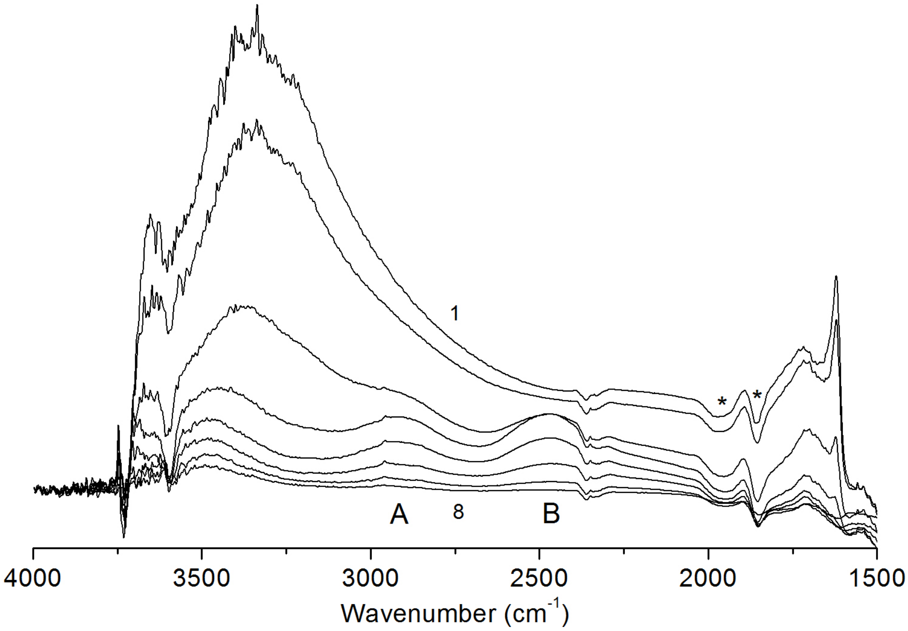

Figure 4.21: Transmission FTIR of the water desorption from H-ZSM-5 40. Starting temperature 50 °C (spectrum 1), 20 °C increase per spectrum to 190 °C (spectrum 8). All spectra are difference spectra where the spectrum of the calcined sample has been subtracted, asterisk indicates false bands.

In the low frequency region the same bands at 1718 and 1623 cm^{-1} from $\gamma(H_2O)$ modes of water in outer spheres are present. As for H-ZSM-5 15, the two bands are only partially overlapping. The band at 3747 cm^{-1} and negative band at 3733 cm^{-1} are the result of silanols shifting due to higher temperature (“hot bands”).

At lower water loadings two bands in the high frequency region can be seen, one at 3699 cm^{-1} assigned to $v(\text{O-H})_b$ and one at 3481 cm^{-1}. The latter could be assigned to hydrogen-bonded clusters, but the bending mode at 1623 cm^{-1} is not present and shows that there are no water clusters left in the pores. The A and B components are found at 2923 and 2460 cm^{-1} respectively, roughly the same as for H-ZSM-5 15. The Evans window is also found at a similar wavenumber, 2686 cm^{-1}.

The C component is hard to determine due to the shift in framework overtones. The B component is larger than A and what is assumed to be the C component has a moderate intensity. Based on these results it is clear that the acidic strength of H-ZSM-5 40 is higher than H-ZSM-5 13.5 and roughly the same as H-ZSM-5 15.

H-ZSM-5 45 The spectra of the desorption of water from H-ZSM-5 45 are shown in figure 4.22. The spectra shows the same features as the other H-ZSM-5's. There are moderate amounts of hydrocarbons adsorbed which also seems to affect the scattering profile of the spectra. Apart from this, only the features related to Fermi resonance will be discussed.

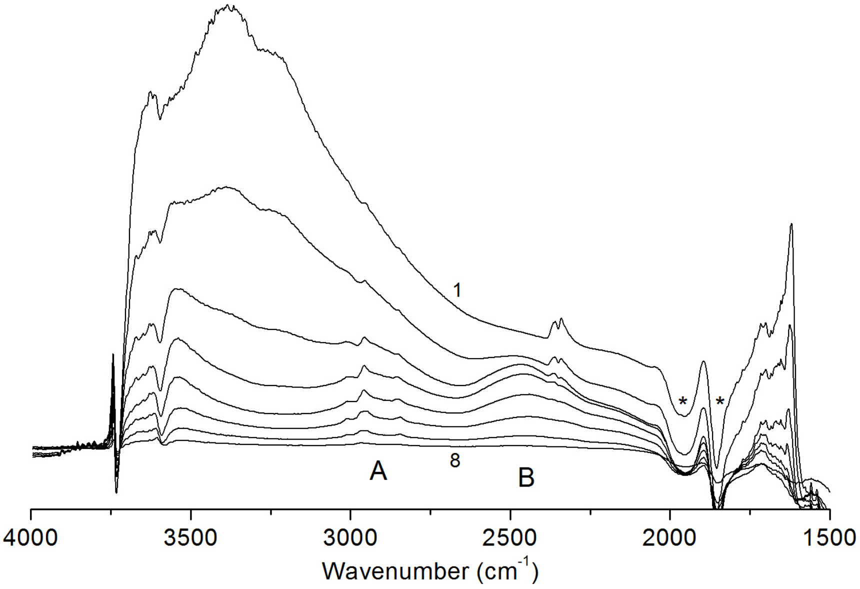

Figure 4.22: Transmission FTIR of the water desorption from H-ZSM-5 45. Starting temperature 50 °C (spectrum 1), 20 °C increase per spectrum to 190 °C (spectrum 8). All spectra are difference spectra where the spectrum of the calcined sample has been subtracted, asterisk indicates false bands.

The A and B component are located at 2923 and 2447 cm^{-1} respectively while the Evans window is found at 2673 cm^{-1}. The C component is hard to determine due to the strong shift in framework overtones but is located between 1600 and

1800 cm^{-1}. The intensity of the A and B components are similar, but B appears to be slightly more intense. The Evans window is located at a lower wavenumber compared to the two previous samples and is close to that of H-ZSM-5 13.5. Even though the high intensity of the B component indicates strong acidic sites, the Evans window indicates a strength closer to that of H-ZSM-5 13.5.

4.2.2 Beta

The Beta zeolites have a larger pore diameter than a ZSM-5 and are therefore expected to contain more water. The acidic strength of the two acidic betas are expected to be the same as the previous samples.

H-Beta 12.5 Spectra of the desorption of water from H-Beta 12.5 are shown in figure 4.23. The spectra are not very different from those of the ZSM-5 spectra, apart from a less pronounced Fermi resonance. Also on this sample are adsorbed hydrocarbons. At high water loadings, a broad and noisy band covers the region from 3700 to 2700 cm^{-1}. This band most likely consists of several bands associated with water clusters.

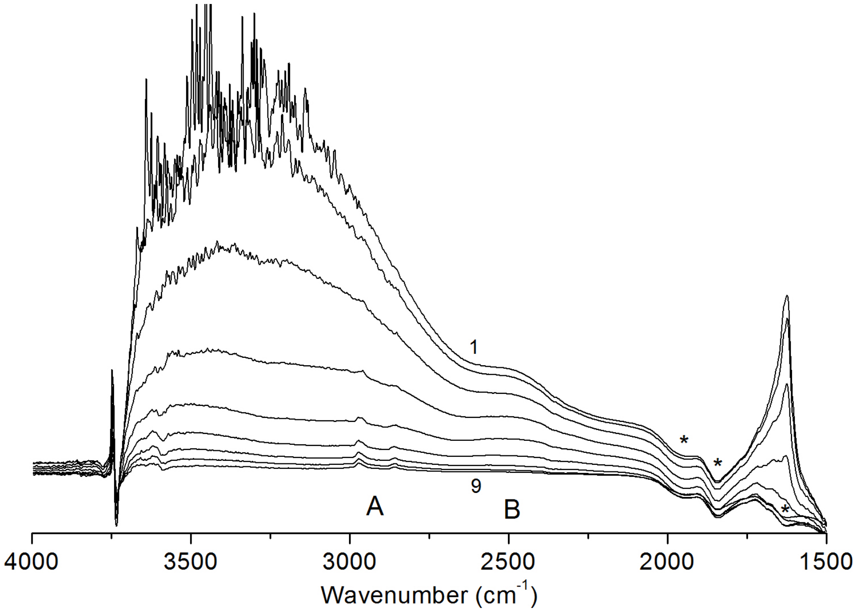

Figure 4.23: Transmission FTIR of the water desorption from H-Beta 12.5. Starting temperature 50 °C (spectrum 1), 20 °C increase per spectrum to 210 °C (spectrum 9). All spectra are difference spectra where the spectrum of the calcined sample has been subtracted, asterisk indicates false bands.

In the low frequency region, the band at 1627 cm^{-1} with a high frequency tail dominates. The band is assigned to $\gamma(H_2O)$ modes of water in outer spheres, as for the other samples. The intensity of the band seems higher than for the previous samples and indicates that more water is adsorbed. This is reasonable as the channel dimension of a Beta zeolite is higher than that of a ZSM-5, and the Betas showed a higher surface to weight ratio from BET.

At lower water loadings, Fermi resonance occurs. The intensity and location of the A component is hard to determine due to the adsorbed hydrocarbons but the location can be estimated to 2855 cm^{-1}. The B component is found at 2510 cm^{-1} and is less intense than A. The Evans window is located at 2660 cm^{-1}, lower than for all the ZSM-5's.

The C component is very hard to distinguish due to the shift in framework overtones and may not be present at all. In the high frequency region, a band at 3580 cm^{-1} is present. As the temperature increases, the band shifts to higher frequencies. The band is assigned to $\upsilon(OH)$ of hydrogen bonded water.

H-Beta 12.5 2 The spectra of the desorption of water from H-Beta 12.5 2 are shown in figure 4.24.

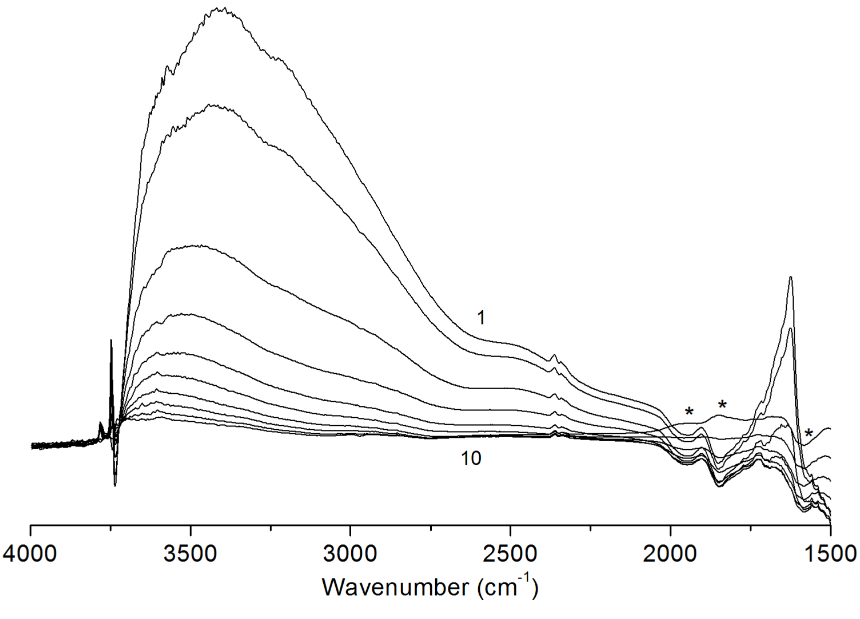

Figure 4.24: Transmission FTIR of the water desorption from H-Beta 12.5 2. Starting temperature 50 °C (spectrum 1), 20 °C increase per spectrum to 230 °C (spectrum 10). All spectra are difference spectra where the spectrum of the calcined sample has been subtracted, asterisk indicates false bands.

The spectra at higher water loadings show the same features as H-Beta 12.5 and will not be discussed further. As no Brønsted bands are shown for this sample, no Fermi resonance is expected. The spectra does however show the same features as H-Beta 12.5, although less pronounced, and the sample does not show the same features as samples on Na-form.

If Fermi resonance is present, the A component of the AB diad is much more intense than the B component and the Evans window can be approximated to 2650 cm^{-1}. While the results indicate some form of hydrogen-bonded interaction with Brønsted acidic sites, what these sites should be and where those bands should be located is not known.

H-Beta 19 The spectra of the desorption of water from H-Beta 19 are shown in figure 4.25. The spectra show much of the same as for the other acidic samples and only the features associated with Fermi resonance at low water loadings will be discussed. The A and B components at 2946 and 2490 cm^{-1} are much more defined than for H-Beta 12.5. The A component appear to be more intense than B, but this can also be the result of an elevation of the base line. The Evans window

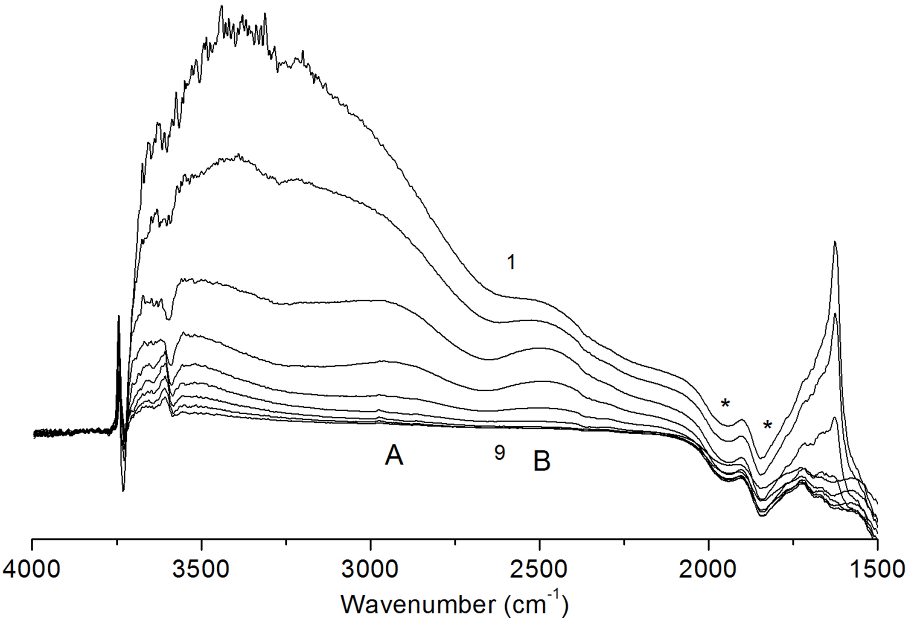

Figure 4.25: Transmission FTIR of the water desorption from H-Beta 19. Starting temperature 50 °C (spectrum 1), 20 °C increase per spectrum to 210 °C (spectrum 9). All spectra are difference spectra where the spectrum of the calcined sample has been subtracted, asterisk indicates false bands.

is found at 2660 cm^{-1}. The presence of any C band is hard to determine because of the shift in framework overtones.

4.2.3 Y zeolites

The Y zeolites have the largest pores and also contain super cages. They are therefore expected to contain large amounts of water compared to the other samples. Based on previous studies, the acidic strength is expected to be somewhat lower than for the other samples [72].

H-Y 15 Spectra of the desorption of water from H-Y 15 are shown in figure 4.26. The spectra does not show any Fermi resonance, and the only development is the diminishing of the initial bands. The lower acidic strength does not explain the absence of Fermi resonance, and it is more likely a result of topology rather than acidity.

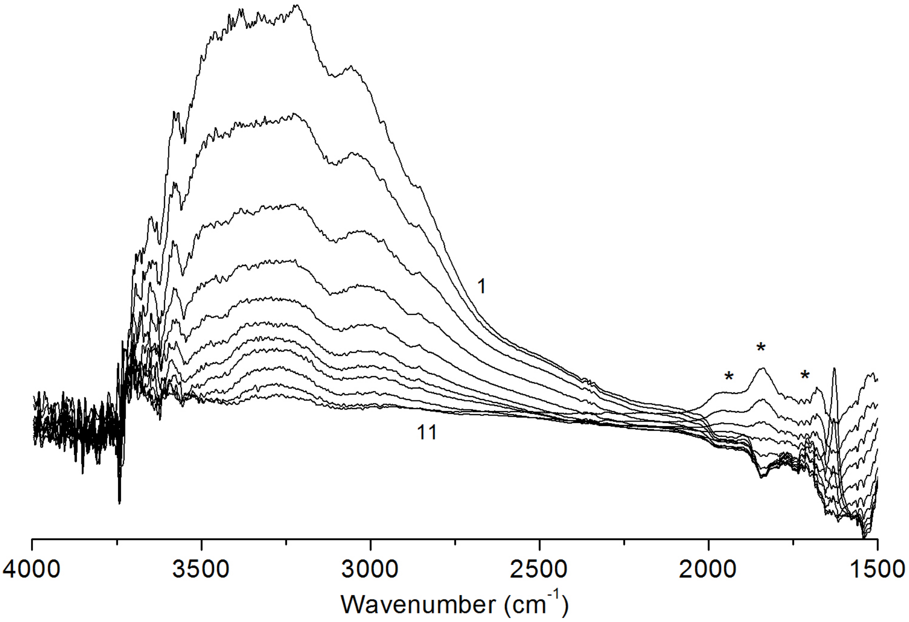

Figure 4.26: Transmission FTIR of the water desorption from H-Y 15. Starting temperature 50 °C (spectrum 1), 20 °C increase per spectrum to 250 °C (spectrum 11). All spectra are difference spectra where the spectrum of the calcined sample has been subtracted, asterisk indicates false bands.

Theoretical studies of water dimers adsorbed on H-FAU and H-ZSM-5 show that hydrogen-bonded complexes are not formed in H-FAU. This is because the complexes are not stabilized by spatial confinement in the supercages in a H-FAU, as they are in the smaller pores of a H-ZSM-5 [75]. All water present therefore forms ion exchanged complexes instead of hydrogen-bonded which would have caused Fermi resonance.

The bands present for H-Y 15 are at 3650, 3560, 3259, 3057, 2860, 2510 and 1623 cm^{-1}. All bands are assigned to stretching modes of various ion-pair complexes, except for the band at 1623 cm^{-1} which is still assigned to bending modes of water in ion complexes.

H-Y 40 Spectra of the desorption of water from H-Y 40 are shown in figure 4.27.

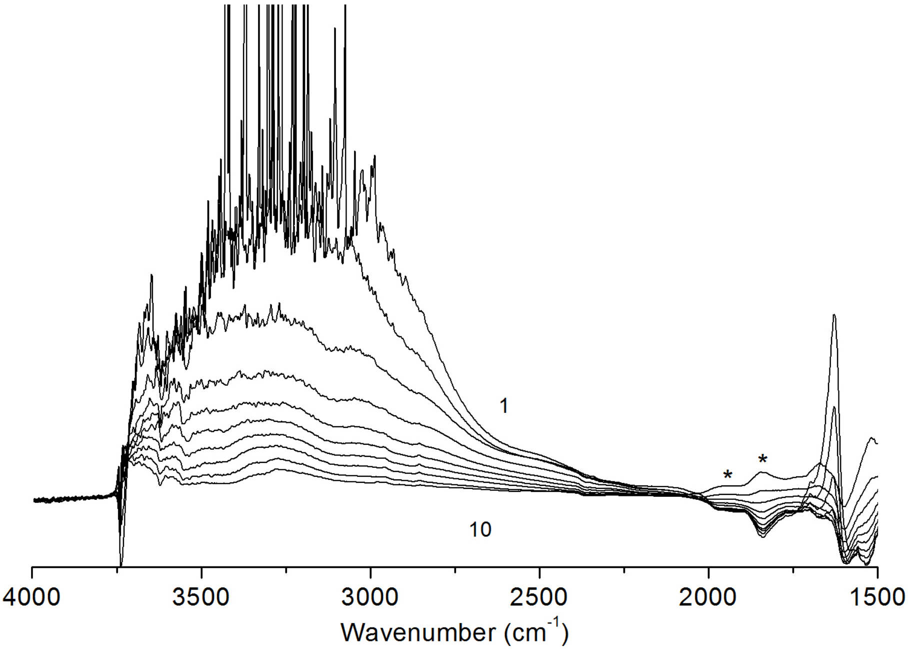

Figure 4.27: Transmission FTIR of the water desorption from H-Y 40. Starting temperature 50 °C (spectrum 1), 20 °C increase per spectrum to 230 °C (spectrum 10). All spectra are difference spectra where the spectrum of the calcined sample has been subtracted, asterisk indicates false bands.

The spectra for H-Y 40 shows the same bands as H-Y 15 both at high and low water loadings, the only difference being the more intense bands at higher loadings.

4.2.4 MOR

The spectra of the desorption of water from H-MOR are shown in figure 4.28.

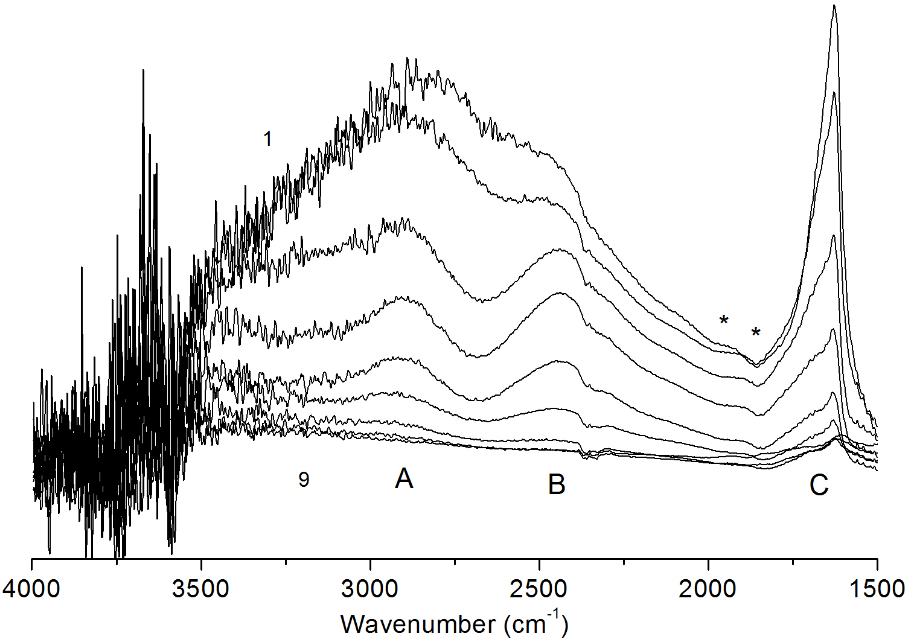

Figure 4.28: Transmission FTIR of the water desorption from H-MOR. Starting temperature 50 °C (spectrum 1), 20 °C increase per spectrum to 210 °C (spectrum 9). All spectra are difference spectra where the spectrum of the calcined sample has been subtracted, asterisk indicates false bands.

The spectra are very similar to those of the ZSM-5 samples except from a very noisy region between 3500 and 4000 cm^{-1}. At high water loading a broad continuum covers the region from 2300 to 3700 cm^{-1}. No bands can be identified in this region due to the noise, but the continuum is associated with various stretching modes of water in inner and outer clusters.

At lower loadings the ABC triplet from Fermi resonance appears. The wavenumber of the A, B and C component are 2913, 2440 and 1695 cm^{-1}. The Evans window is found at 2680 cm^{-1}, in the same region as the ZSM-5's. The band at 1632 cm^{-1} is present until almost all the water is removed. This shows the narrow pockets which stabilizes water clusters even at low water loadings [73]. The narrow pores also causes Fermi resonance to occur much earlier than for the Beta zeolites.

4.2.5 Acidity

The position of A and B diads and Evans windows associated with hydrogen-bonded complexes for the samples are summarized in table 4.3.

Table 4.3: Location of the A and B diad and Evans windows for the samples. The values for H-Beta 12.5 2 might be from bands not related to Fermi resonance.

Sample	A (cm^{-1})	B (cm^{-1})	Evans window (cm^{-1})
H-ZSM-5 13.5	2934	2490	2676
H-ZSM-5 15	2925	2446	2682
H-ZSM-5 40	2923	2460	2686
H-ZSM-5 45	2923	2447	2673
H-Beta 12.5	(2855)	3620	2660
H-Beta 12.5 2	(2915)	(2502)	(2650)
H-Beta 19	2946	2490	2660
H-Y 15	none	none	none
H-Y 40	none	none	none
H-MOR	2913	2440	2680

Based on the location of the Evans windows the relative acidic strength of the samples can be estimated to be H-ZSM-5 40 $\simeq$ H-ZSM-5 15 $\simeq$ H-MOR $>$ H-ZSM-5 13.5 $\simeq$ H-ZSM-5 45 $>$ H-Beta 12.5 $=$ H-Beta 19 $>$ H-Beta 12.5 2. The values for H-Beta 12.5 2 assumes that the sample is acidic. H-Y 15 and H-Y 40 show no Fermi resonance and are not included in the comparison, although their acidic strength is assumed to be lower that the other samples, based on other studies [72].

4.3 In-Situ Reaction Studies

The samples were investigated during the conversion of methanol to hydrocarbons. All samples were investigated using a transmission cell, and for selected samples the reaction was repeated using a DRIFTS cell. The transmission cell enables quantitative comparison of normalized data, but does not provide plug flow conditions. The DRIFTS cell is assumed to absorb more of the IR-beam at the surface of the sample and can therefore not be used for quantitative comparisons. The cell does however provide plug flow conditions, and the effluent analysis will show a more precise conversion and selectivity. Another drawback of the DRIFTS cell is that the region from 2000 cm^{-1} and below is obscured by framework vibrations and bands from δ(C-H), γ(C-H) and υ(C-C) modes are therefore hidden.

4.3.1 Transmission

4.3.1.1 General features

The reactions with the transmission cell were performed at 350 °C with WHSV=2 h^{-1}. Although the cell does not provide plug flow conditions, the selectivity of the various products should not be much affected. For an easier interpretation and comparison, the spectra have been divided into three regions. As these experiments are a screening, not all of the bands are assigned. This is also a result of the low sensitivity of the DTGS detector used, giving a noisy spectra which makes it difficult to assign bands. The MTH reaction produces water when methanol forms dimethyl ether, methoxy or methylates hydrocarbon pool species. This water is not properly flushed due to the lack of plug flow conditions, and will produce noise as the reaction time increases.

The first region ranges from 3800 to 3400 cm^{-1}. In this region Brønsted sites, silanols and defects will give rise to absorption bands. The second region ranges from 3100 to 2700 cm^{-1}. Here υ(C-H) modes from adsorbed hydrocarbons will appear. For the screening these two regions will be shown together. Because of the difference of slope, the spectra have been vertically shifted.

The third region ranges from 1700 to 1300 cm^{-1}. This region is shown as difference spectra, where the spectra of the calcined zeolite has been subtracted. Here bands from δ(C-H), γ(C-H) and υ(C-C) modes will appear during reaction. In methanol and dimethyl ether there are only hydrogen-carbon bonds and no carbon-carbon bonds. The presence of bands associated with carbon-hydrogen bonds will therefore confirm adsorption of methanol or dimethyl ether, but not necessary other hydrocarbons. While absorption bands associated with carbon-carbon bonds confirm some form of reaction.

From a catalytic viewpoint, the presence of some carbon-carbon bonds is desirable. The MTH-reaction needs hydrocarbons in the pool in order to proceed. But not all products are desired, especially not those who do not leave the system. A high intensity in carbon-carbon bonds does mean that the catalyst is producing a lot of products, but these are often dense and bulky. While heavy hydrocarbons can be a desired product, many of these species are very dense and remain trapped inside cavities, or do not leave the system for other reasons, and therefore blocks new reactions. Bands at 1600 and 1350 cm^{-1} are associated with such species, known as coke. Coke will not show in region 2 as it does not have any υ(C-H) modes.

4.3.1.2 ZSM-5

H-ZSM-5 13.5 Selected spectra of H-ZSM-5 13.5 during MTH-reaction are shown in figure 4.29. In region 1 it can be seen that the intensity of the Brønsted band, at 3595 cm^{-1}, decreases with increasing reaction time. There are no new bands between 3600 and 3200 cm^{-1} associated with perturbation of the Brønsted sites, so the sites are deprotonated. This indicates that one or more protonated species are adsorbed on the active sites of the zeolite. In region 2 new bands at 3000-2800 cm^{-1} also appear, and the intensity grows throughout the experiment. The first bands, at 2981 and 2870 cm^{-1}, are assigned to methoxy formed on Brønsted acid sites [76, 77].

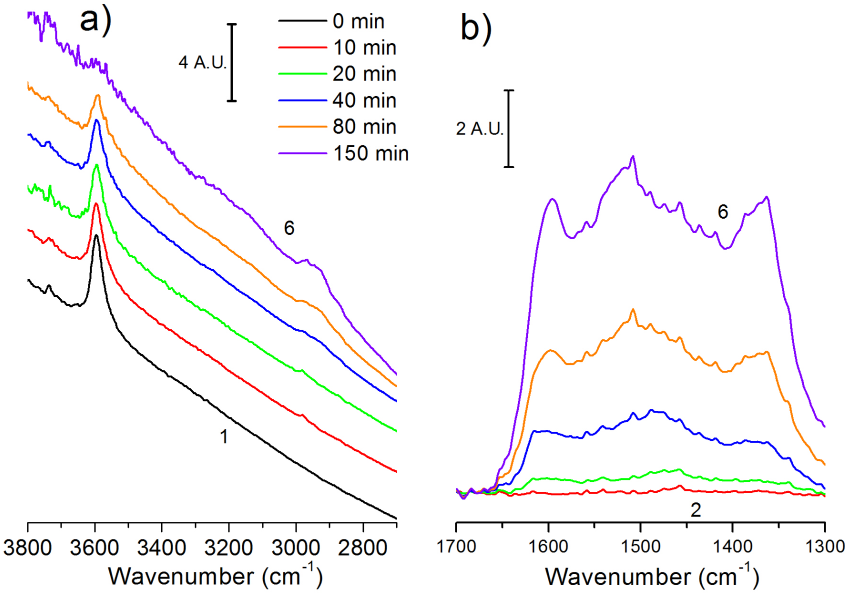

Figure 4.29: Selected FTIR transition spectra of H-ZSM-5 13.5 during MTH-reaction at 350 °C a) Region 1 and 2 is vertically translated b) Region 3 shows difference spectra. Spectra recorded 0, 10, 20, 40, 80 and 150 minutes after introducing methanol, spectrum 1 after 0 minutes.

For longer reaction times the shape of the spectra changes as bands appear at wavenumbers other than 2981 and 2870 cm^{-1}. These bands comes from hydrocarbons other than methanol, necessarily formed on the sample itself. As the reaction time increases the scattering profile also increases. This increase is associated with adsorption of species on the zeolite. After 150 minutes the Brønsted band has lost all it's intensity.

In region 3 more defined bands appear. After 40 min a band at 1615 cm^{-1} with a low frequency tail has grown, in addition to a small bands at 1649 cm^{-1} are present. There is also a band at 1482 cm^{-1} with a shoulder at 1463 cm^{-1} and broad band at 1377 cm^{-1}. There also seems to be other bands present, but only the well defined bands will be discussed. Bands around 1600 cm^{-1} are reported for coke species, but also for other C-C bonds [78, 79]. The sample is not expected to coke after 40 min, and the bands at 1615 and 1649 cm^{-1} are thus assigned to C-C and C=C modes of aromatics and oligomers respectively [79, 80, 81]. The band at 1482 cm^{-1} and shoulder at 1463 cm^{-1} is assigned to bending modes of CH_2 or CH_3, while the band at 1377 cm^{-1} is assigned to $\delta\,(CH_3)$ modes in oligomers and methyl groups [79, 26].

After 150 min the high frequency tail of the band at 1615 cm^{-1} has grown to a intense and well defined band at 1596 cm^{-1}, the band is still assigned to C-C and C=C modes of aromatics. A broad band at 1520 cm^{-1}also appears. This band might consist of several bands, but all are assigned to various aromatics. New bands between 1355 and 1395 cm^{-1} also grows, these bands are assigned to methyl groups [82].

The decrease of the Brønsted bands and the appearance of several bands in region 2 and 3 shows that methanol is adsorbed on the active sites of the zeolite, and that at least some methanol is converted to other hydrocarbons. The species formed primarily oligomers and aromatics.

H-ZSM-5 15, 40 and 45 Selected spectra of H-ZSM-5 15, 40 and 45 during MTH reaction are shown in figure 4.31 (a)-(f). The samples showed the same major features as H-ZSM-5 13.5 in region 1 and 2.

For all samples, the intensity of the Brønsted bands decreased with increasing reaction time, and new bands appeared in region 2. Unlike H-ZSM-5 13.5, these samples have silanols in addition to Brønsted sites, at approximately 3735 cm^{-1}. The silanols of H-ZSM-5 15 does not seem to lose much intensity, but the silanols of H-ZSM-5 40 and H-ZSM-5 45 loses allot of the initial intensity.

Another difference between the spectra from H-ZSM-5 13.5 and the rest is what appears to be the retention of the Brønsted band at high reaction times. It is unknown why the sample with the most intense initial Brønsted band should lose all of it's intensity while the other samples retain some, although the most apparent difference between H-ZSM-5 13.5 and the other ZSM-5 samples is the crystal size and presence of silanols. The band may also arise from perturbed silanols, which would not be present for H-ZSM-5 13.5 as it has no or very few silanols. The band for H-ZSM-5 15 should however not be as intense.

H-ZSM-5 15, 40 and 45 showed different shapes for the bands in region 2, and the time it took before more than two bands appeared varied. The difference in shape and relative intensities could appear because the samples yield different products, or that produced species interacts differently with the samples. The different interactions or produced species could result from the different Si/Al ratio of the samples, the different crystal sizes, amount of silanols or defects.

In region 3 there are some difference between all the ZSM-5 samples. The spectra of H-ZSM-5 15 at short reaction times shows a band at 1618 cm^{-1} and a broad band at 1375 cm^{-1}, as for H-ZSM-5 13.5. There is also a more narrow band at 1507 cm^{-1} present with a low frequency tail. This band is possibly present for H-ZSM-5 13.5, but it is much more intense for H-ZSM-5 15. The band is assigned to carbocationic species [83]. The lower intensity for the bands associated

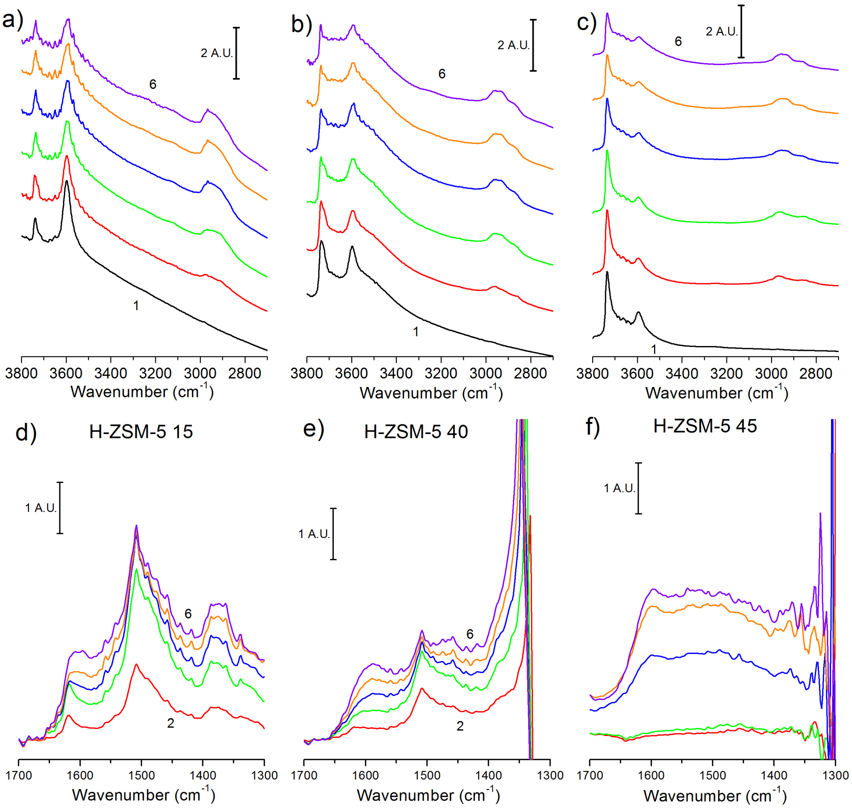

Figure 4.30: Selected FTIR transition spectra of H-ZSM-5 15 (a and d), H-ZSM-5 40 (b and e) and H-ZSM-5 45 (c and f) during MTH-reaction at 350 °C. Region 1 and 2 vertically translated, region 3 shows difference spectra. Spectra recorded 0, 10, 20, 40, 80 and 150 minutes after introducing methanol, spectrum 1 after 0 minutes.

with adsorbed hydrocarbons compared with H-ZSM-5 13.5 correlates well with the retention of the Brønsted band.

The spectra of region 3 for H-ZSM-5 40 shows the same bands as for H-ZSM-5 15 except from framework vibrations which are shifted to higher frequencies and hides some of the region. The band at 1618 cm^{-1} is shifted to lower frequencies for higher reaction times, and the band at 1460 cm^{-1} has a higher intensity than for H-ZSM-5 13.5. The broad band at 1375 cm^{-1} is partially hidden by the shift in framework vibrations, but seems to be present throughout the experiment. All bands are given the same assignments as for H-ZSM-5 15.

H-ZSM-5 45 shows a broad continuum from 1350 to 1600 in region 3 and only one band at 1596 cm^{-1} is well defined. The band is as for all other samples assigned to oligomers and aromatics. At frequencies below 1350 cm^{-1} the spectra are obscured by the shift in framework vibrations. Although no defined bands can be seen for the rest of the region, the continuum is assigned to aromatics and methyl groups as seen for the other samples.

4.3.1.3 Beta

Selected spectra of the Beta zeolites during MTH reaction are shown in figure 4.31.

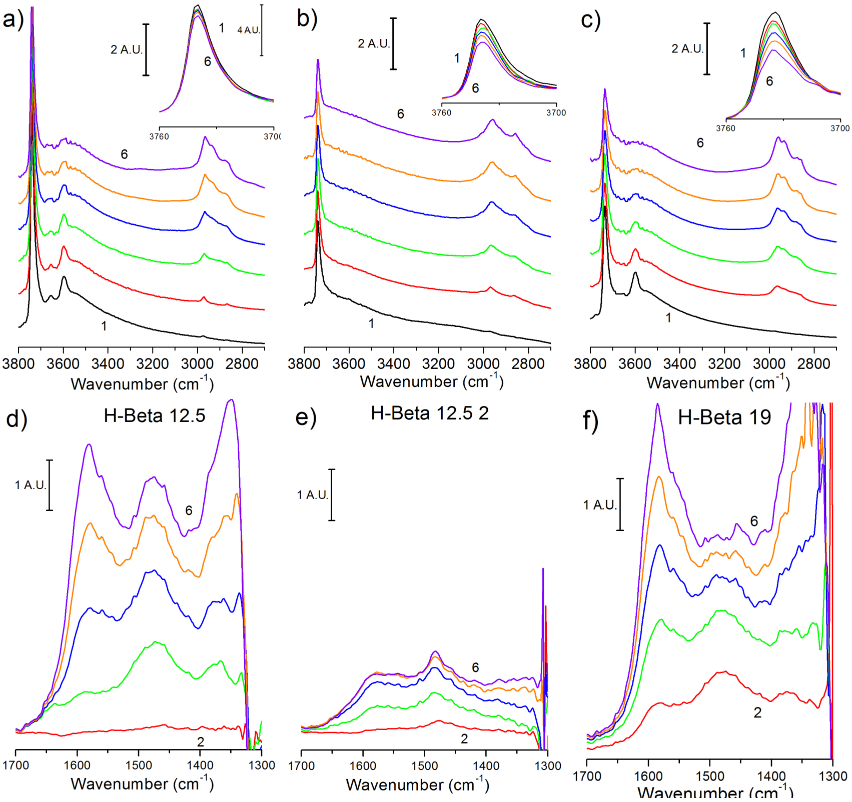

Figure 4.31: Selected FTIR transition spectra of H-Beta 12.5 (a and d), H-Beta 12.5 2 (b and e) and H-Beta 19 (c and f) during MTH-reaction at 350 °C. Region 1 and 2 vertically translated, region 3 shows difference spectra. Spectra recorded 0, 10, 20, 40, 80 and 150 minutes after introducing methanol, spectrum 1 after 0 minutes. Insets show the silanol band.

H-Beta 12.5 H-Beta 12.5, shown in figure 4.31 (a) and (d), had a few differences compared to the ZSM-5 samples. The Brønsted sites are consumed a a rate slightly higher than for the ZSM-5 samples, the silanols lose minor intensity throughout the experiment. In region 2 there seems to be the same bands as for H-ZSM-5 45 present, but with higher intensities. The higher intensity could be a result of different species being formed with high dipole moment, or that the larger pores of the Beta can adsorb more hydrocarbons. In region 3 the band at 1580 cm^{-1} is the most dominant, the band is as for all other samples assigned to aromatic species [82].

The broad band at 1475 cm^{-1} and the shoulder at 1382 cm^{-1} are the only other bands distinguishable, the band at 1350 cm^{-1} is the result of a shift in framework vibrations. The broad band at 1475 cm^{-1} is assigned to v(C-C) modes of aromatics [84]. The shoulder at 1382 cm^{-1} to methyl groups [82].

H-Beta 12.5 2 H-Beta 12.5 2 gave interesting results and is shown in figure 4.31 (b) and (e). Lacking Brønsted sites, the only development in region 1 and 2 is the partial consumption of the silanols and the growth of the bands at 3005, 2960 and 2854 cm^{-1}. The shape of the new bands does not change at longer reaction times. These bands are those of physisorbed methanol [76, 77]. In region 3 only three bands appear. The bands are located at 1577, 1482 and 1357 cm^{-1}. The bands at 1577 and 1482 cm^{-1} are assigned to aromatic species and v(C-C) modes of benzene respectively [84, 82], and the band at 1357 cm^{-1} is assigned to methyl groups [82]. This indicates that the sample catalyse reaction.

H-Beta 19 Selected spectra of H-Beta 19 during MTH reaction is shown in figure 4.31 (c) and (f). The spectra are similar to those for H-Beta 12.5 in region 1 and 2, both regarding shape and intensities of most bands. The exception is the much higher consumption of the silanols and the Brønsted bands. It can be seen that the low frequency tail of the silanol band is not consumed to the same extent as the main band. The Brønsted band has the same intensity as for H-Beta 12.5 before reaction, but the band is no longer visible after 1h and 20 min (spectrum 5) and only the band from the silanol nests remain.

In region 3 the same bands as for H-Beta 12.5 is present. The band at 1583 cm^{-1} is much more intense compared to the other bands in the region, and the band grows much faster than for H-Beta 12.5. This could be an indication that the sample accumulate hydrocarbons to a larger extent, and correlates well to the consumption of the brønsted bands. H-Beta 19 has a somewhat higher Si/Al ratio than Beta 12.5, but the acidic strength is similar, and a higher density of acidic sites should not result in a higher relative consumption.

4.3.1.4 Y zeolites

Selected spectra of the Y zeolites during MTH reaction are shown in figure 4.32

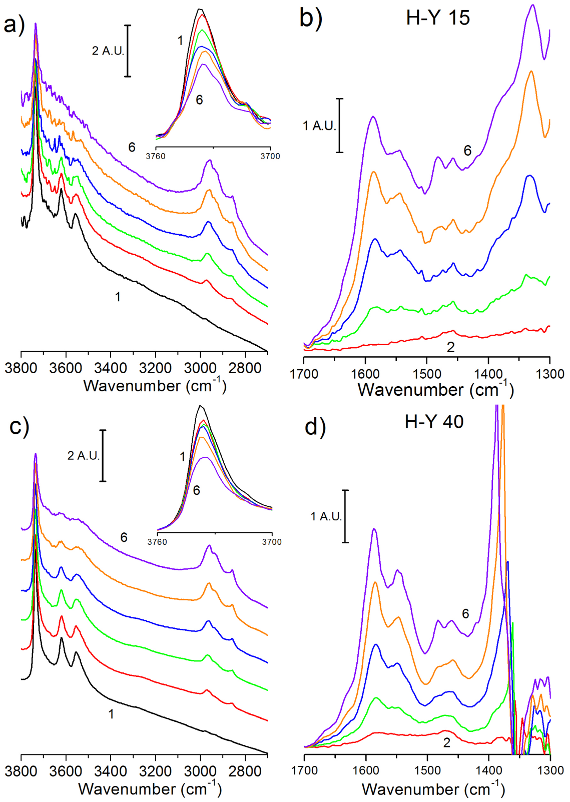

Figure 4.32: Selected FTIR transition spectra of H-Y15 (a and b) and H-Y 40 (c and d) during MTH-reaction at 350 °C. Region 1 and 2 is vertically translated, region 3 shows difference spectra. Spectra recorded 0, 10, 20, 40, 80 and 150 minutes after introducing methanol, spectrum 1 after 0 minutes. Insets show the silanol band.

H-Y 15 and 40 H-Y 15 and H-Y 40 showed much of the same features as the Beta zeolites. Both the HF and LF Brønsted sites seem to be consumed at a fairly similar rate, this indicates that the sites are equally accessible and that methanol has no problem interacting with either. The silanols are also consumed to some extent, again the low frequency tail is not consumed to the same extent as the main band.

The shape of the v(C-H) bands are fairly similar compared the other species. As the Y-zeolites have the largest cavities, heavier hydrocarbons are expected to form and these probably also gives rise to new bands. There does not seem to be any change in the bands other than the general intensity increase.

Region 3 is similar for the two samples at high frequencies. At lower frequencies the framework vibrations of H-Y 40 shift and disrupts bands below 1400 cm^{-1}. For both Y zeolites bands at 1588, 1547, 1483 and 1459 cm^{-1} are present. Both bands at 1588 and 1547 cm^{-1} are assigned to aromatics [85, 82]. The bands are well defined and has a moderate intensity. The bands at 1483 and 1459 cm^{-1} are assigned to various modes of alkenes [86].

For H-Y 15 a band at 1329 cm^{-1} and a shoulder at 1382 cm^{-1} can be observed at lower frequencies. The band at 1329 cm^{-1} could consist of several bands, but all are assigned to various modes of oligomers [81]. The shoulder at 1382 cm^{-1} is assigned to methyl groups [82]. These bands may also be present for H-Y 40, but they would be hidden by the shift of framework bands.

4.3.1.5 MOR

Selected spectra for H-MOR 10 are shown in figure 4.33. The spectra become very noisy after about 20 minutes, but it can be seen that the Brønsted sites are consumed and that bands appear in the υ(C-H) region. The reason for this noise is because the sample transmits to lite of the IR-beam when new species are adsorbed. In region 3, two bands with high intensities grow and dominates the whole region. At short reaction times, two bands are present at 1577 and 1400 cm^{-1}. The band at 1577 cm^{-1} is assigned to aromatic species while the other band at 1400 cm^{-1} is assigned to methyl groups [82]. Both coke bands grow quickly after methanol is introduced and shows the tendency of MOR to coke.

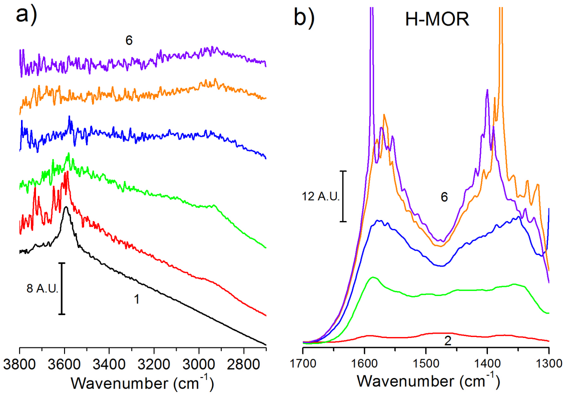

Figure 4.33: Selected FTIR transition spectra of H-MOR during MTH-reaction at 350 °C. Region 1 and 2 is vertically translated, region 3 shows difference spectra. Spectrum 1 before reaction.

4.3.1.6 Effluent analysis

The effluents from the reactions were analyzed by GC-MS-FID, although not all analysis were conducted with FID detector. The selectivity and conversion of selected samples after 50 min are shown in figure 4.34. It should be noted that the reactions are not conducted under plug flow conditions, so the conversions are only an indication. The figure shows that the samples produced a broad variety of species. The most interesting result is the conversion for H-Beta 12.5 2. This confirms the assignements on the IR-spectra of hydrocarbons other than methanol and dimethyl ether. It is not known how this sample could catalyze the MTH reaction without any visible Brønsted acidic sites. It should be noted though, that the sample contains aluminum.

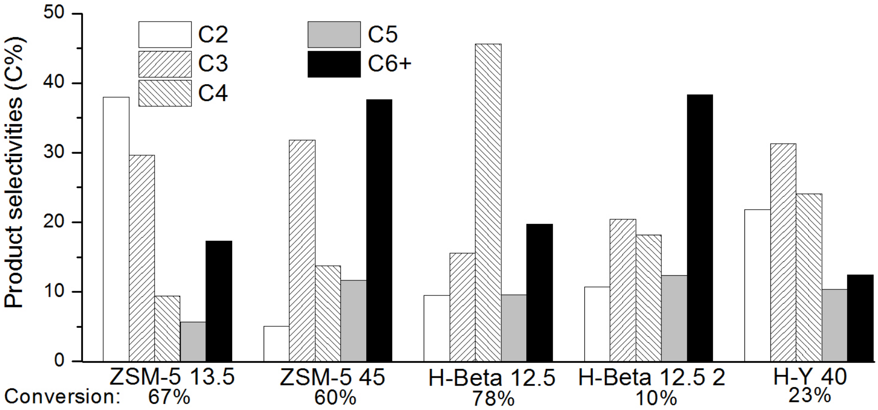

Figure 4.34: Product selectivity of H-ZSM-5 13.5, H-ZSM-5 45, H-Beta 12.5, H-Beta 12.5 2 and H-Y 40. Analysis performed after 50 or 60 minutes on stream.

It can be seen that in the early phase of reaction there are no clear trends, and that the selectivity is dependent on more parameters than topology alone. H-Y for instance has large volumes able to produce complex structures, but it also yields ethylene and propene. H-MOR shows a low conversion after 20 minutes, this is most likely because the system has been deactivated by coking.

Figure 4.35 shows the higher retention times of the FID chromatograms of H-ZSM-5 45, H-Beta 12.5 and H-Y 40, recorded after 50 minutes on stream. In this region the methylated benzenes are detected. As can be seen, H-ZSM-5 45 does not produce species larger than tetramethylbenzene (Tetra-MB) to any extent. The tetramethylbenzene formed is most likely durene. The reason for the lack of species larger than Tetra-MB is the restrictions caused by the narrow pore diameter of the MFI topology, which prevents more bulky molecules from being formed. The minor intensity at higher retention time is most likely from species formed at the surface of the zeolite. It should also be noted that the most abundant polymethylbenzene

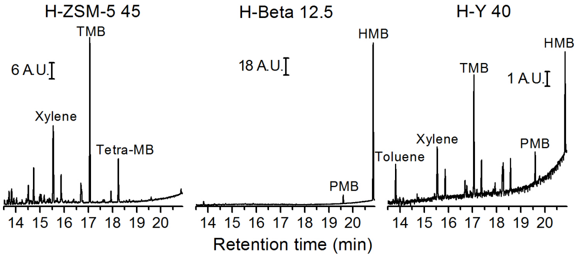

Figure 4.35: FID chromatogram of H-ZSM-5 45, H-Beta 12.5 and H-Y 50 showing higher retention times.

for H-ZSM-5 45 is trimethylbenzene which is considered to be the most reactive hydrocarbon pool specie for this topology.

H-Beta 12.5 produces some pentamethylbenzene, but HMB is by far the most dominating specie of this region, also this specie is considered to be the most reactive hydrocarbon pool specie for this topology. H-Y 40 produces a variety of methylated benzenes. While more branched or polycyclic hydrocarbons are most likely formed inside the supercages of H-Y, the 12-ring windows are too narrow for these species to leave. At lower retention times the samples produced mostly the same species in different amounts.

The entire FID chromatogram of the effluent analysis for H-ZSM-5 45 is shown in figure 4.36. The figure shows the variety of species formed and gives an indication

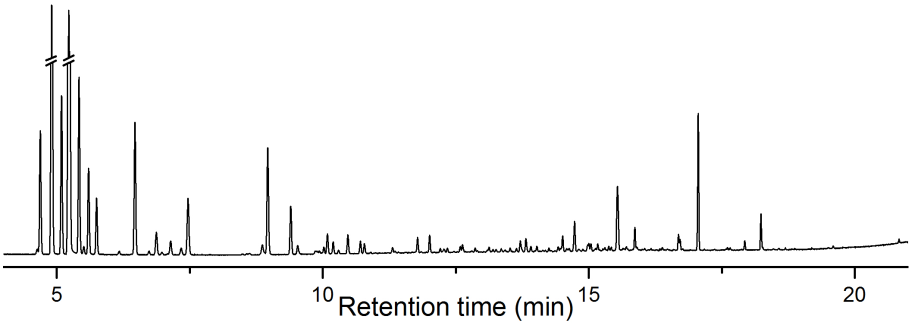

Figure 4.36: FID chromatogram of H-ZSM-5 45 recorded after 20 min. The peaks from propene, methanol and isobutane have been cut to show the intensities of the smaller peaks.

of the complexity of the IR-spectra. The most intense peaks, from propane and methanol and isobutane, have been cut.

4.3.1.7 Summary

The IR-spectra of the screening showed bands associated with various hydrocarbons for all samples, even H-Beta 12.5 2. It is not surprising that the other samples show a conversion, but it is unexpected for a sample showing no Brønsted acidity to catalyze the MTH reaction. It is not known what this is caused by. The development of the υ(C-H) bands shapes for some of the acidic samples over time indicates that the reaction undergoes different phases. The complex shape of the bands in both region 2 and 3 shows the broad variety of species formed during the MTH reaction, which is also confirmed by the effluent analysis. An interesting result is that both the ZSM-5 and Beta zeolites showing high intensity silanol bands seem to keep some of the intensity of the Brønsted bands.

Another result is the different bands shown in region 3 for the different topologies. The ZSM-5 samples showed bands assigned to both aromatics and oligomers, H-ZSM-5 13.5 showed some higher intensity for the bands assigned to aromatics than the other did. The effluents of H-ZSM-5 13.5 contained fewer heavy hydrocarbons than H-ZSM-5 45 and this could indicate that H-ZSM-5 13.5 accumelates the aromatics to a larger extent than the other ZSM-5 samples. This higher accumulation might be a result of higher density of acidic sites or larger crystals, which could allow the sample to retain more aromatics.

H-Beta 12.5 and H-Beta 19 both showed a high intensity of bands assigned to aromatics, and any bands from oligomers are hidden under these more dominant bands. It should be noted that the lower frequencies of the Beta zeolites are obscured by framework vibrations, and that this may hide som of the bands form oligomers. Again, a high intensity of aromatics in the IR-spectra are followed by a lower amount of heavy hydrocarbons in the effluents.

H-Beta 12.5 2 also showed some bands associated with methylated aromatics, although the intensity was less than for the other Beta zeolites. H-Beta 12.5 2 has showed several unexpected and contradictory results for all experiments using FTIR. It shows a higher scattering profile than suggested by the crystal size determined by SEM, and lacks Brønsted bands or any other bands associated with aluminum, although aluminum is confirmed in the sample by ICP-MS. In addition, the sample shows bands associated with hydrocarbons during MTH reaction and the effluent analysis confirm that methanol is converted to other species.

One possible explanation for these strange results is that the sample could already contain hydrocarbons, or some other species, on the Brønsted sites which is not burned off during the calcination. This could explain both the higher scattering profile as well as the absence of Brønsted bands in the spectra. If the possible hydrocarbons present are not to condense they may still act as hydrocarbon pool species, thus allowing for some conversion. In order to verify this assumption, the sample should be investigated again by in-situ FTIR calcination, possibly at higher temperature or for a longer period.

H-Y 15 and H-Y 40 both showed bands from aromatics and alkenes. The bands where more narrow than for the other topologies, and could indicate that fewer types of species are adsorbed. It could be that the band at 1588 cm^{-1} is from condense hydrocarbons.

The coke bands of H-MOR grow quickly and dominates region 3, while the Brønsted bands are fully consumed. This shows the tendency for this topology to coke. It is not known if the very broad bands for H-MOR are a direct consequence of coke, but the sample shows a low conversion.

The reactions are neither conducted under the right conditions or for a long enough time to draw any conclusions of the coking based on the effluent analysis or IR-spectra.

While the process of coking is interesting both from a scientific and an industrial point of view, this work will focus on the formation of desired products during the steady-state phase. A more detailed analysis of what happens on the catalyst as the reaction occurs will be made, as well as a more precise analysis of the products formed. To reduce the time scale and amount of data only two of the samples will be investigated further, and further investigation of H-Beta 12.5 2 will not be made. To make the analysis more comprehensive, the samples will have few side reactions and be as similar as possible.

As the ZSM-5 samples showed little sign of coking and has narrow pores which limits side reactions, this is the topology which will be investigated further. H-ZSM-5 13.5 and 15 were without significant defects, have a close Si/Al ratio but a very different crystal size, and are therefore chosen as the two samples to be investigated further.

4.3.2 DRIFTS

For the closer investigation a DRIFTS cell has been used. This is to ensure that the reaction is conducted under plug flow condition for an adequate analysis of the effluent products. Although region 3 will be covered by framework overtones, this study does not focus on the formation of coke and region 3 is therefore not very important. Another change is the use of a LN-MCT detector. This detector is much faster and more sensitive than the DTGS detector used for the screening experiments. As a result, the new spectra will have a higher signal to noise ratio and a higher time resolution.

The two samples used for the study are very similar except from the particle size. H-ZSM-5 13.5 has very large particles and therefore contains very few silanols compared to H-ZSM-5 15 which has small particles. This is the only major difference between the samples and should help the assignment of bands. To further ease the assignment of bands, the reaction was conducted at four different temperatures for both the samples. This provides spectra of increasing complexity, as many of the reactions do not occur at the lower temperatures. Bands present at the lower temperatures can more easily be identified as there are fewer potential species, in addition to fewer overlapping bands.

4.3.2.1 H-ZSM-5 13.5

Of the two ZSM-5 samples chosen for the closer investigation, H-ZSM-5 13.5 shows the simplest spectrum of region 1. It has a large particle size, and therefore few silanols, it also has few defects. Therefore, the most intense bands in region 2 are expected to appear from hydrocarbons physisorbed on the framework or interacting with Brønsted acidic sites.

Reaction at 200°C The first reaction was performed at 200 °C on H-ZSM-5 13.5, spectra are shown in figure 4.37 and 4.38. Figure 4.37 shows a 3D spectra of the whole reaction while figure 4.38 shows selected spectra. From figure 4.37 it can be seen that the Brønsted sites are consumed during the start of the experiment and that bands appear in region 2. Two broad bands at 2920 and 2350 cm^{-1} can also be seen. These bands are the first two components of an ABC triplet caused by Fermi resonance of the stretching and overtones of the bending modes of the Brønsted sites interacting with methanol through hydrogen-bonds [77, 46]. The C component (not shown) is located on framework overtones and is hard to distinguish. In figure 4.38 the location and intensity of the bands can be seen in more detail.

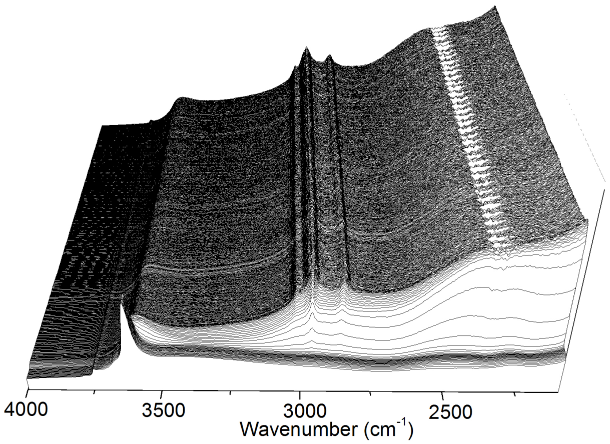

Figure 4.37: DRIFTS spectra of H-ZSM-5 13.5 during MTH-reaction at 200°C.

In region 1, a consumption of the Brønsted band can be seen, and a broad band around 3578 cm^{-1} is evident after 2 min. The band shifts to lower frequencies and seems to lose intensity, but this may also be because it is superimposed on a decreasing Brønsted band. Bands associated with perturbed silanols are expected around these wavenumbers, and the silanols do lose some intensity. The silanol band is however too weak to support the assumption, in addition the intensity

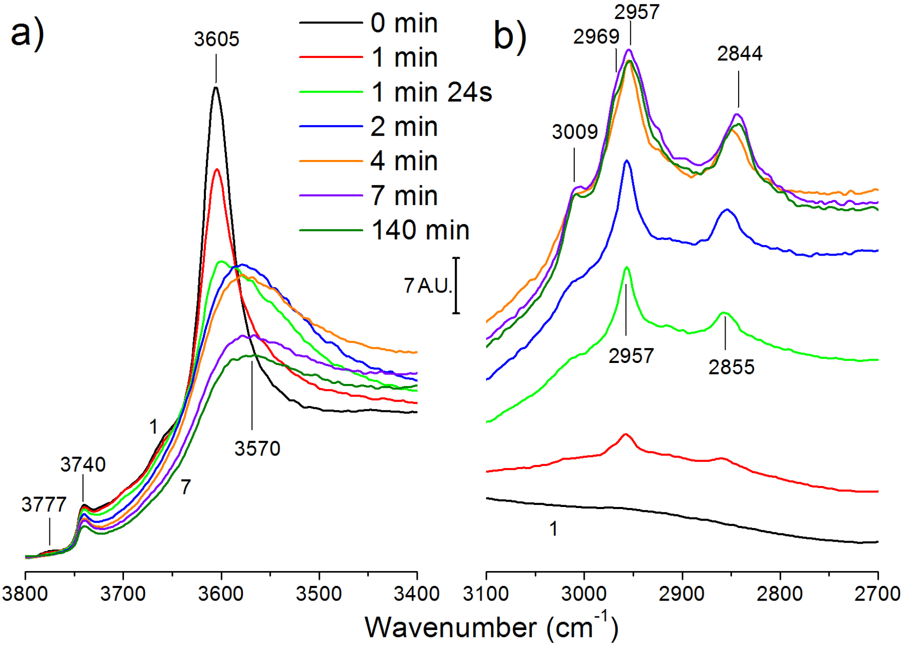

Figure 4.38: Selected DRIFTS spectra of H-ZSM-5 13.5 during MTH-reaction at 200°C. Spectrum 1 before reaction. (a) v(O-H) region; (b) v(C-H) region

development for the two bands does not seem to be consistent. The band is instead assigned to v(O-H) modes of hydrogen bonded methanol.

The reason for the intensity loss for the band at 3578 cm^{-1} could be that methanol is converted to species that does not have v(O-H) modes. There is also a band at 3661 cm^{-1} which is consumed during the reaction, this band is assigned to AlOH groups of extra framework aluminum [87, 88]. The band has a too low intensity to be seen during the screening which was performed with a much poorer resolution.

In region 2 (2700-3100 cm^{-1}), two bands at 2957 and 2855 cm^{-1} and a shoulder at 3009 cm^{-1} immediately appear. These bands have by others in previous experiments been assigned methoxy on silanol groups and to physisorbed methanol [77, 76]. Since this sample holds very few silanols the bands are assigned to physisorbed methanol, this correlates well with the other assignments made.

After 4 minutes three additional bands have grown at 2969, 2946 and 2844 cm^{-1}. These bands have been assigned to dimethyl ether hydrogen bonded to Brønsted sites, which should also have a band at 3011 cm^{-1}[77, 76]. This band could be present within the band at 3009 cm^{-1}.

The band at 2969 cm^{-1} has also been assigned to methoxy on Al OH [77]. This band should be accompanied with a band at 2865 cm^{-1}, which may be present with a low intensity. While our sample holds lite extra framework aluminum, there may be some small amount of methoxy on Al OH present. Dimethyl ether does not have any O-H bonds and this explains the intensity loss for the band at 3578 cm^{-1} in region 1 as methanol is converted.

The presence of a band from v(O-H) modes of methanol and Fermi resonance confirms that methanol forms a neutral adduct at this temperature, the dimethyl ether present on the sample is also assumed to form neutral adducts.

The FID chromatogram from the effluent analysis after 60 min is shown in figure 4.39. The only observed species are methanol and dimethyl ether, indicating no catalytic activity. This is in correlation with what was observed for the IR-spectra, where only methanol and dimethyl ether were present. This also indicates that the methoxy on the AlOH sites have no catalytic activity at this temperature, other studies have shown that they are inactive also at higher temperatures [77]. Water is not observed as it is not detectable by a FID detector [53].

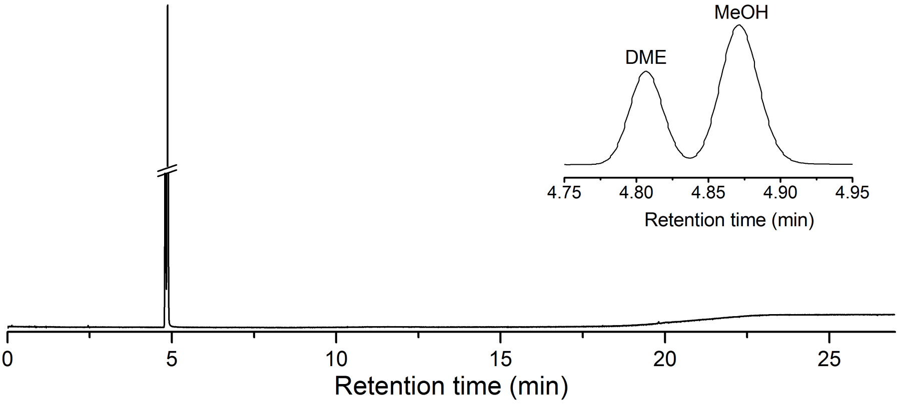

Figure 4.39: FID Chromatogram of the effluents of H-ZSM-5 13.5 during MTH-reaction at 200°C taken after 65 min. The only peaks represent unconverted feed (shown in the inset).

Flushing at 200°C Spectra of the flushing performed after the reaction are shown in figure 4.40. In region 1 the band at 3570 cm^{-1} steadily loses intensity during the first 15 minutes. The silanols shows only a negligible intensity gain, and this is not accompanied with any new changes elsewhere in the spectra. In region 2, the A component of the ABC triplet loses minor intensity, the B component also loses some intensity (not shown).

The bands at 2955 and 2853 cm^{-1}, assigned to methanol, loses a lot of intensity. This intensity loss seems to coincide with that seen in region 1. It therefore seems like some methanol is either converted to dimethyl ether or is flushed out of the system.

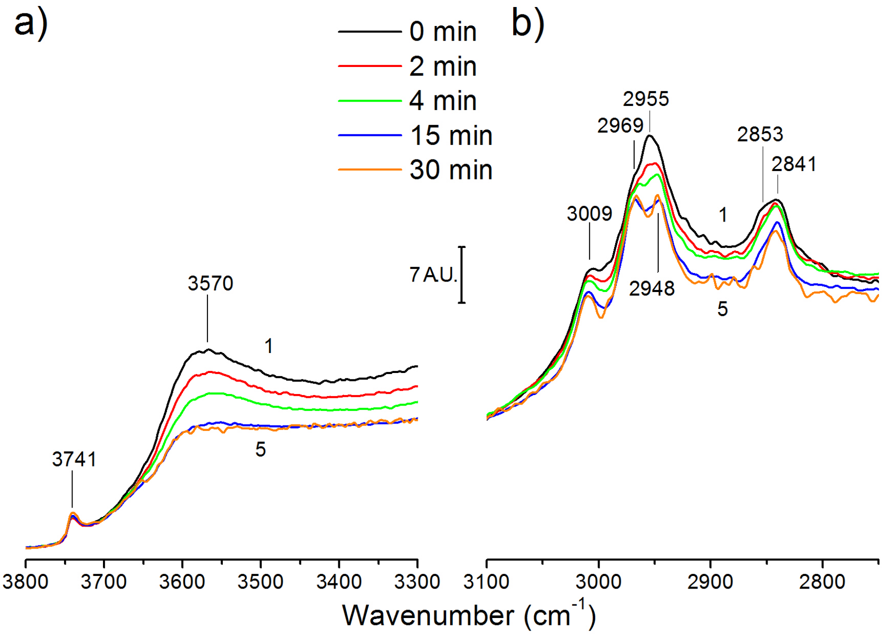

Figure 4.40: Selected DRIFTS spectra of H-ZSM-5 13.5 during flushing following MTH-reaction at 200°C. Spectrum 1 before flushing. (a) v(O-H) region; (b) v(C-H) region

Reaction at 250°C The experiment at 250°C showed no new bands compared to those that at 200°C, selected spectra are shown in figure 4.41. In region 1 the Brønsted band and some of the silanol band are consumed, the band at 3570 cm^{-1} is present but it is much less intense than at 200°C. Different intensities are also seen in region 2.

The bands at 2968, 2946 and 2841 cm^{-1}, assigned to dimethyl ether, shows a much higher intensity than at 200 °C. The bands at 2956 and 2853 cm^{-1}, from methanol, is present at short reaction times, but shows little or no intensity after 140 min.

These results indicate that more dimethyl ether is formed and that methanol possibly desorbs to a larger extent than at 200 °C. FID chromatogram of the effluent analysis (not shown) indicates that the amount of dimethyl ether has increased, and it is more abundant than methanol. There are no other observed species in the effluents.

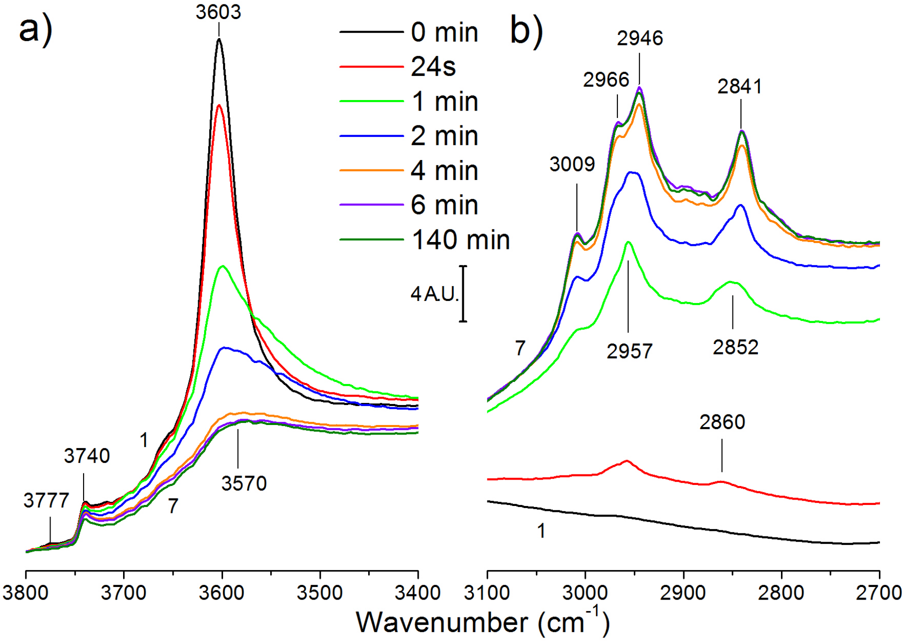

Figure 4.41: Selected DRIFTS spectra of H-ZSM-5 13.5 during MTH-reaction at 250°C. Spectrum 1 before reaction. (a) v(O-H) region; (b) v(C-H) region

Flushing at 250°C The flushing showed a different development than at 200°C, selected spectra are shown in figure 4.42. In region 1 the most apparent change is the partial regeneration of the Brønsted bands. The small broad band at 3575 cm^{-1} loses intensity as it did at 200 °C, and the silanols has a minor intensity gain throughout the flushing. In region 2 the A and B components of the ABC triplet loses much of their intensity throughout the flushing.

After 15 minutes, the bands at 2966, 2945 and 2841 cm^{-1} has lost much of their intensity, and a band at 2972 cm^{-1} becomes visible. The bands at 2972, 2945 and 2841 cm^{-1} were associated with dimethyl ether on the Brønsted sites, but it is not known why some bands lose intensity while others retain their.

Bands from methoxy formed on Brønsted sites are expected at 2978 and 2867 cm^{-1} [77, 89], and a band at 2867 cm^{-1} indeed becomes present after 15 minutes. The band at 2978 cm^{-1} could be hidden in the band at 2972 cm^{-1}, and this would explain the band at 2978 cm^{-1} retains intensity.

While any methoxy seems to be formed simultaneously as bands from dimethyl ether loses intensity, this does not necessary mean that this is the species that forms methoxy as it is in equilibrium with methanol.

Both the regeneration of the Brønsted band and the formation of methoxy correlates well to the intensity loss of the ABC triplet. As methoxy deprotonates the

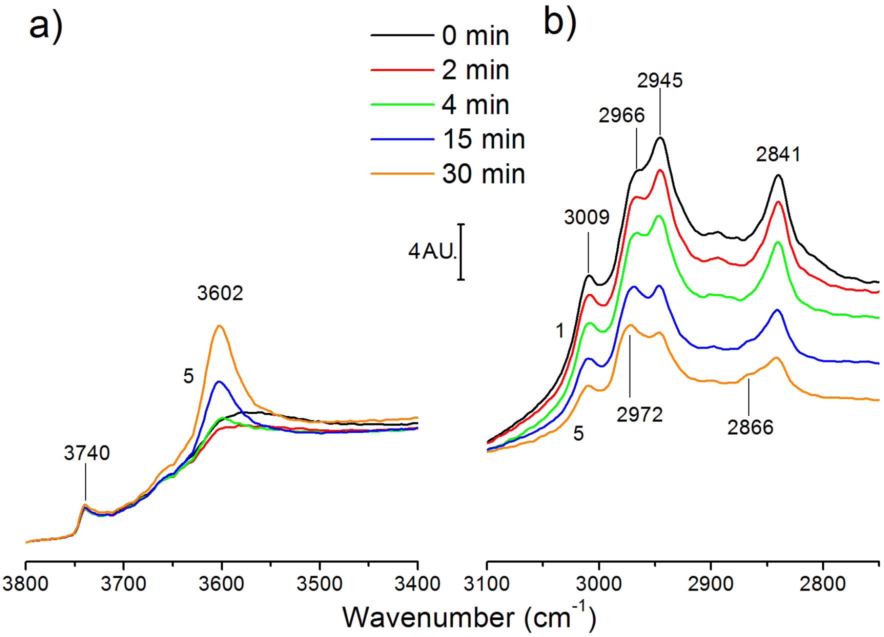

Figure 4.42: Selected DRIFTS spectra of H-ZSM-5 13.5 during flushing following MTH-reaction at 250 °C. Spectrum 1 before flushing. (a) v(O-H) region; (b) v(C-H) region

Brønsted site, the regeneration of the Brønsted band must be caused by methanol and dimethyl ether leaving the system.

The FID chromatogram from the effluent analysis after 30 minutes of flushing is shown in figure 4.43.

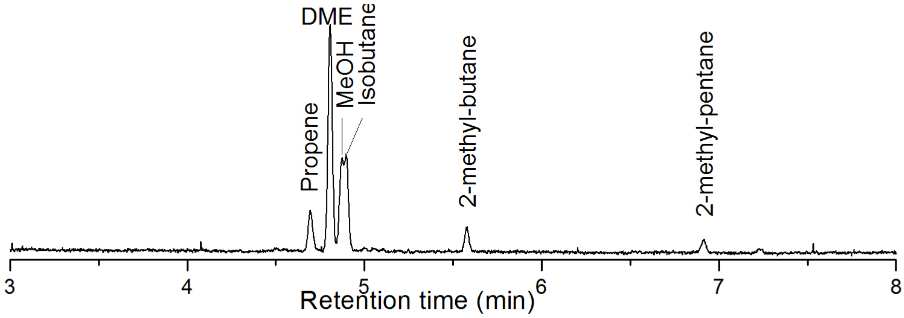

Figure 4.43: FID Chromatogram of the effluents of H-ZSM-5 13.5 after 30 minutes flushing following MTH-reaction at 250 °C for 140 minutes.

As can be seen on the figure, some hydrocarbon species are formed and very little methanol is present, 2-methyl-pentane is the larges hydrocarbon formed. No aromatics are seen in the effluents.

The conversion of some hydrocarbons confirm the presence of methoxy on the sample. As the methoxy is formed after the methanol feed is turned off, it may seem like methoxy is prevented to form if too much methanol is present on the sample.

Reaction at 300°C At 300°C the first actual reaction takes place. DRIFTS spectra are shown in figure 4.44 and 4.45.

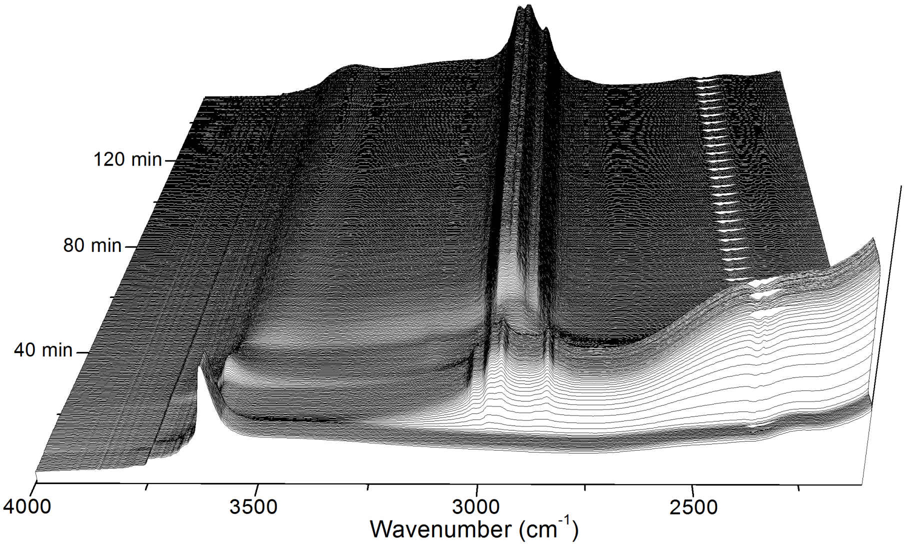

Figure 4.44: DRIFTS spectra of H-ZSM-5 13.5 during MTH-reaction at 300°C.

As can be seen in figure 4.44, the first 6 minutes are not very different compared to the lower temperatures. After this initial period, the intensities of all bands in region 2 and the ABC triplet decreases while the intensity of the Brønsted bands seems to increase.

After approximately 16 min the Brønsted bands again start to decrease and new bands appear in region 2. Figure 4.45 shows the bands in more detail. The spectra recorded after 1 min shows two bands not present during the reaction at the lower temperatures. Both bands, at 2975 and 2866 cm^{-1}, are assigned to methoxy on Brønsted sites. The spectrum recorded after 6 minutes looks similar to those for the lower temperatures, and the two new bands are not distinguishable.

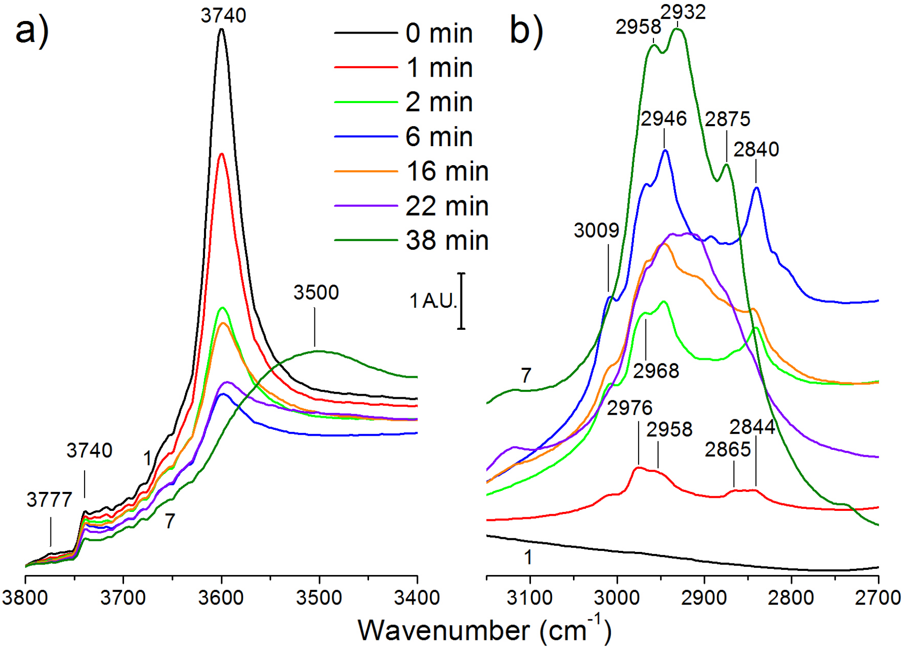

Figure 4.45: Selected DRIFTS spectra of H-ZSM-5 13.5 during MTH-reaction at 300°C. Spectrum 1 before reaction. (a) v(O-H) region; (b) v(C-H) region

The spectra recorded after 38 minutes shows only three bands in region 2, at 2958, 2932 and 2875 cm^{-1}. In region 1, the Brønsted band is fully consumed and a broad band at 3500 cm^{-1} is present. There is also a broad absorption between 3000 and 3500 cm^{-1}. As the sample now catalyzes the MTH reaction, the bands are assumed to arise from various products formed.

Aliphatic and aromatic C-H stretching and bending modes are expected to appear between 2970 and 2850 cm^{-1}, close to the three bands reported in region 2, while many aromatic modes are also expected to appear at wavenumbers above 3000 cm^{-1} [83, 82, 90, 91]. The spectrum does show some intensity above 3000 cm^{-1}, but there are no defined bands. It is therefore assumed that primarily aliphatic gives rise to the bands in region 2, but that aromatics are also present. The broad absorption between 3000 and 3500 cm^{-1} is assigned to Brønsted sites perturbed by the hydrocarbons formed [82, 29].

The result shows that before reaction takes place, an induction period occurs. During this phase, methanol is physisorbed to the zeolite, and is only converted to dimethyl ether and methoxy. Bands from methoxy are only visible the first few minutes, and it is uncertain if they are present for the entire induction period, or if they are a requirement for the reaction phase to start.

Flushing at 300°C The flushing at 300 °C on H-ZSM-5 13.5 shows the least changes of all for the ZSM-5 samples, selected spectra are shown in figure 4.46. In region 1 there is only a small decrease in the intensity of the band at 3497 cm^{-1}, neither the silanol or the Brønsted bands regain any intensity. In region 2 there is a general intensity drop, which is associated with the flushing of the products from the reaction. The small shoulder at 3009 cm^{-1} seems to vanish, indicating that any methanol present desorbs or is converted during the flushing.

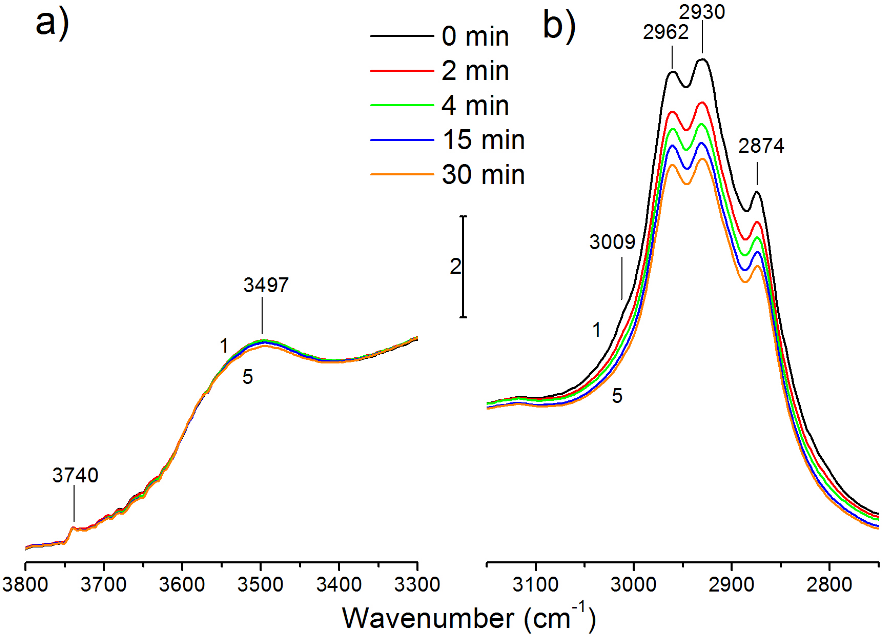

Figure 4.46: Selected DRIFTS spectra of H-ZSM-5 13.5 during flushing following MTH-reaction at 300°C. Spectrum 1 before flushing. (a) v(O-H) region; (b) v(C-H) region

Reaction at 350°C The last experiment for H-ZSM-5 13.5 was conducted at 350°C. Selected IR-spectra are shown in figure 4.47. The first spectra are similar to that obtained at 300 °C after 1 min, with methoxy, methanol and dimethyl ether on Brønsted sites as the dominating bands in region 2. It should be noted that the methoxy bands are more intense at 350 °C than at 300 °C.

The spectrum recorded after 140 min shows some different bands in region 2 than that at 300 °C, there are now intense bands at 2965, 2924 and 2874 cm^{-1} and the continuum from 3000 to 3500 cm^{-1} is more intense. The bands are still assigned to aliphatic and aromatic C-H modes as at 300 °C, but as there is a broad shoulder from 3000 cm^{-1}, more aromatics are most likely present than at 300 °C.

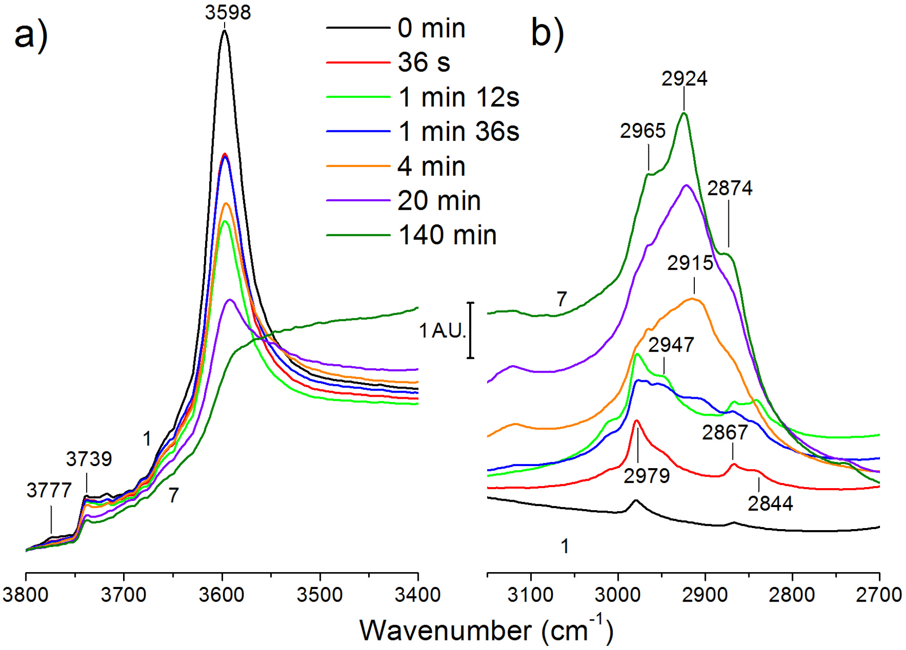

Figure 4.47: Selected DRIFTS spectra of H-ZSM-5 13.5 during MTH-reaction at 350°C. Spectrum 1 before reaction. (a) v(O-H) region; (b) v(C-H) region

Flushing at 350°C The flushing following the reaction is shown in figure 4.48. In region 1, a regeneration of the Brønsted sites can be seen from 15 minutes and on. The Brønsted sites does not fully regenerate, and regains only about 1/4 of its initial height. There is no regeneration of the silanols. In region 2 there is a general loss of intensity for all bands, the relative intensities does not seem to change. This gives an indication of the strength of the hydrogen-bonded adducts formed.

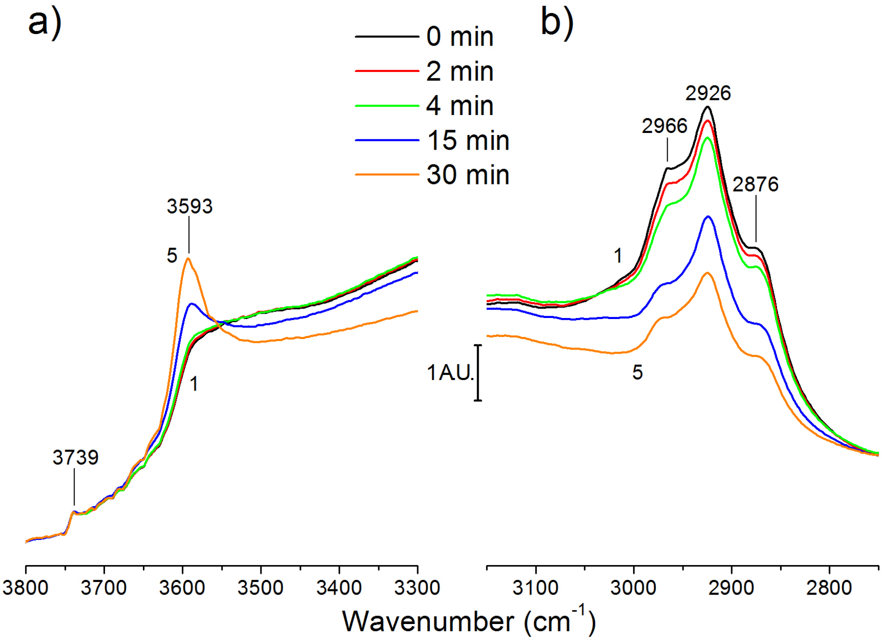

Figure 4.48: Selected DRIFTS spectra of H-ZSM-5 13.5 during flushing following MTH-reaction at 350°C. Spectrum 1 before flushing. (a) v(O-H) region; (b) v(C-H) region

Effluent analysis The catalytic conversion for H-ZSM-5 13.5 is shown in figure 4.49. At 300°C there is no activity after 10 minutes, but after 40 minutes it has risen to 52%. From 65 minutes and onwards the activity drops again, however the IR-spectra does not change during this time.

The reason for this higher conversion is hard to explain, but the analysis it is taken close to the transition between the initial phase and the steady-state. So it might be possible that the initial phase builds up reactive intermediates, which during the early stage of the reaction phase are consumed faster than they regenerate. Over time, the rate of consumption would approaches that of the regeneration, and steady state is obtained.

The conversion at 350 °C is constantly high throughout the experiment.

The effluents from the reactions at 300 and 350 °C show the same species, the effluents at 350 °C contained more of the heavy hydrocarbons. The same species are seen as for the other ZSM-5 samples using the trasmission cell, although the selectivity is slightly different.

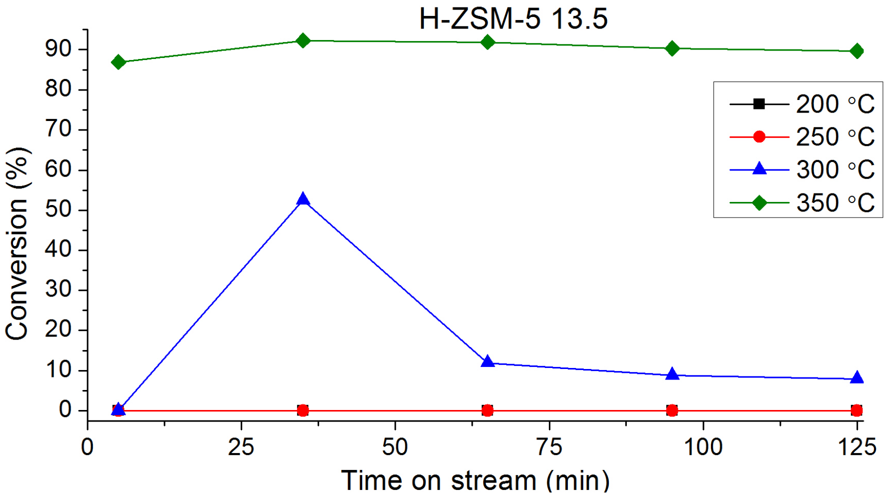

Figure 4.49: Catalytic conversion for H-ZSM-5 13.5 during MTH-reaction at different temperatures

4.3.2.2 H-ZSM-5 15

H-ZSM-5 15 has much of the same features as H-ZSM-5 13.5. It has few/similar defects and a fairly similar Si/Al ratio. The particles are however much smaller, and H-ZSM-5 15 therefore contains silanols to a larger extent. It is expected that, in addition to the bands seen for H-ZSM-5 13.5, new bands will appear from species interacting with silanols.

Reaction at 200°C Selected spectra obtained from the reaction at 200°C using H-ZSM-5 15 are shown in figure 4.50. The spectra are quite similar in region 2 compared to those obtained for H-ZSM-5 13.5 at the same temperature. In region 1, the silanols lose some but not all intensity while the Brønsted band is fully consumed.

The band at 3650 shows a lower intensity than for H-ZSM-5 13.5 at the same temperature, and may indicate that less methanol is present on the sample. In region 2 a new band appears at 2892 cm^{-1}, and the bands at 2950 and 2842 contain low frequency shoulders.

All the new features in region 2 are associated with dimethyl ether hydrogen bonded to silanols [77, 76]. This is expected as H-ZSM-5 15 contains silanols to a larger extent than H-ZSM-5 13.5. After 6 minutes time on stream, the spectra stabilizes and remains unchanged for the rest of the experiment. The effluent analysis showed no catalytic activity.

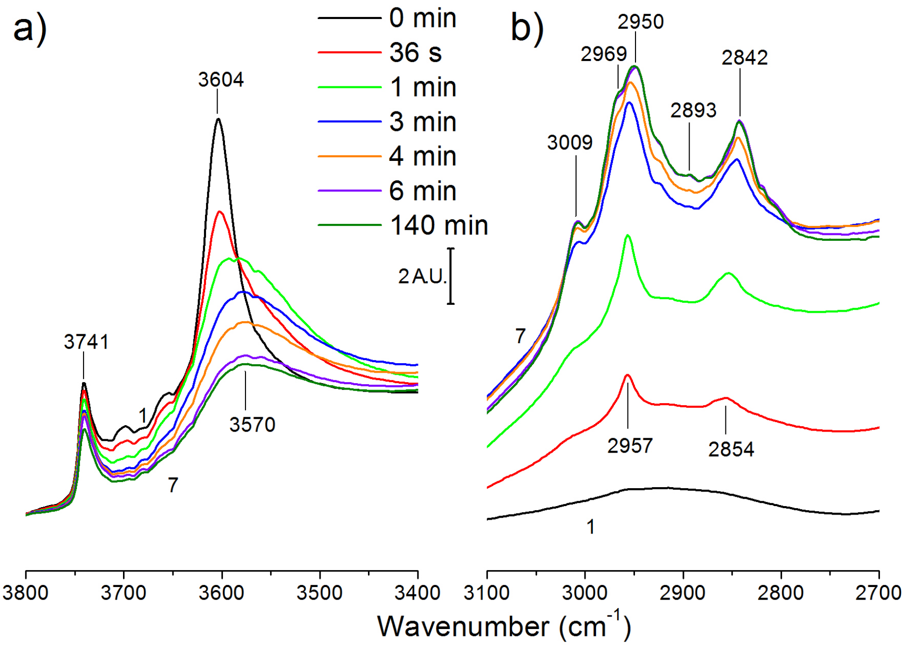

Figure 4.50: Selected DRIFTS spectra of H-ZSM-5 15 during MTH-reaction at 200°C. Spectrum 1 before reaction. (a) v(O-H) region; (b) v(C-H) region

Flushing at 200°C Selected spectra from the flushing is shown in figure 4.51. Region 1 of the flushing at 200°C shows the same loss of intensity for the band at 3570 cm^{-1} as for H-ZSM-5 13.5. The silanol band does not gain intensity, but the Brønsted band does. In region 2, the A component of the ABC triplet loses intensity, this intensity loss is larger than for the previous sample.

The broad band at 2950 cm^{-1} loses intensity, and after 2 minutes only the band at 2946 cm^{-1} remains while the shoulder at 2967 cm^{-1} has become a well defined band. The missing band is that at 2954 cm^{-1}, assigned to methanol on the Brønsted sites.

The band at 3007 cm^{-1} may lose some intensity, but the band at 2853 cm^{-1} does not. If methanol leaves the system, as indicated by the intensity loss of the bands at 3570 and 2954 cm^{-1}, the band at 2853 cm^{-1} must arise from some other species. Methoxy on silanols are expected to have bands around 2959 and 2855 cm^{-1} [77, 76], and is a reasonable assignment as this sample contains silanols.

The band at 2959 cm^{-1} can not be seen on the spectra, but may be hidden by the bands at 2946 and 2967 cm^{-1}. The effluent analysis did not show any other species than methanol and dimethyl ether, the former being much more abundant than the first. This shows that any methoxy formed on the silanols are not reactive at this temperature.

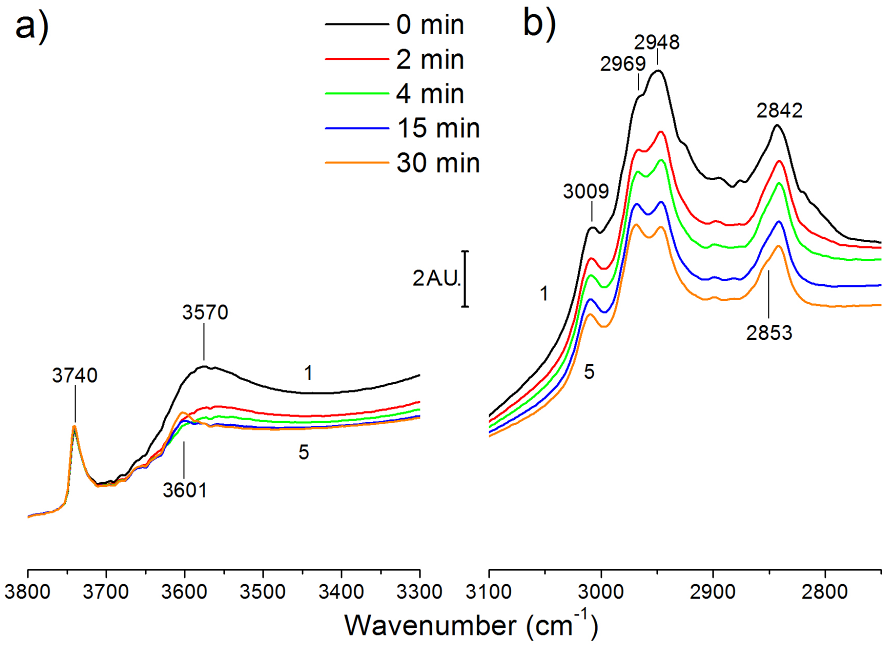

Figure 4.51: Selected DRIFTS spectra of H-ZSM-5 15 during flushing following MTH-reaction at 200°C. Spectrum 1 before flushing. (a) v(O-H) region; (b) v(C-H) region

Reaction at 250°C As for H-ZSM-5 13.5, the reaction at 250°C with H-ZSM-5 15 did not show much differences except from a lesser amount methanol. Selected spectra are shown in figure A.1 in supporting materials. The effluent analysis did not show any catalytic activity.

Flushing 250°C Selected spectra from the flushing is shown in figure 4.52. In region 1 the band at 3570 cm^{-1} loses intensity and a regeneration of the Brønsted sites is visible. The regeneration starts earlier, and the Brønsted band regains more intensity than at 200°C.

This is reasonable as the higher temperature makes diffusion easier. There is only a negligible increase in the intensity of the silanols. In region 2 all the initial bands lose intensity. The bands assigned to dimethyl ether retains some of their intensity, but any band assigned to methanol have a very low intensity.

After 15 minutes of flushing new bands have appeared in region 2 at 2974, 2866 and 2855 cm^{-1}. These bands are assigned to methoxy on Brønsted sites and silanols. Methoxy on silanols should also have a band around 2956 cm^{-1}, and this could be hidden by more intense surrounding bands. It is interesting to note that the shape of the spectra in region 2 after flushing is similar to those during the induction

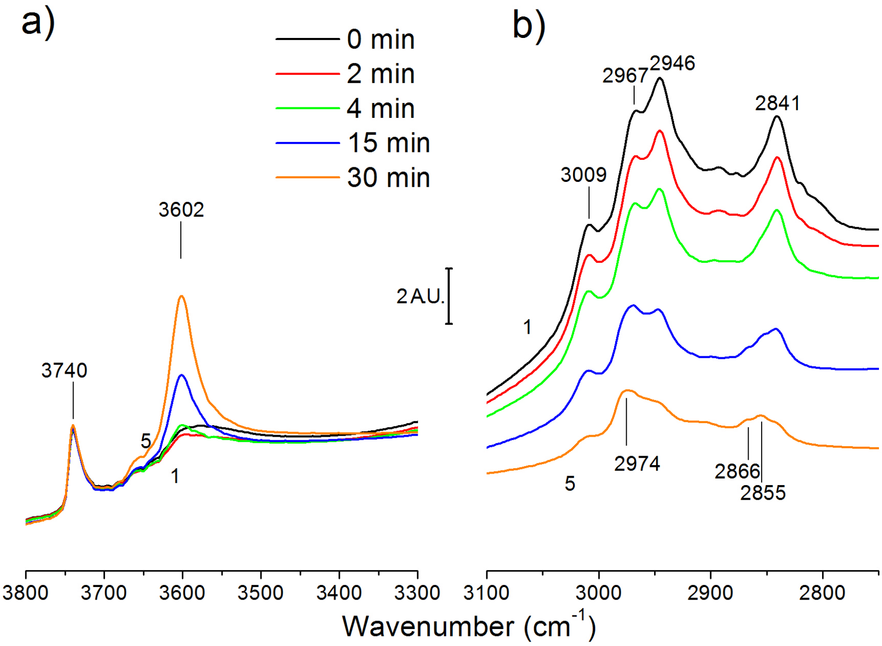

Figure 4.52: Selected DRIFTS spectra of H-ZSM-5 15 during flushing following MTH-reaction at 250°C. Spectrum 1 before flushing. (a) v(O-H) region; (b) v(C-H) region

period at 300°C for both samples, with the exception of the band at 2855 cm^{-1} which is not present for H-ZSM-5 13.5. The effluent analysis shows that propene, isobutan and some higher hydrocarbons are formed, as for H-ZSM-5 13.5.

Reaction at 300°C When reacting at 300°C, some conversion is again seen. Selected spectra are shown in figure 4.53. The induction phase is similar as that for H-ZSM-5 13.5, and the same bands arise in region 2 while the Brønsted bands decrease rapidly. The steady-state phase is however different.

While the bands at 2841 and 3009 cm^{-1} are eroded, the bands at 2967 and 2945 cm^{-1} maintain much of their intensity. There is no continuum from 3000 to 3500 cm^{-1}, and the A and B components of the ABC triplet retain much of their intensity.

This may be either because methanol is still present on the sample, or that the new species formed have some bands at wavenumbers similar to methanol, and interacts with the Brønsted sites through stronger hydrogen-bonds. It is also possible that a combination of both cases happen.

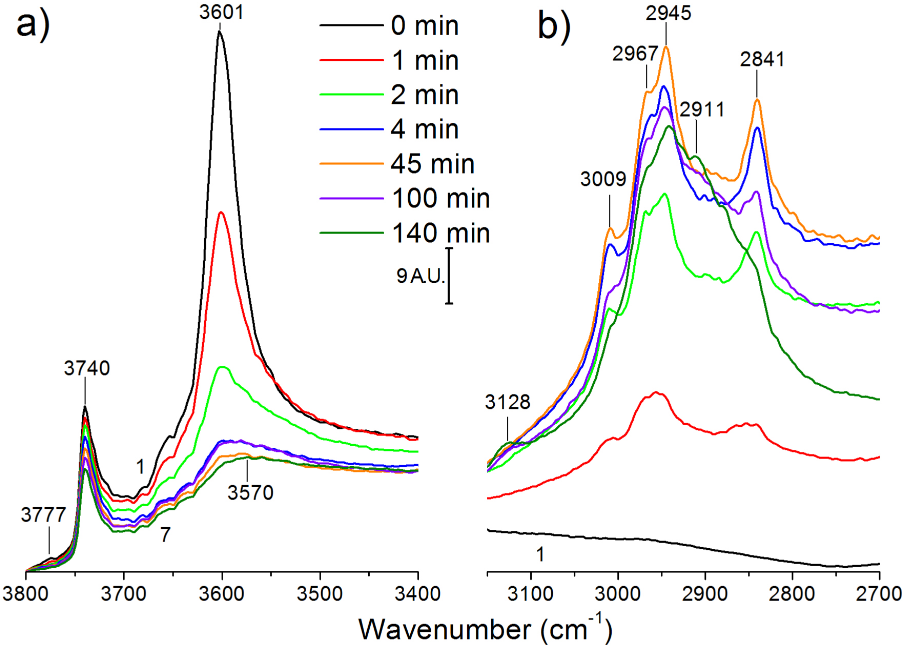

Figure 4.53: Selected DRIFTS spectra of H-ZSM-5 15 during MTH-reaction at 300°C. Spectrum 1 before reaction. (a) v(O-H) region; (b) v(C-H) region

Flushing at 300°C Selected spectra of the flushing are shown in figure 4.54. In region 1 the only change is the partial regeneration of the Brønsted sites, as for the flushing at 250°C. The flushing of H-ZSM-5 13.5 at the same temperature did not regenerate the Brønsted bands. In region 2, the A and B components of the ABC triplet and the bands at 3009, 2853 and 2843 cm^{-1} loses intensity.

There is also a high intensity loss between 2973 and 2940 cm^{-1}. All bands which lose intensity are associated with methanol and dimethyl ether, which must be converted or flushed out of the system. The regeneration if the Brønsted bands correlate well with the intensity loss of the A and B component.

The results show that methanol is most likely present on the sample during the steady-state phase, and is then removed or converted during flushing. But it can not be excluded that other hydrocarbons also form strong hydrogen-bonds with the Brønsted sites.

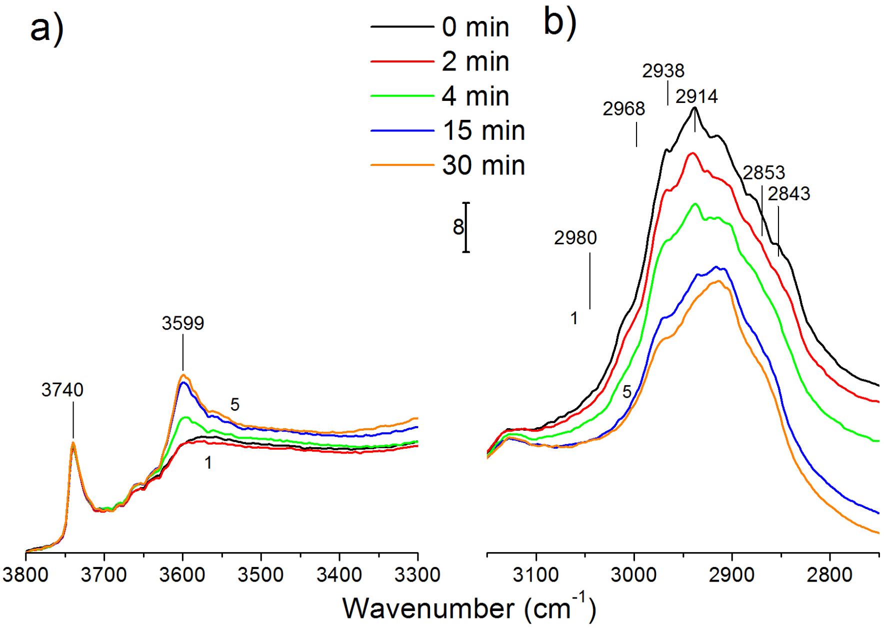

Figure 4.54: Selected DRIFTS spectra of H-ZSM-5 15 during flushing following MTH-reaction at 300°C. Spectrum 1 before flushing. (a) v(O-H) region; (b) v(C-H) region

Reaction at 350°C The last reaction was conducted at 350°C over H-ZSM-5 15, selected spectra are shown in figure 4.55. Again the induction period is similar to that of H-ZSM-5 13.5, with methanol, dimethyl ether and methoxy present immediately after introducing the feed.

During the steady-state phase, region 1 shows that the Brønsted band has lost some, but not all intensity. This was also seen for the screening with the same sample and temperature.

There is not the same continuum between 300 and 3500 cm^{-1} as for H-ZSM-5 13.5. Region 2 shows the same bands as H-ZSM-5 13.5 after 20 minutes, and indicates that much of the same species are formed. It is worth noting that the shape of the spectrum recorded during steady-state is similar to that after flushing at 300 °C.

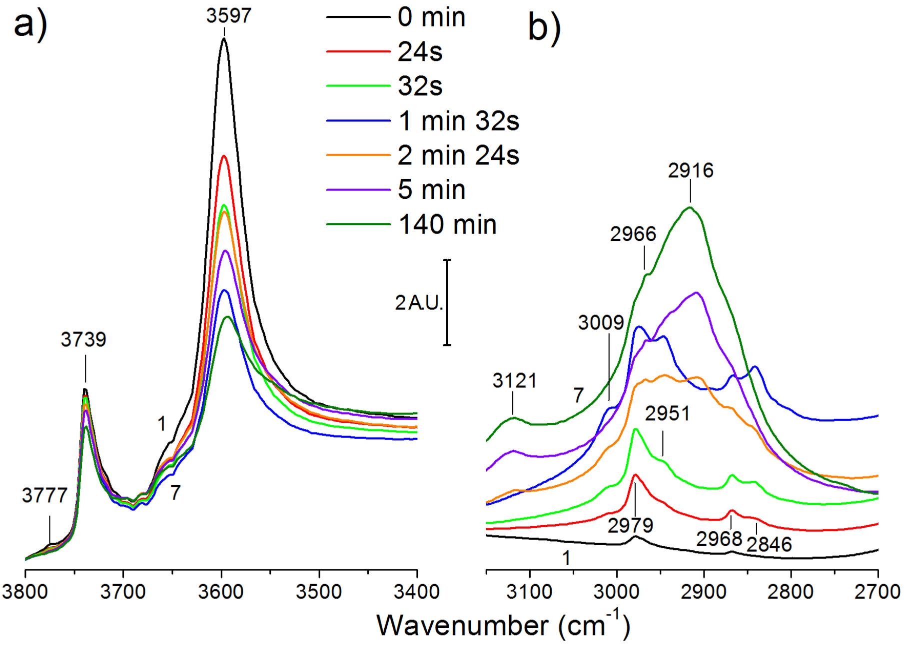

Figure 4.55: Selected DRIFTS spectra of H-ZSM-5 15 during MTH-reaction at 350°C. Spectrum 1 before reaction. (a) v(O-H) region; (b) v(C-H) region

Flushing at 350°C The flushing showed no new bands or features and is presented in supporting materials A.2. The Brønsted bands were regenerated to a larger extent than at 300 °C, and all bands in region 2 lost much intensity at a fairly similar rate. This shows that the hydrocarbons present on the sample is more reactive, or desorbs easier, at 350 than at 300 °C.

Effluent analysis The conversions for H-ZSM-5 15 is shown in figure 4.56. At 300°C the system uses a fairly long time before before some catalytic activity is observed, but then maintains this conversion for the rest for the experiment.

The reason for this development of the conversion may be that this system uses longer time to produce necessary intermediates, which is then the limiting factor during the steady state phase.

The conversion at 350 °C is high throughout the experiment, but starts at a somewhat lower value than for H-ZSM-5 13.5.

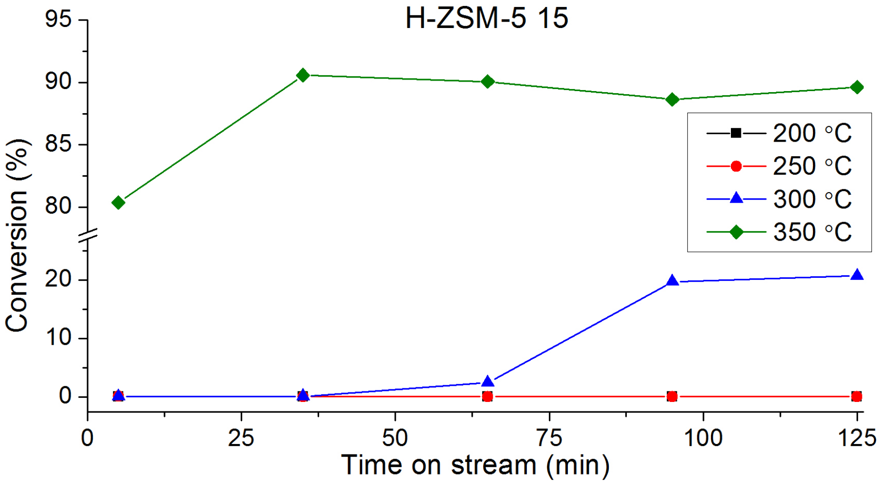

Figure 4.56: Catalytic conversion for H-ZSM-5 15 during MTH-reaction at different temperatures

4.3.2.3 Summary DRIFTS spectra of H-ZSM-5 13.5 and 15

The DRIFTS spectra for the two samples shows that methanol physisorbs and is to some extent converted to dimethyl ether at 200 and 250 °C. The flushing at 250 °C showed some conversion, and it seems that the formation of both methoxy and hydrocarbons is prevented if too much methanol is present. At the lower temperatures the only difference between the two samples is that H-ZSM-5 15 contains bands from dimethyl ether in addition to the bands seen for H-ZSM-5 13.5.

The results further show that 300 °C or more is required to catalyze the MTH reaction while feeding methanol. Prior to conversion an induction period occurs, where methanol and dimethyl ether physisorbs to the sample and some methoxy is formed. The induction period is shorter at 350 than at 300 °C. During the steady-state reaction at 300 °C, H-ZSM-5 15 still contains methanol and the spectra are therefore different from those of H-ZSM-5 13.5 at the same temperature.

At 350 °C, the two samples show much of the same bands in region 2, except from the continuum between 3000 and 3500 cm^{-1} which is much more intense for H-ZSM-5 13.5. This could indicate that this sample produces more aromatic hydrocarbons than H-ZSM-5 15.

4.3.2.4 Effluent analysis

The FID chromatograms for H-ZSM-5 13.5 and 15 at 350°C after 65 minutes on stream are shown in figure 4.57.

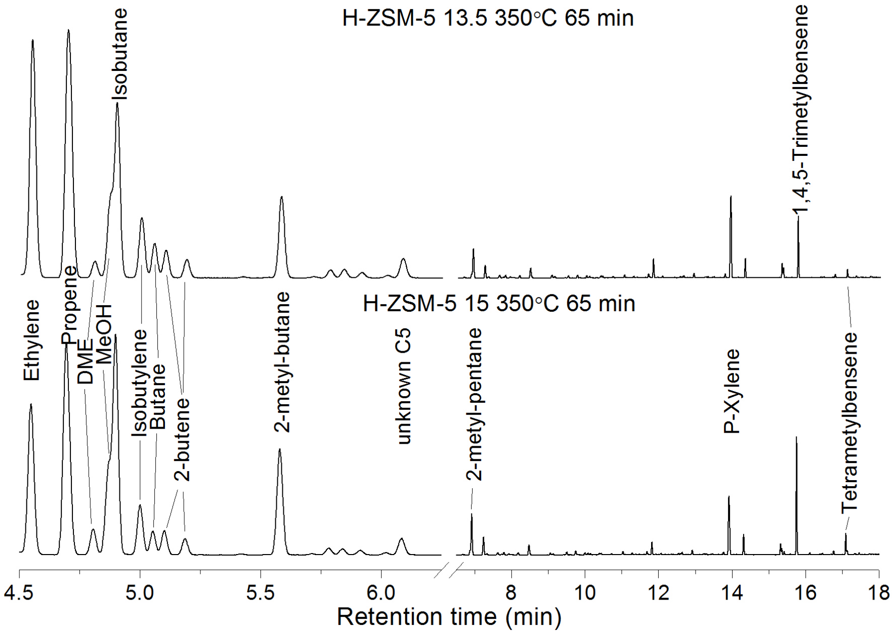

Figure 4.57: FID chromatogram of effluents from H-ZSM-5 13.5 and 15 during MTH-reaction at 350°C. The effluents are collected after 65 min.

As can be seen, the two samples produce the same species with fairly similar intensities. The main difference is that H-ZSM-5 13.5 has a tendency to produce more linear molecules than H-ZSM-5 15. The similar selectivity for the two samples seems reasonable as they have the same topology and a similar Si/Al. Although the results does not indicate that H-ZSM-5 12.5 yields more aromatics, they are otherwise consistent with the IR-spectra at steady-state for the two samples at this temperature.

4.3.3 DRIFTS spectroscopic investigation of silicalite sample

The MTH reaction was also performed on the silicalite sample using the DRIFTS cell. This was done to study a sample that is similar to H-ZSM-5 15 with the exception of the absence of Brønsted acidic sites. Any bands present for H-ZSM-5 15 that are not seen for the silicalite sample are assumed to arise from species interacting with, or formed on, Brønsted acidic sites.

4.3.3.1 DRIFTS spectrum of dehydrated silicalite

DRIFTS spectra showing the v(O-H) region of the calcined silicalite sample is shown in figure 4.58. The sample has two bands dominating the region which is assigned based on previous studies. The fairly sharp band at 3731 cm^{-1} represents isolated Si-OH groups on the external surface not interacting with other species to any significant extent [92, 40]. The band might consist of other components, for instance one at 3713 cm^{-1}, but they are overshadowed by the very intense band, so no certain assignment can be made.

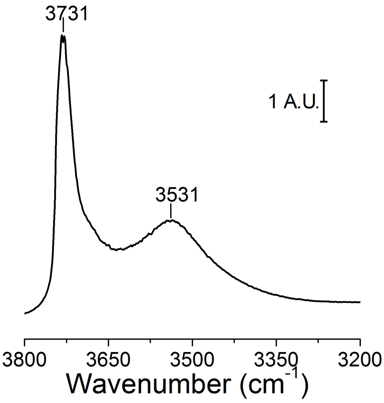

Figure 4.58: DRIFTS spectra showing the v(O-H) region of the calcined silicalite recorded at 300°C

The low frequency band with a maximum at 3531 cm^{-1} is hydroxyls mutually interacting via medium strength hydrogen bonds, IE. silanol nests [40]. The silanol nests are cured when calcined at temperatures around 500 °C and forms strained Si-O-Si bridges. These bridges are reported to be reactive and could make the spectra of the reaction more complex [40].

4.3.3.2 DRIFTS of silicalite during water desorption

The sample was calcined prior to all reactions. DRIFTS spectra of the desorption of water from the silicalite is shown in figure 4.59. At higher water loadings the spectra only shows four bands. The bands at 3742 cm^{-1} is assigned to silanols

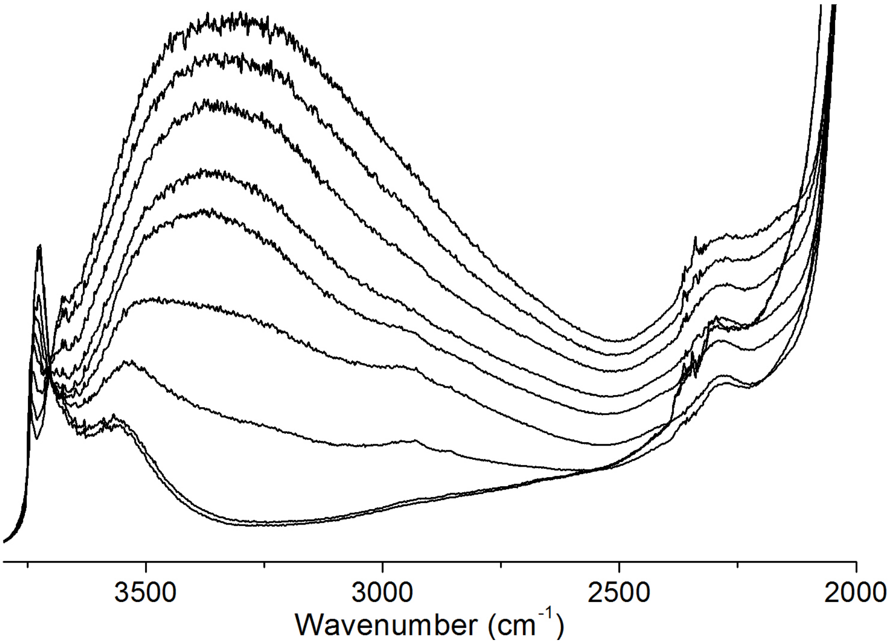

Figure 4.59: DRIFTS spectra showing the desorption of water from the silicalite sample.

not affected by the water, while the band at 3671 cm^{-1} is assigned to unperturbed stretch modes of water. As for the other samples, the broad continuum from 2600 to 3600 cm^{-1} is assigned to various modes from water. The band at ca 2314 cm^{-1} is assigned to carbon dioxide.

As the temperature increases, the bands assigned to water loses intensity while the bands assigned to silanols gain intensity. The silicalite has no Brønsted acidic sites, so there is no presence of Fermi resonance.

At lower water loadings, two bands assigned to hydrocarbons become visible at 2929 and 2856 cm^{-1}, and eventually a band at 3535 cm^{-1} also appears. This band, assigned to silanol nests, steadily loses intensity and shift to higher wavenumbers as the temperature increases.

The band continues to lose intensity while the sample is kept at 450°C, and loses even more intensity for the calcinations at 500°C. This is because the silanol nests are converted to isolated silanols and strained Si-O-Si bridges.

4.3.3.3 DRIFTS of silicalite during methanol feeding

Reaction at 200 °C DRIFTS spectra of the silicalite during reaction at 200 °C are shown in figure 4.60. Unlike for the reactions at higher temperatures, the

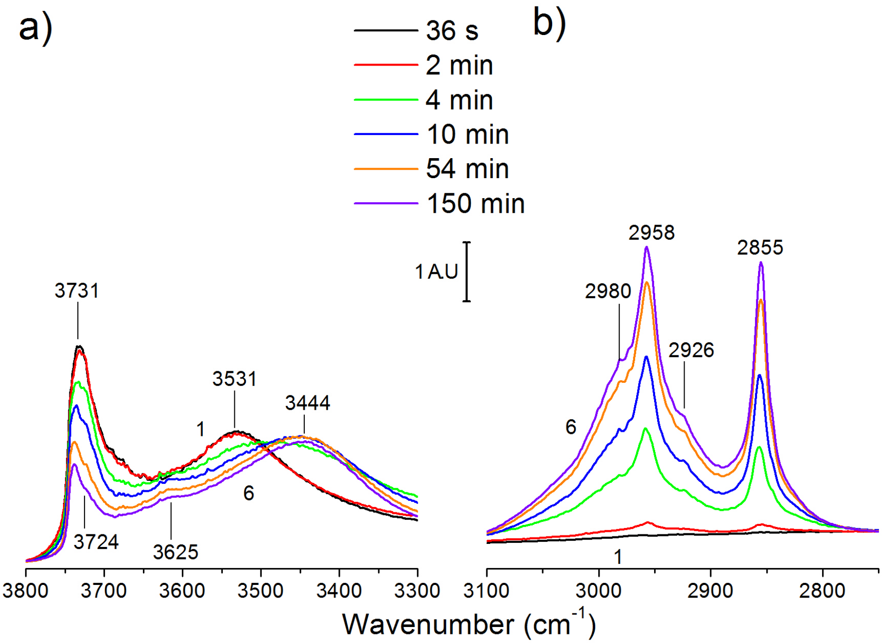

Figure 4.60: Selected DRIFTS spectra of the silicalite during MTH reaction at 200°C. Spectrum 1 before reaction. (a) v(O-H) region; (b) v(C-H) region.

sample used for the reaction at 200 °C was only calcined at 450 °C. The silanol nests therefore have a higher intensity than for the other reactions and the silanols are less intense. In the v(O-H) region, consumption of both initial bands can be observed, while a new broad band appears at 3444 cm^{-1} and a small shoulder at 3625 cm^{-1} also becomes visible.

The consumption of the band at 3731 cm^{-1} seems to coincide with the growth of the new bands in the v(C-H) region and possibly with the band at 3444 cm^{-1}. The band could appear from silanols perturbed by methanol, with a red shift of $\Delta v\,(OH) = -280\,\mathrm{cm}^{-1}$. If this is the case, bands from hydrogen bonded methanol would be expected in the v(C-H) region.

As the intensity of the dominant band at 3731 cm^{-1} decreases, a shoulder at 3724 cm^{-1} becomes apparent. This shoulder is assigned to silanols in the internal surface [93]. The loss of intensity for the band at 3531 cm^{-1} seems to occur at a similar rate as the growth of the band at 3444 cm^{-1}, and could indicate that the new band is from silanol nests interacting with methanol.

The small shoulder at 3625 cm^{-1} is visible as soon as the silanol bands start to decrease and is assigned to nearly free v(O-H) modes from methanol.

In region 2, two intense bands appear at 2855 and 2958 cm^{-1} with two shoulders at 2926 and 2980 cm^{-1}. The bands at 2855 cm^{-1} and 2958 cm^{-1} have by others in previous experiments been assigned to both methoxy on silanol sites ($SiOCH_3$), and to hydrogen-bonded methanol.

Both species are expected, but hydrogen-bonded methanol should also have a band at 3007 or 2993 cm^{-1} and there are no clear shoulders around those wavenumbers. In addition, the band from v(O-H) modes of methanol shows a very low intensity. Therefore the bands at 2855 and 2958 cm^{-1} are assigned to methoxy formed on silanol sites, and any hydrogen-bonded methanol is present a small extent.

Since the two bands are assigned to methoxy on deprotonated silanols and not hydrogen bonded methanol, it is therefore more likely that the band at 3444 cm^{-1} appears from silanol nests with methanol. It is expected that methanol interacting with the silanol nests also shows bands in region 2.

The shoulder at 2926 cm^{-1}is present for both H-ZSM-5 samples at the same temperature, but it is then much less intense compared to the other bands. Both shoulders at 2926 and 2980 cm^{-1} have been assigned to dimethyl ether physisorbed to the external surface [76].

The results show that some methanol is physisorbed to the sample, but most forms methoxy on the silanols or interacts with the silanol nests is some manner.

Flushing at 200 °C Figure 4.61 shows the DRIFTS spectra of the flushing subsequent to the reaction. In region 1, the only change is the consumption of the band at 3625 cm^{-1}. This gives an indication of the strength of the interacting between the adsorbed species and the silanols and silanol nests.

In region 2, all bands lose some intensity, with band at 2855 cm^{-1} losing less than the other bands. The loss of intensity for the bands at 2855 and 2958 cm^{-1} could be attributed to the out gassing of the weakest bound methoxy formed on the silanol sites, but this should be followed by an increased intensity for the silanol bands which is not present.

Loss of methoxy should also be detected in the effluent analysis as carbon species other than oxygenates. The intensity loss of the bands at 3625, 2855 and 2958 cm^{-1} is attributed to the desorption of the physisorbed methanol present. The intensity loss for the shoulders at 2926 and 2980 cm^{-1}shows that the dimethyl ether is not strongly bound to the external surface.

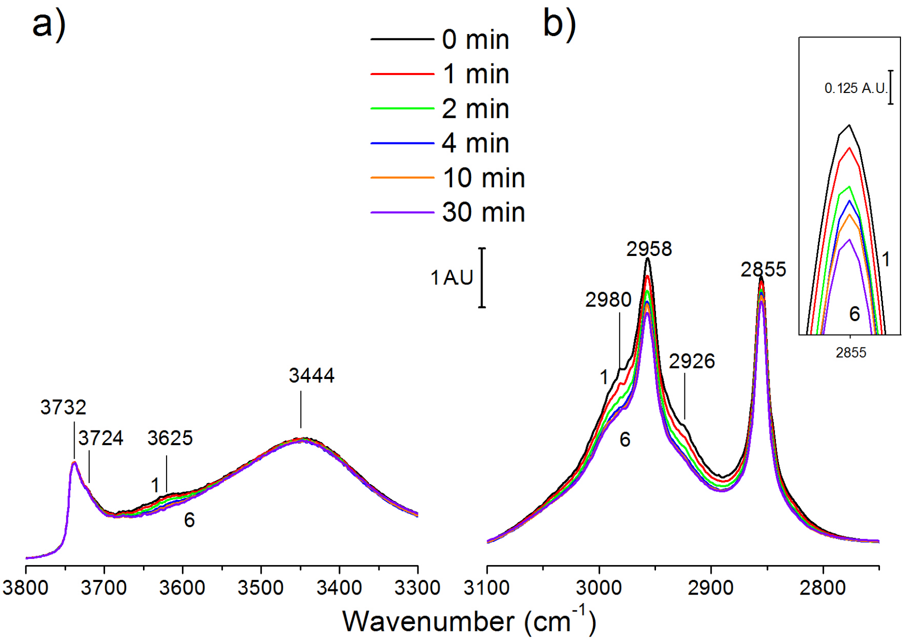

Figure 4.61: Selected DRIFTS spectra of the silicalite during flushing at 200 °C after reaction. Spectrum 1 before flushing. (a) v(O-H) region; (b) v(C-H) region. The inset shows a magnification of the band at 2855 cm^{-1}.

Reaction and flushing at 250 and 300 °C DRIFTS spectra from the same reaction and following flushing carried out at 250 and 300°C are shown in figure 4.62,4.63,4.64 and 4.65. The spectra does not show any new bands or other new features compared to the spectra recorded at 200°C, except from a shift of the bands at 3531 cm^{-1} and 3444 cm^{-1} to higher wavenumber. These bands were assigned to silanol nests interacting with themselves and methanol respectively, and the similar shift supports this assignment.

The silanols lose more intensity at higher temperatures and the bands in region 2 seems to gain a higher intensity, although the higher intensity in region 2 must not be relied on too much because the DRIFTS cell used is not quantitative. The band at 3625 cm^{-1} is shifted to 3519 cm^{-1}, shows less intensity at the higher temperatures, and is barely present at 300 °C. The bands in region 2 does not show the same lower intensity for higher temperatures.

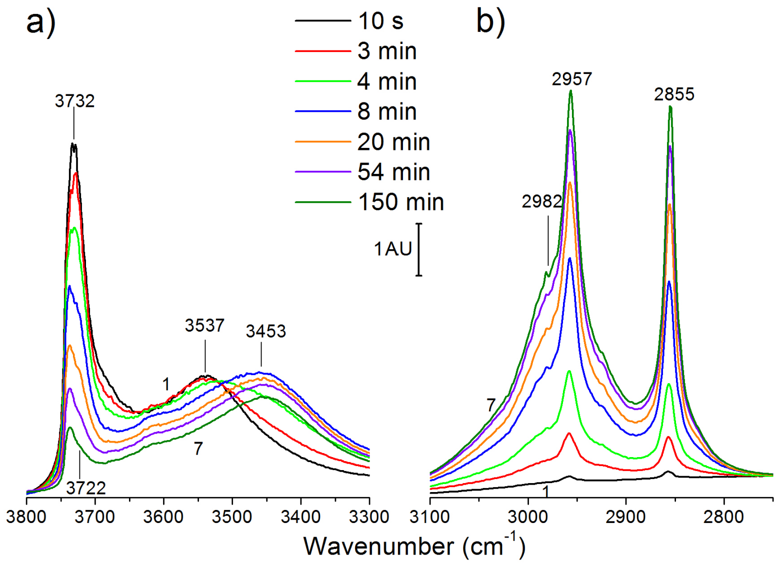

Figure 4.62: Selected DRIFTS spectra of the silicalite during MTH reaction at 250°C. Spectrum 1 before reaction. (a) v(O-H) region; (b) v(C-H) region

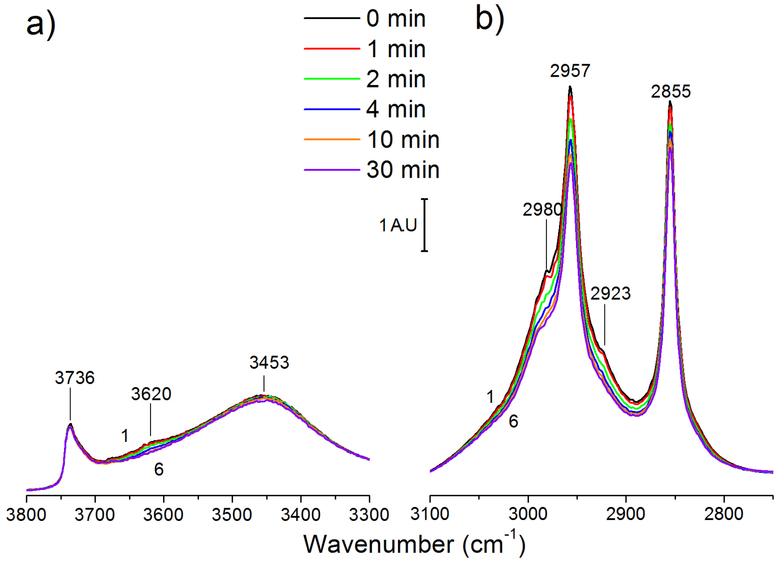

Figure 4.63: Selected DRIFTS spectra of the silicalite during flushing at 250 °C after reaction. Spectrum 1 before flushing. (a) v(O-H) region; (b) v(C-H) region.

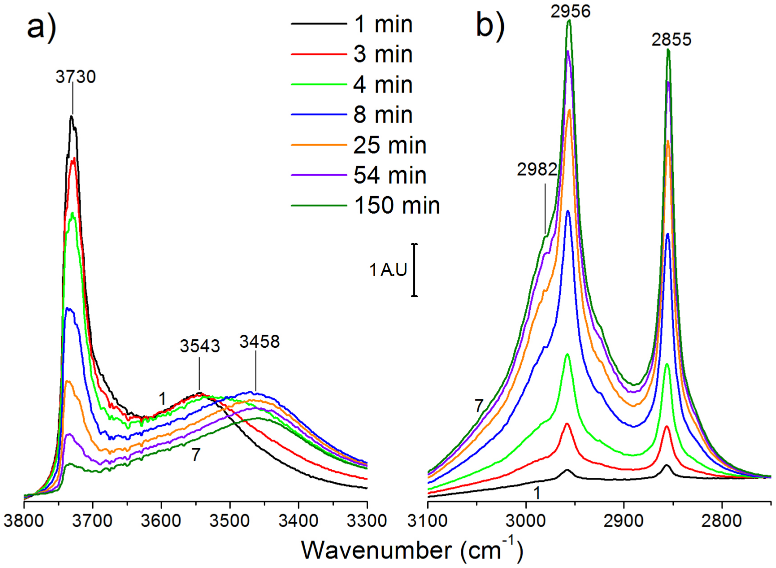

Figure 4.64: Selected DRIFTS spectra of the silicalite during MTH reaction at 300°C. Spectrum 1 before reaction. (a) v(O-H) region; (b) v(C-H) region.

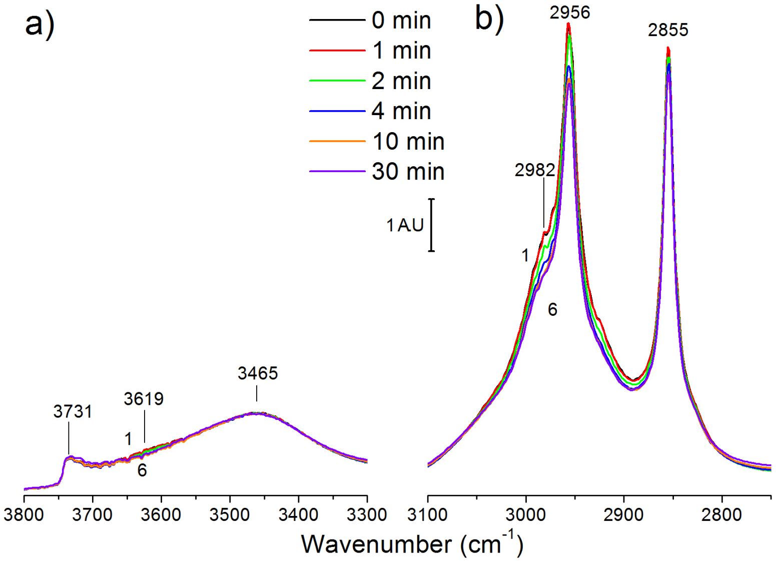

Figure 4.65: Selected DRIFTS spectra of the silicalite during flushing at 300 °C after reaction. Spectrum 1 before flushing. (a) v(O-H) region; (b) v(C-H) region.

Reaction at 350 °C DRIFTS spectra of the reaction at 350 °C are shown in figure 4.66. Here the consumption of the silanol bands is even more pronounced than for the lower temperatures, and the band seems to lose almost all intensity. The development of the two bands at 3464 and 3549 cm^{-1} is not very different than at the lower temperatures.

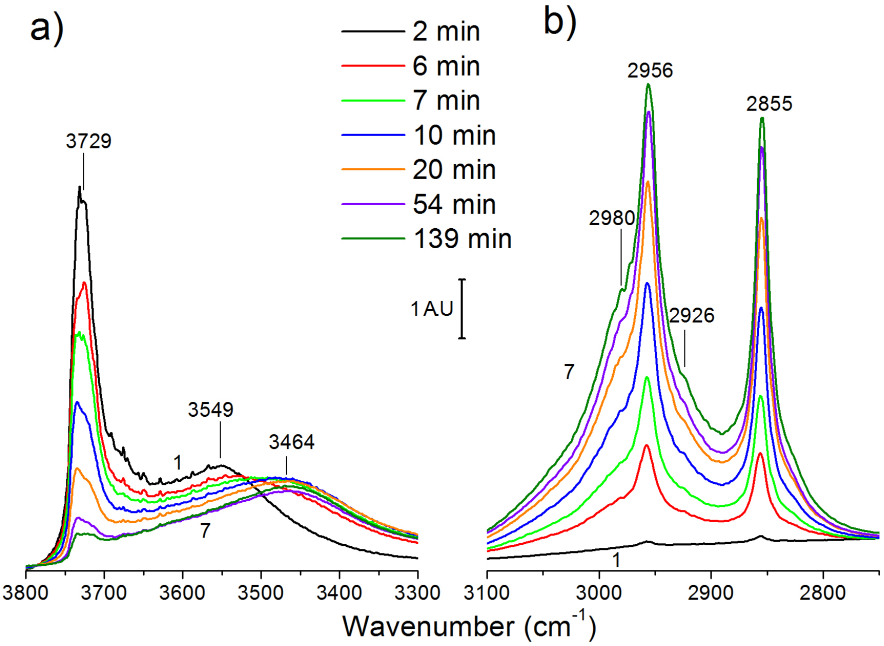

Figure 4.66: Selected DRIFTS spectra of the silicalite during MTH reaction at 350 °C. Spectrum 1 before reaction. (a) v(O-H) region; (b) v(C-H) region

The shoulder at 3617 cm^{-1} seen for the previous temperatures is not visible. In region 2, the same bands are present as for the other temperatures. The only change is the previously mentioned higher intensity for the bands at 2855 and 2956 cm^{-1} which correlates to the larger intensity loss of the silanol bands.

Flushing at 350 °C DRIFTS spectra of the flushing are shown in figure 4.67. In region 1, the only change during the flushing is a minor regeneration of the band at 3713 cm^{-1}, which was assigned to internal silanols. The intensity gain could result from the higher temperature during flushing, making some desorption possible. It could also result from the lower initial intensity.

The development is not much different in region 2 than for the lower temperatures. Which species that leave the silanols during regeneration is uncertain as there is no pronounced change in region 2 between the two spectra recorded after 10 and 30 minutes on stream.

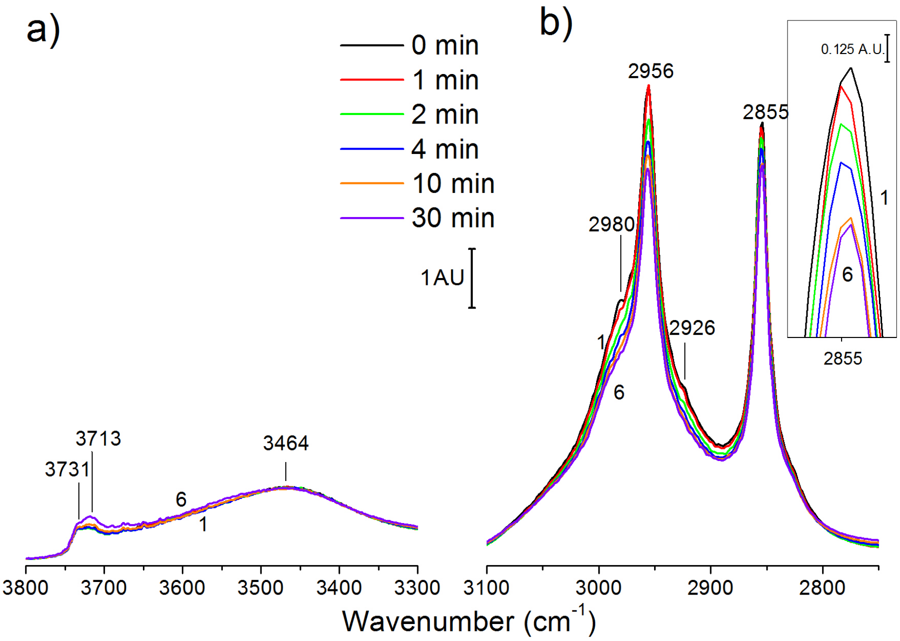

Figure 4.67: Selected DRIFTS spectra of the silicalite during flushing at 350 °C after reaction. Spectrum 1 before flushing. (a) v(O-H) region; (b) v(C-H) region.

4.3.3.4 Summary DRIFTS spectra of silicalite

The spectra of the silicalite sample during methanol feeding shows that the sample does not catalyze the MTH reaction as the acidic zeolites did. The silanols primarily interacted with a species assumed to be methoxy, and physisorbed methanol was only present to a small extent. Some dimethyl ether was also formed which did not interact much with the silanols.

4.3.3.5 Effluent analysis during reaction

FID chromatograms of the effluents from the reaction at 200 and 350 °C, collected after 70 min are shown in figure 4.68 and 4.69. There were no conversion of methanol below 300 °C, not even to dimethyl ether. This undermines the assignment of the shoulders at 2926 and 2980 cm^{-1}to dimethyl ether, as these bands lost intensity during the flushing and should be detected in the effluents.

But as the analysis is of the effluents after 30 minutes, it may be that all the dimethyl ether is removed during the first few minutes of the flushing, as indicated by the IR-spectra. At 300 °C (not shown), a very small peak from dimethyl ether can be seen.

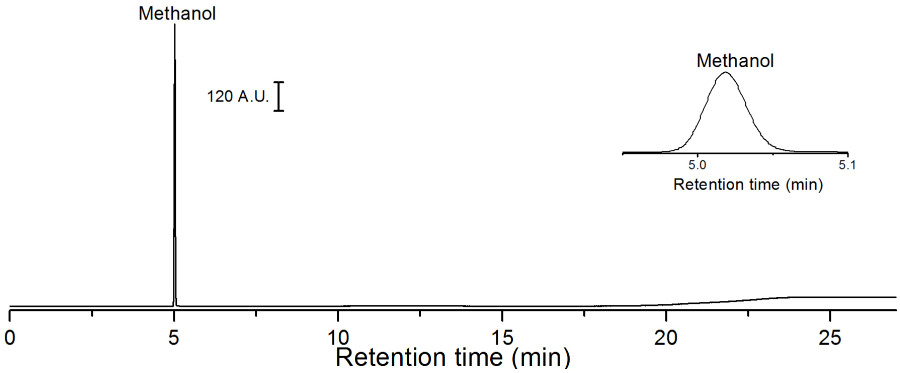

Figure 4.68: FID chromatogram of the effluents of the silicalite sample during MTH at 200 °C taken after 70 min. The only peak represent uncoverted methanol (shown in instet).

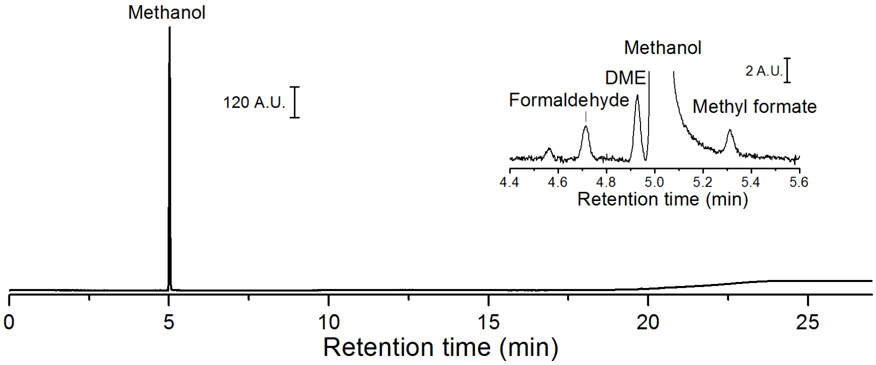

Figure 4.69: FID chromatogram of the effluents of the silicalite sample during MTH at 350 °C taken after 70 min. The inset shows the minor species present.

At 350 °C the oxygenates formaldehyde, dimethyl ether and methyl formate is present in very small amounts. These species are most likely formed in gas phase reactions. This is in accordance with the assumption that brønsted acidity is required to catalyze the MTH reaction. The absence of species other than methanol confirms the assignments of methanol or methoxy in region 2 of the IR spectra, but also undermines the assignment of bands in the IR-spectra to dimethyl ether.

Chapter 5

Conclusions

The samples were all of the assumed topology, and showed a variety in Si/Al ratio, particle size and defects.

All the zeolites were investigated by transmission FTIR spectroscopy during water desorption and MTH reaction. With the exception of H-Beta 12.5 2, all zeolites were characterized by a Brønsted band around 3600 cm^{-1}, the Y-zeolites contained two families of Brønsted sites. All the zeolites yielded products during the reaction, even H-Beta 12.5 2 which showed no Brønsted acidity. In the The v(C-C) region, the spectra varied for the ZSM-5 samples, while H-Beta 12.5 and H-Beta 19 were similar. Also the Y zeolites were similar to each other.

The ZSM-5 samples showed bands from both aromatics and oligomers in region 3, while the Beta zeolites showed primarily bands from aromatics. The Y zeolites showed bands from both aromatics and alkenes. H-MOR was most likely deactivated during the reaction. The samples did not show any clear trends in the effluent analysis, with the exception of the ZSM-5 samples not yielding species larger than tetramethylbenzene.

The contradictory results for H-Beta 12.5 2 may be caused by species adsorbed on the sample which deprotonates the Brønsted bands, but still allows some conversion to occur during the MTH reaction.

The DRIFTS experiments gave more detailed information about the samples during reaction. At 200 and 250 °C the methanol physisorbed to the sample, and was only converted to dimethyl ether. The flushing at 250 °C showed new bands from methoxy on the Brønsted sites, and produced hydrocarbons were detected in the effluents. The samples still showed bands from methoxy on Brønsted sites after 30 min of flushing. H-ZSM-5 15 still contained methanol during the reaction at 300 °C, while this was not seen for H-ZSM-5 13.5.

This was also confirmed by the effluent analysis, which showed a much lower conversion for H-ZSM-5 15 at 300 °C. The higher presence of methanol may explain why only the Brønsted sites of H-ZSM-5 15 were partially restored during the flushing at 300 °C The two ZSM-5 samples did not show much difference at 350°C.

The silicalite sample did not show any conversion at any of the temperatures, which was expected as the sample does not contain Brønsted acidic sites. The most abundant species on for all the temperates appeared to be methoxy, which did not leave during the flushing. Some methanol physisorbed to the sample, but desorbed during flushing. The IR-spectra indicated the formation of some dimethyl ether which were removed during the flushing, but this was not seen in the effluent analysis taken after 30 minutes of flushing.

The silanol bands of H-ZSM-5 13.5, H-ZSM-5 15 and the silicalite sample all behaved in a similar manner, and indicates that methoxy forms on all silanols and that this methoxy is unreactive.

Chapter 6

Further Work

In order to determine whether H-Beta 12.5 2 contains any adsorbed species, the sample should be calcined again for a longer period of time, and at a higher temperature. The sample should also be investigated by FTIR using pyridine as a probe molecule to determine if the sample is acidic.

A continuation of the DRIFTS experiments performed on the ZSM-5 samples could be to investigate methoxy on the Brønsted sites of the samples. The methoxy could be formed by e.g. feeding methanol at 250 °C for one hour and flushing for three. The reactivity of methoxy at lower temperatures could be investigated by feeding methanol at 200 and 250 °C.

It should also be investigated whether the methoxy formed at 250 °C reacts at higher temperatures by simply heating a sample with methoxy to 300 or 350 °C. Another investigation could be the interaction between a sample with adsorbed methoxy and hydrocarbon pool species at lower temperatures, or other more conventional probe molecules.

By performing these experiments on ZSM-5 samples similar to those used in the DRIFTS part of this thesis, the incluence of methoxy on silanols could also be investigated.

Similar types of experiments could be performed on the silicalite sample to provide a comparison with a sample that has only methoxy formed on silanols. The reactivity of methoxy formed on silanols should be looked into by heating a silicalite sample with methoxy to higher temperatures and see whether it desorbs.

Bibliography

[1] Jacobsen CJH, Dohrup J, Schmidt I. Katalyse - Introduktion til Kemien Bag Katalytiske Processer. Lyngby: Haldor Topsøe; 1999.

[2] Chorkendorff I, Niemantsverdriet JW. Concepts of Modern Catalysis and Kinetics. Weinheim: Wiley-WCH; 2003.

[3] Dyer A. An Introduction to Zeolite Molecular Sieves. John Wiley & Sons Ltd.; 1988.

[4] Szostak R. Molecular Sieves Principles of Synthesis and Identification. New York: Van Nostrand Reinhold; 1989.

[5] van Bekkum H, Flanigen EM, Jacobs PA, Jansen JC. Introduction to Zeolite Science and Practice. 2nd ed. Amsterdam: Elsevier Sicience B.V.; 2001.

[6] Bjørgen M, Svelle S, Joensen F, Nerlov J, Kolboe S, Bonino F, et al. Conversion of methanol to hydrocarbons over zeolite H-ZSM-5: On the origin of the olefinic species. Journal of Catalysis. 2007;249:195–207.

[7] Chang CD, Silvestri AJ. The conversion of methanol and other O-compounds to hydrocarbons over zeolite catalysts. J Catal. 1977;47:249–259.

[8] Chen JQ, Bozzano A, Glover B, Fuglerud T, Kvisle S. Recent advancements in ethylene and propylene production using the UOP/Hydro MTO process. Catalysis Today. 2005;106:103–107.

[9] Koempel H, Liebner W. Lurgi's Methanol To Propylene (MTP) Report on a successful commercialisation. Studies in Surface Science and Catalysis. 2007;167:261–267.

[10] Topp-Jørgensen J. Topsøe integrated gasoline synthesis- The tigas process. Studies in Surface Science and Catalysis. 1988;36:293–305.

[11] Stöcker M. Methanol-to-hydrocarbons: catalytic materials and their behavior. Microporous and Mesoporous Materials. 1999;29:3–48.

[12] Dahl IM, Kolboe S. On the reaction mechanism for propene formation in the MTO reaction over SAPO-34. Catalysis Letters. 1993;20:329–336.

[13] Dahl IM, Kolboe S. On the Reaction Mechanism for Hydrocarbon Formation from Methanol over SAPO-34. I. Isotopic Labeling Studies of the Co-Reaction of Ethene and Methanol. Journal of Catalysis. 1994;149:458–464.

[14] Arstad B, Kolboe S. Methanol-to-hydrocarbons reaction over SAPO-34. Molecules confined in the catalyst cavities at short time on stream. Catalysis Letters. 2001;71:209–212.

[15] Arstad B, Kolboe S. The Reactivity of Molecules Trapped within the SAPO-34 Cavities in the Methanol-to-Hydrocarbons Reaction. J Am Chem Soc. 2001;123:8137–8138.

[16] Sassi A, Wildman MA, Haw JF. Reactions of Butylbenzene Isomers on Zeolite HBeta: Methanol-to-Olefins Hydrocarbon Pool Chemistry and Secondary Reactions of Olefins. J Phys Chem B. 2002;106:8768–8773.

[17] Song W, Nicolas JB, Sassi A, Haw JF. Synthesis of the heptamethylbenzenium cation in zeolite-beta: in situ NMR and theory. Catalysis Letters. 2002;81:49–53.

[18] Bjørgen M, Olsbye U, Petersen D, Kolboe S. The methanol-to-hydrocarbons reaction: insight into the reaction mechanism from [12C]benzene and [13C]methanol coreactions over zeolite H-beta. Journal of Catalysis. 2004;221:1–10.

[19] Svelle S, Joensen F, Nerlov J, Olsbye U, Lillerud KP, Kolboe S, et al. Conversion of Methanol into Hydrocarbons over Zeolite H-ZSM-5: Ethene Formation Is Mechanistically Separated from the Formation of Higher Alkenes. J Am Chem Soc. 2006;128:14770–14771.

[20] Niwa M, Katada N, Sawa M, Murakami Y. Temperature-Programmed Desorption of Ammonia with Readsorption Based on the Derived Theoretical Equation. J Phys Chem. 1995;99:8812–8816.

[21] Zecchina A, Bordiga S, Spoto G, Scarano D, Spanò G, Geobaldo F. IR spectroscopy of neutral and ionic hydrogen-bonded complexes formed upon interaction of CH_3OH, C_2H_5OH, $(CH_3)_2O$, $(C_2H_5)_2O$ and C_4H_8O with H-Y, H-ZSM-5 and H-mordenite: Comparison with analogous adducts formed on the H-Nafion superacidic membrane. J Chem Soc, Faraday Trans. 1996;92:4863–4875.

[22] Paze C, Bordiga S, Lamberti C, Salvalaggio M, Zecchina A, Bellussi G. Acidic Properties of H-Beta Zeolite As Probed by Bases with Proton Affinity in the 118-204 kcal $mol^{-}1$ Range: A FTIR Investigation. J Phys Chem B. 1997;101:4740–4751.

[23] Jin L, Hu H, Zhu S, Ma B. An improved dealumination method for adjusting acidity of HZSM-5. Catalysis Today. 2010;149:207–211.

[24] Haw JF. Zeolite acid strength and reaction mechanisms in catalysisy. Phys Chem Chem Phys. 2002;4:5431–5441.

[25] Baerlocher C, McCusker LB, Olson DH. Atlas of Zeolite Framework Types. 6th ed. Amsterdam: Elsevier; 2007.

[26] Palumbo L, Bonino F, Beato P, Bjørgen M, Zecchina A, Bordiga S. Conversion of Methanol to Hydrocarbons: Spectroscopic Characterization of Carbonaceous Species Formed over H-ZSM-5. J Phys Chem C. 2008;112:9710–9716.

[27] Higgins JB, LaPierre RB, Schlenker JL, Rohrman AC, Wood JD, Kerr GT, et al. The Framework Topology of Zeolite Beta. Zeolites. 1988;8:446–452.

[28] Bjørgen M, Olsbye U, Kolboe S. Coke precursor formation and zeolite deactivation: mechanistic insights from hexamethylbenzene conversion. Journal of Catalysis. 2003;215:30–44.

[29] Bjørgen M, Bonino F, Arstad B, Kolboe S, Lillerud KP, Zecchina A, et al. Persistent Methylbenzenium Ions in Protonated Zeolites: The Required Proton Affinity of the Guest Hydrocarbon. Chem Phys Chem. 2005;6:232–235.

[30] Klein H, Kirschhock C, Fuess H. Adsorption and Diffusion of Aromatic Hydrocarbons in Zeolite Y by Molecular Mechanics Calculation and X-ray Powder Diffraction. J Phys Chem. 1994;98:12345–12360.

[31] Sherry HS. The Ion-Exchange Properties of Zeolites. IV. Alkaline Earth Ion Exchange in the Synthetic Zeolites Linde X and Y. J Phys Chem. 1968;p. 4086–4094.

[32] Kaduk JA, Faber J. Crystal Structure of Zeolite Y as a Function of Ion Exchange. The Rigaku Journal. 1995;12:14–34.

[33] Boréave A, Auroux A, Guimon C. Nature and Strength of Acid Sites in HY Zeolites: a Multitechnical Approach. Microporous Materials. 1997;11:275–291.

[34] Khabtou S, Chevreau T, Lavalley JC. Quantitative infrared study of the distinct acidic hydroxyl groups contained in modified Y zeolites. Microporous Materials. 1994;3:133–148.

[35] Hopkins PD, Miller JT, Meyers BL, Ray GJ, Roginski RT, Kuehne MA, et al. Acidity and cracking activity changes during coke deactivation of ultrastable Y zeolite. Applied Catalysis A: General. 1996;136:29–48.

[36] O'Donovan AW, O'Connor CT, Koch KR. Effect of acid and steam treatment of Na- and H-mordenite on their structural, acidic and catalytic properties. Microporous Materials. 1995;5:185–202.

[37] Sawa M, Niwa M, Murakami Y. Relationship between acid amount and framework aluminum content in mordenite. Zeolites. 1990;10:532–538.

[38] Itho H, Hattor T, Murakami Y. Selective Formation of Alkenes in the Conversion of Methanol into Hydrocarbons on Barium Ion-exchanged Mordenite. JCS Chem Comm. 1981;p. 1091–1092.

[39] Zecchina A, Spoto G, Bordiga S. Vibrational Spectroscopy of Zeolites. John Wiley & Sons Ltd.; 2001.

[40] Bordiga S, Ugliengo P, Damin A, Lamberti C, Spoto G, Zecchina A, et al. Hydroxyls nests in defective silicalites and strained structures derived upon dehydroxylation: vibrational properties and theoretical modelling. Topics in Catalysis. 2001;15:43–52.

[41] Jiao J, Kanellopoulos J, Wang W, Ray SS, Foerster H, Freude D, et al. Characterization of framework and extra-framework aluminum species in non-hydrated zeolites Y by 27Al spin-echo, high-speed MAS, and MQMAS NMR spectroscopy at B0 = 9.4 to 17.6 T. Phys Chem Chem Phys. 2005;7:3221–3226.

[42] Levine IN. Physical Chemistry. 5th ed. New York: McGraw-Hill; 2002.

[43] Günzler H, Gremlich HU. IR Spectroscopy An Introduction. Weinheim: Wiley-WCH; 2002.

[44] Colthup NB, Daly LH, Wiberley SE. Introduction to Infrared and Raman Spectroscopy. 2nd ed. New York: Academic Press,INC.; 1975.

[45] Griffiths PR, de Haseth JA. Fourier Transform Infrared Spectrometry. 2nd ed. John Wiley & Sons, Inc.; 2007.

[46] Bordiga S, Regli L, Lamberti C, Zecchina A, Bjørgen M, Lillerud KP. FTIR Adsorption Studies of H_2O and CH_3OH in the Isostructural H-SSZ-13 and H-SAPO-34: Formation of H-Bonded Adducts and Protonated Clusters. J Phys Chem B. 2005;109:7724–7732.

[47] Holm MS, Svelle S, Joensen F, Beato P, Christensen CH, Bordiga S, et al. Assessing the acid properties of desilicated ZSM-5 by FTIR using CO and 2,4,6-trimethylpyridine (collidine) as molecular probes. Applied Catalysis A: General. 2009;356:23–30.

[48] Lifshin E. X-ray characterization of materials. Wiley-VCH; 1999.

[49] Niemantsverdriet JW. Spectroscopy in Catalysis: An Introduction. 3rd ed. Weinheim: WILEY-VCH; 2007.

[50] Do DD. Adsorption Analysis: Equilibria and Kinetics, vol 2. Imperial College Press; 1998.

[51] Thomas R. Practical guide to ICP-MS: a tutorial for beginners. 2nd ed. Boca Raton: CRC Press; 2008.

[52] Zhou W, Apkarian RP, Wang ZL, Joy D. Fundamentals of Scanning Electron Microscopy I: Scanning Microscopy for Nanotechnology Techniques and Applications. Zhou W, Wang ZL, editors. New York: Springer; 2007.

[53] Braithwaite A, Smith FJ. Chromatographic Methods. 5th ed. Glasgow: Chapman & Hall; 1996.

[54] Gross JH. Mass Spectrometry. Heidelberg: Springer; 2004.

[55] Bi J, Guo X, Liu M, Wang X. High effective dehydration of bio-ethanol into ethylene over nanoscale HZSM-5 zeolite catalysts. Catalysis Today. 2010;149:143–147.

[56] Hassanpour S, Taghizadeh M, Yaripour F. Preparation, Characterization, and Activity Evaluation of H-ZSM-5 Catalysts in Vapor-Phase Methanol Dehydration to Dimethyl Ether. Ind Eng Chem Res. 2010;49:4063–4069.

[57] Sun L, Guo X, Liu M, Wang X. Ethylation of coking benzene over nanoscale HZSM-5 zeolites: Effects of hydrothermal treatment, calcination and La_2O_3 modification. Applied Catalysis A: General. 2009;355:184–191.

[58] Hassanpour S, Yaripour F, Taghizadeh M. Performance of modified H-ZSM-5 zeolite for dehydration of methanol to dimethyl ether. Fuel Processing Technology. 2010;91:1212–1221.

[59] Zheng J, Zeng Q, Yi Y, Wang Y, Ma J, Bo Qin XZ, et al. The hierarchical effects of zeolite composites in catalysis. Catalysis Today. 2011;168:124–132.

[60] Eapen MJ, Reddy KSN, Shiralkar VP. Hydrothermal crystallization of zeolite beta using tetraethylammonium bromide. ZEOLITES. 1994;14:295–302.

[61] Mostowicz R, Testa F, Crea F, AielIo R, Fonseca A, Nagy JB. Synthesis of zeolite beta in presence of fluorides: Influence of alkali cations. Zeolites. 1997;18:308–324.

[62] Hegde SG, Kumar R, Bhat RN, Ratnasamy P. Characterization of the acidity of zeolite Beta by FTi.r. spectroscopy and t.p.d., of NH3. ZEOLITES. 1989;9:231–237.

[63] Wang Y, Li X, Xue Z, Dai L, Xie S, Li Q. Preparation of Zeolite ANA Crystal from Zeolite Y by in Situ Solid Phase Iso-Structure Transformation. J Phys Chem B. 2010;114:5747–5754.

[64] Li X, Prins R, van Bokhoven JA. Synthesis and characterization of mesoporous mordenite. Journal of Catalysis. 2009;262:257–265.

[65] Zhang Y, ChaoJin. Rapid crystallization and morphological adjustment of zeolite ZSM-5 in nonionic emulsions. Journal of Solid State Chemistry. 2011;184:1–6.

[66] Zhu X, Lobban LL, Mallinson RG, Resasco DE. Tailoring the mesopore structure of HZSM-5 to control product distribution in the conversion of propanal. Journal of Catalysis. 2010;271:88–98.

[67] Kunkeler PJ, Moeskops D, van Bekkum H. Zeolite Beta: characterization and passivation of the external surface acidity. Microporous Materials. 1997;11:313–323.

[68] Perez-Pariente J, Martens JA, Jacobs PA. Crystallization Mechanism of Zeolite Beta from $(TEA)_2O$, Na_2O and K_2O Containing Aluminosilicate Gels. Applied Catalysis,. 1987;31:35–64.

[69] Bin Xu FR, Bordiga S, Prins R, van Bokhoven JA. Reversibility of structural collapse in zeolite Y: Alkane cracking and characterization. Journal of Catalysis. 2006;241:66–73.

[70] Koch H, Liepold A, Roos K, Stöcker M, Reschetilowski W. Comparative Study of the Acidic and Catalytic Properties of the Mesoporous Material H-MCM-41 and Zeolite H-Y. Chem Eng Technol. 1999;22:807–811.

[71] Hincapie BO, Garces LJ, Zhang Q, Sacco A, Suib SL. Synthesis of mordenite nanocrystals. Microporous and Mesoporous Materials. 2004;67:19–26.

[72] Zecchina A, Bordiga S, Spoto G, Marchese L, Petrini G, Leofanti G, et al. Silicaiite Characterization. 1. Structure, Adsorptive Capacity, and I R Spectroscopy of the Framework and Hydroxyl Modes. J Phys Chem. 1992;96:4985–4990.

[73] Zecchina A, Geobaldo F, Spoto G, Bordiga S, Ricchiardi G, Buzzoni R, et al. FTIR Investigation of the Formation of Neutral and Ionic Hydrogen-Bonded Complexes by Interaction of H-ZSM-5 and H-Mordenite with CH_3CN and H_2O: Comparison with the H-NAFION Superacidic System. J Phys Chem. 1996;100:16584–16599.

[74] Buzzoni R, Bordiga S, Ricchiardi G, Spoto G, Zecchina A. Interaction of H_2O, CH_3OH, $(CH_3)_2O$, CH_3CN, and Pyridine with the Superacid Perfluorosulfonic Membrane Nafion: An IR and Raman Study. J Phys Chem. 1995;99:11937–11951.

[75] Jungsuttiwong S, Limtrakul J, Truong TN. Theoretical Study of Modes of Adsorption of Water Dimer on H-ZSM-5 and H-Faujasite Zeolites. J Phys Chem B. 2005;109:13342–13351.

[76] Forester TR, Howe RF. In Situ FTIR Studies of Methanol and Dimethyl Ether in ZSM-5. J Am Chem Soc. 1987;109:5076–5082.

[77] Campbell SM, Jiang XZ, Howe RF. Methanol to Hydrocarbons: Spectroscopic Studies and the Significance of Extra-Framework Aluminium. Microporous and Mesoporous Materials. 1999;29:91–108.

[78] Rozwadowski M, Lezanska M, Wloch J, Erdmann K, Golembiewski R, Kornatowski J. Investigation of Coke Deposits on Al-MCM-41. Chem Mater. 2001;13:1609–1616.

[79] Bjørgen M, Lillerud KP, Olsbye U, Bordiga S, Zecchina A. 1-Butene Oligomerization in Brønsted Acidic Zeolites: Mechanistic Insights from Low-Temperature in Situ FTIR Spectroscopy. J Phys Chem B. 2004;108:7862–7870.

[80] Hunger M. IR study on methanol-to-olefin reaction over zeolites with different pore structures and acidities. Microporous and Mesoporous Materials. 2005;82:241–255.

[81] Li C, Stair PC. Ultraviolet Raman spectroscopy characterization of coke formation in zeolites. Catalysis Today. 1997;33:353–360.

[82] Seo G, Jeong HS, Hong SB, Uh YS. Skeletal isomerization of 1-butene over ferrierite and ZSM-5 zeolites: influence of zeolite acidity. Catalysis Letters. 1996;36:249–253.

[83] Petkovic LM, Ginosar DM, Burch KC. Supercritical fluid removal of hydrocarbons adsorbed on wide-pore zeolite catalysts. Journal of Catalysis. 2005;234:328–339.

[84] Tripathi AK, Sahasrabudhe A, Mitra S, Mukhopadhyay R, Gupta NM, Kartha VB. QENS and FTIR studies on binding states of benzene molecules adsorbed in zeolite HZSM-5 at room temperature. Phys Chem Chem Phys. 2001;3:4449–4455.

[85] Park JW, Seo G. IR study on methanol-to-olefin reaction over zeolites with different pore structures and acidities. Applied Catalysis A: General. 2009;365:180–188.

[86] Haber J, Komorek-Hlodzik J, Romotowski T. I.r. study of the transformations of olefins, alcohols and ethers on zeolites. Zeolites. 1982;2:179–184.

[87] Campbell SM, Bibby DM, Coddington JM, Howe RF. Dealumination of HZSM-5 Zeolites. JOURNAL OF CATALYSIS. 1996;161:350–358.

[88] Maijanen A, Derouane EG, Nagy JB. FT-IR and solid-state NMR investigation of surface hydroxyl groups on dealuminated ZSM-5. Applied Surface Science. 1994;75:204–212.

[89] Cheung P, Bhan A, Sunley GJ, Law DJ, Iglesia E. Site requirements and elementary steps in dimethyl ether carbonylation catalyzed by acidic zeolites. Journal of Catalysis. 2007;425:110–123.

[90] Lin X, Fan Y, Shi G, Liu H, Bao X. Coking and Deactivation Behavior of HZSM-5 Zeolite-Based FCC Gasoline Hydro-Upgrading Catalyst. Energy & Fuels. 2007;21:2517–2524.

[91] Bjørgen M, Bonino F, Kolboe S, Lillerud KP, Zecchina A, Bordiga S. Spectroscopic Evidence for a Persistent Benzenium Cation in Zeolite H-Beta. J Am Chem Soc. 2003;125:15863–15868.

[92] Zecchina A, Bordiga S, Spoto G, Marcbese L, Petrid G, Leofanti G, et al. Sllicallte Characterization. 2. IR Spectroscopy of the Interaction of CO with Internal and External Hydroxyl Groups. J Phys Chem. 1992;96:4991–4997.

[93] Bordiga S, Roggero I, Ugliengo P, Zecchina A, Bolis V, Artioli G, et al. Characterisation of defective silicalites. J Chem Soc, Dalton Trans. 2000;p. 3921–3929.

Appendix A

Additional FTIR spectra

A.1 H-ZSM-5 15 during MTH at 250 °C

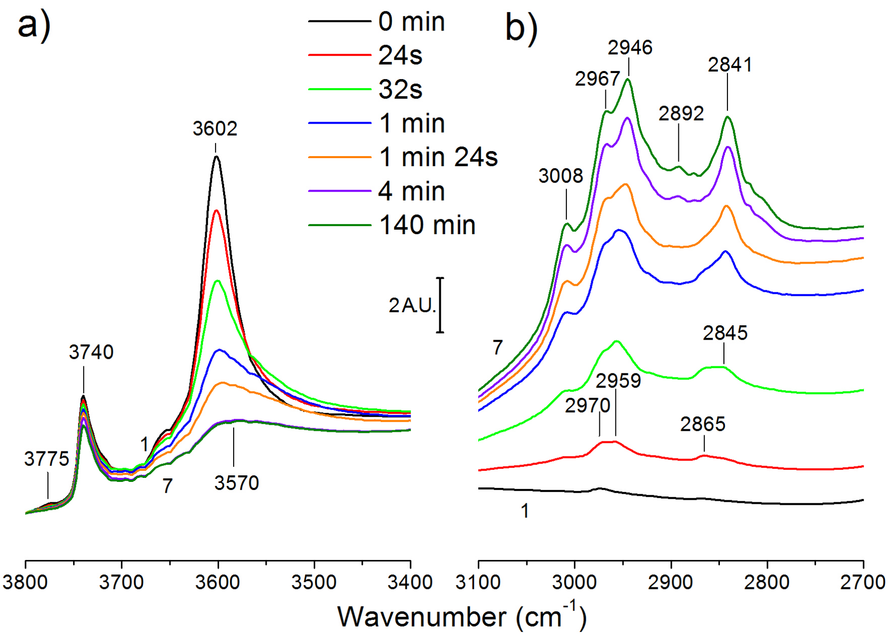

Figure A.1: Selected DRIFTS spectra of H-ZSM-5 15 during MTH-reaction at 250°C. Spectrum 1 before reaction. (a) v(O-H) region; (b) v(C-H) region

A.2 H-ZSM-5 15 during flushing at 350 °C

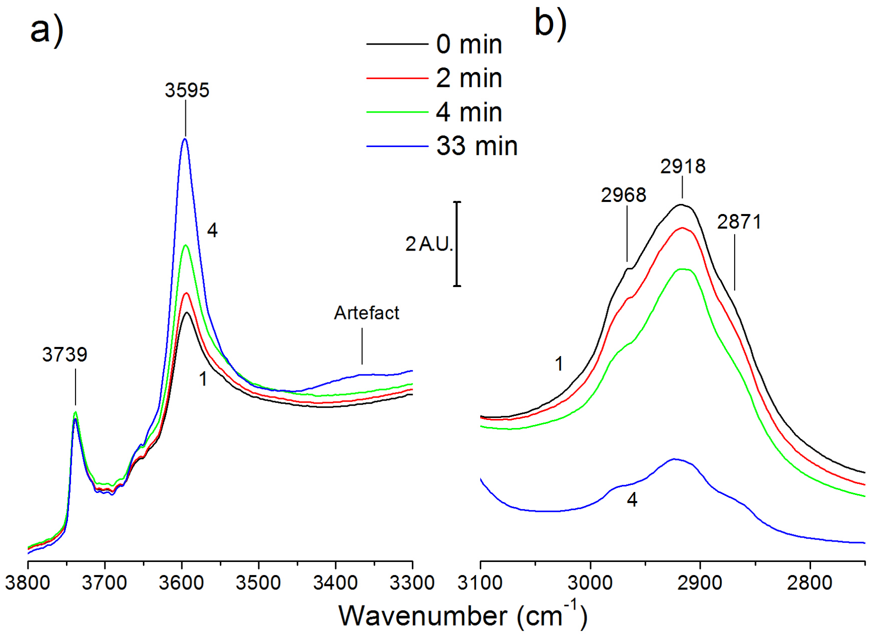

Figure A.2: Selected DRIFTS spectra of H-ZSM-5 15 during flushing following MTH-reaction at 350°C. Spectrum 1 before flushing. (a) v(O-H) region; (b) v(C-H) region. Spectrum 4 contains artefacts.